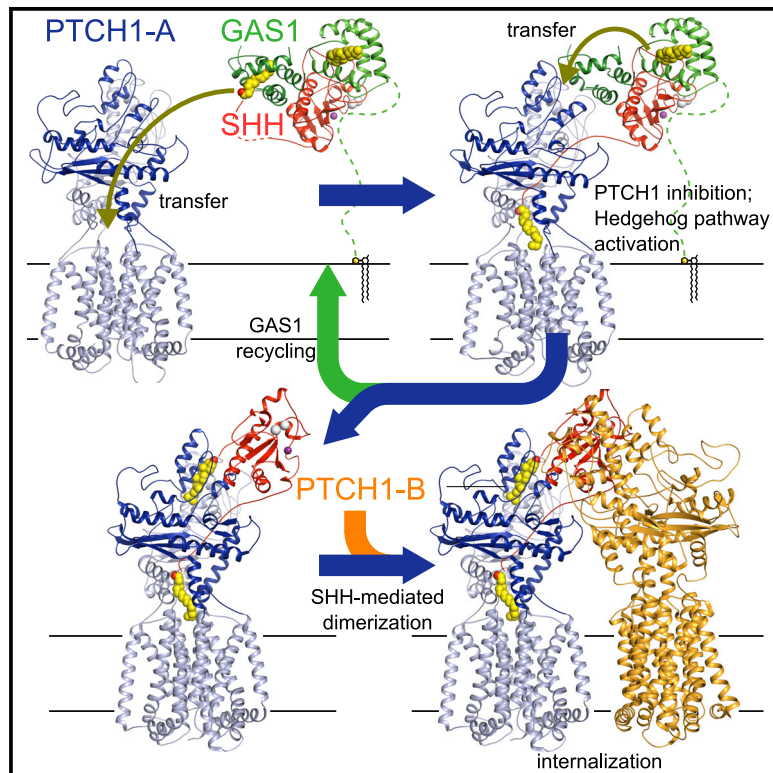# Developmental Cell

Structural basis for catalyzed assembly of the Sonic hedgehog–Patched1 signaling complex

Graphical abstract

Authors

Pengxiang Huang,
Bradley M. Wierbowski, Tengfei Lian,
Charlene Chan, Sara García-Linares,
Jiansen Jiang, Adrian Salic

Correspondence

jiansen.jiang@nih.gov (J.J.),
asalic@hms.harvard.edu (A.S.)

In brief

Huang et al. elucidate how the GAS1 coreceptor catalyzes Hedgehog pathway activation by SHH via sequential handoffs. GAS1 accepts dually lipidated SHH from extracellular SCUBE2, then a transient GAS1–PTCH1 interaction promotes SHH transfer to PTCH1, causing its inhibition. Subsequent SHH-mediated PTCH1 dimerization drives SHH–PTCH1 internalization from the cell surface.

Highlights

- GAS1 is a modular lipid-binding protein recognizing both SHH palmitate and cholesterol

- Lipid-independent GAS1–SHH contact facilitates transfer of lipidated SHH from SCUBE2

- GAS1–PTCH1 contact is critical for direct delivery of SHH to PTCH1

- SHH–PTCH1 engages a second PTCH1 molecule, triggering endocytosis

CellPress

Developmental Cell

CellPress

Article

Structural basis for catalyzed assembly of the Sonic hedgehog–Patched1 signaling complex

Pengxiang Huang,[1,3,4] Bradley M. Wierbowski,[1,3] Tengfei Lian,[2,3] Charlene Chan,[1] Sara García-Linares,[1,5] Jiansen Jiang,[2,*] and Adrian Salic[1,6,*]
[1]Department of Cell Biology, Harvard Medical School, Boston, MA 02115, USA
[2]Laboratory of Membrane Proteins and Structural Biology, Biochemistry and Biophysics Center, National Heart Lung and Blood Institute, National Institutes of Health, Bethesda, MD 20892, USA
[3]These authors contributed equally
[4]Present address: Department of Molecular and Cellular Biology, Baylor College of Medicine, Houston, TX 77030, USA
[5]Present address: Departamento de Bioquímica y Biología Molecular, Universidad Complutense, 28040 Madrid, Spain
[6]Lead contact
*Correspondence: jiansen.jiang@nih.gov (J.J.), asalic@hms.harvard.edu (A.S.)
https://doi.org/10.1016/j.devcel.2022.02.008

SUMMARY

The dually lipidated Sonic hedgehog (SHH) morphogen signals through the tumor suppressor membrane protein Patched1 (PTCH1) to activate the Hedgehog pathway, which is fundamental in development and cancer. SHH engagement with PTCH1 requires the GAS1 coreceptor, but the mechanism is unknown. We demonstrate a unique role for GAS1, catalyzing SHH–PTCH1 complex assembly in vertebrate cells by direct SHH transfer from the extracellular SCUBE2 carrier to PTCH1. Structure of the GAS1–SHH–PTCH1 transition state identifies how GAS1 recognizes the SHH palmitate and cholesterol modifications in modular fashion and how it facilitates lipid-dependent SHH handoff to PTCH1. Structure-guided experiments elucidate SHH movement from SCUBE2 to PTCH1, explain disease mutations, and demonstrate that SHH-induced PTCH1 dimerization causes its internalization from the cell surface. These results define how the signaling-competent SHH–PTCH1 complex assembles, the key step triggering the Hedgehog pathway, and provide a paradigm for understanding morphogen reception and its regulation.

INTRODUCTION

Hedgehog (Hh) signaling is one of a handful of essential pathways that orchestrate animal embryogenesis (Ingham and McMahon, 2001; Lum and Beachy, 2004). Deficient Hh signaling leads to birth defects, such as holoprosencephaly (HPE), the most frequent congenital brain malformation (Roessler et al., 2009), whereas uncontrolled Hh activation causes various cancers (Rubin and de Sauvage, 2006). Transduction of Hh signals across the plasma membrane is governed by the membrane protein Patched1 (PTCH1) (Chen and Struhl, 1996; Marigo et al., 1996; Stone et al., 1996), a member of the Resistance–Nodulation–Division (RND) family of small molecule pumps (Nikaido, 2018). When the Hh pathway is off, PTCH1 inhibits the GPCR-like transducer Smoothened (SMO) (Alcedo et al., 1996; van den Heuvel and Ingham, 1996) by antagonizing its activation by cholesterol (Huang et al., 2016; Luchetti et al., 2016; Petrov et al., 2021). The Hh pathway is triggered by a Hh ligand, best exemplified by vertebrate Sonic hedgehog (SHH) (Echelard et al., 1993; Krauss et al., 1993; Riddle et al., 1993; Chang et al., 1994), which binds PTCH1, causing its inhibition and internalization. With PTCH1 thus neutralized, cholesterol activates SMO, leading to activation of GLI transcription factors (Humke et al., 2010; Tukachinsky et al., 2010), which drive the gene expression program of the Hh pathway.

Hh ligands are uniquely modified with palmitate on the N terminus (Pepinsky et al., 1998) and cholesterol on the C terminus (Porter et al., 1996b; Beachy et al., 1997). In the case of SHH, its lipid moieties ultimately bind PTCH1 (Qi et al., 2018a, 2018b; Qian et al., 2018; Rudolf et al., 2019), with the palmitate being critical for inhibiting PTCH1 and for signaling (Williams et al., 1999; Tukachinsky et al., 2016). Although lipid-dependent SHH–PTCH1 complexes can be assembled in vitro in detergent, lipidated SHH is highly insoluble and thus strongly attached to membranes in vivo, requiring dedicated factors for dissemination from producing cells and for engaging PTCH1. A carrier, such as SCUBE2 (Kawakami et al., 2005; Woods and Talbot, 2005; Hollway et al., 2006), is needed for extracellular SHH release (Creanga et al., 2012; Tukachinsky et al., 2012). SCUBE2 solubilizes SHH by binding its lipids, forming a highly active complex that delivers SHH to faraway cells (Wierbowski et al., 2020). Interestingly, the lipid-dependent interactions of SHH with SCUBE2 and PTCH1 are mutually exclusive, prompting the question of how SHH moves from the former to the latter. We proposed that SHH is shuttled via a sequential pathway (Wierbowski et al., 2020) mediated by SHH coreceptors, a group of
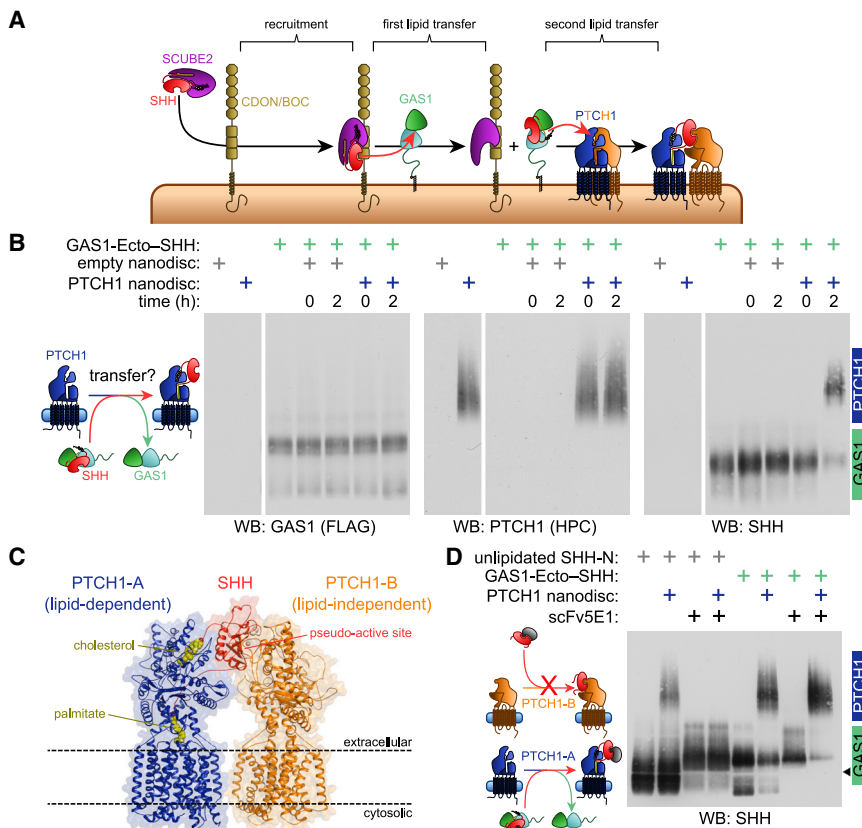
Figure 1. SHH–PTCH1 complex assembly by direct transfer of SHH from GAS1 to PTCH1

(A) Coreceptor pathway for SHH reception. SCUBE2–SHH is recruited by CDON/BOC, and SHH is transferred to GAS1 and then to PTCH1.

(B) Purified GAS1 ectodomain bound to SHH (GAS1-Ecto–SHH, 200 nM) was incubated with PTCH1 nanodiscs (600 nM), and the mixture was analyzed by native PAGE and immunoblotting. SHH is transferred to PTCH1, but not to empty nanodiscs.

(C) Lipid-dependent and -independent SHH–PTCH1 interaction modes (PDB ID: 6RVD). One PTCH1 molecule (PTCH1-A, blue) interacts with SHH (red) through its N- and C-terminal lipids (yellow). A second molecule (PTCH1-B, orange) interacts with the pseudo-active site of the SHH globular domain.

(D) As in (B), but including unlipidated SHH (SHH-N). SHH species (500 nM) were preincubated with the HaloTag-fused anti-SHH antibody scFv5E1 (Wierbowski et al., 2020) (2.5 μM), which binds the SHH pseudo-active site, or HaloTag (negative control). scFv5E1 blocks SHH-N binding to PTCH1 but not SHH transfer from GAS1 to PTCH1. Arrowhead indicates size of scFv5E1.

Here, we use *in vitro* reconstitution with purified proteins to demonstrate that GAS1 directly transfers SHH to PTCH1. We next solve the cryo-EM structure of a GAS1–SHH–PTCH1 complex, which captures the transition state in SHH handoff. The structure elucidates the unique mode of SHH recognition by GAS1, involving modular binding of lipid moieties and extensive contacts around the SHH globular domain, which explain SHH mutations that cause HPE. We identify a GAS1–PTCH1 contact, which is critical for SHH transfer to PTCH1 and for Hh signaling. Structure-guided mutagenesis and functional assays show how SHH moves from CDON/BOC–SCUBE2 to GAS1 and then to PTCH1. Finally, our data indicate that SHH first engages PTCH1 via lipid-dependent binding, then recruits a second PTCH1 molecule via lipid-independent binding. This SHH-mediated bridging of PTCH1 serves to internalize SHH–PTCH1 but is dispensable for signaling. These results define the essential GAS1-catalyzed pathway for assembly of the signaling-competent SHH–PTCH1 complex.

RESULTS

GAS1 directly transfers dually lipidated SHH to PTCH1

GAS1 is essential for Hh pathway activation by SCUBE2–SHH (Figure 1A; Wierbowski et al., 2020). To test whether GAS1 suffices to transfer SHH to PTCH1, we purified *Xenopus laevis* PTCH1 and reconstituted it in lipid nanodiscs (Figures S1A and S1B) or amphipol (Figures S1C and S1D). PTCH1 nanodiscs were incubated with purified GAS1–SHH, and the mixture was analyzed by native gel electrophoresis. SHH moved from GAS1 to a species of lower electrophoretic mobility, which

three proteins essential for Hh signaling (Allen et al., 2011), comprising the related transmembrane proteins CDON and BOC (Okada et al., 2006; Tenzen et al., 2006; Yao et al., 2006; Zhang et al., 2006) and the GPI-anchored GAS1 (Lee et al., 2001; Allen et al., 2007; Martinelli and Fan, 2007). In this model, CDON/BOC recruit SCUBE2–SHH to the cell surface, forming a ternary complex, then SHH undergoes two successive transfers, from CDON/BOC–SCUBE2 to GAS1 and from GAS1 to PTCH1.

GAS1 plays the central role in SHH reception, being necessary and sufficient for signaling by SCUBE2–SHH (Wierbowski et al., 2020); however, key questions remain unanswered. SHH movement from GAS1 to PTCH1 was demonstrated only in cells (Wierbowski et al., 2020); therefore, it is unknown if GAS1 is sufficient for SHH–PTCH1 assembly or whether additional factors are required. Furthermore, it is unknown how GAS1 recognizes SHH. It appears that GAS1 has a unique interaction with SHH, binding not only SHH lipids (Wierbowski et al., 2020) but also the globular domain (Martinelli and Fan, 2009), distinct from other SHH-binding proteins, including CDON/BOC (McLellan et al., 2008; Kavran et al., 2010), PTCH1 (Gong et al., 2018; Qi et al., 2018a, 2018b; Qian et al., 2018; Rudolf et al., 2019), and the Hh inhibitory protein, HHIP (Bishop et al., 2009; Bosanac et al., 2009); however, the structure of GAS1 bound to SHH has not been solved. Finally, a major finding in recent cryo-EM structures is that SHH can simultaneously engage two PTCH1 molecules via distinct binding modes (Qi et al., 2018a; Qian et al., 2018), but it is unclear how such ligand-induced PTCH1 dimers participate in SHH reception and signaling.

Developmental Cell
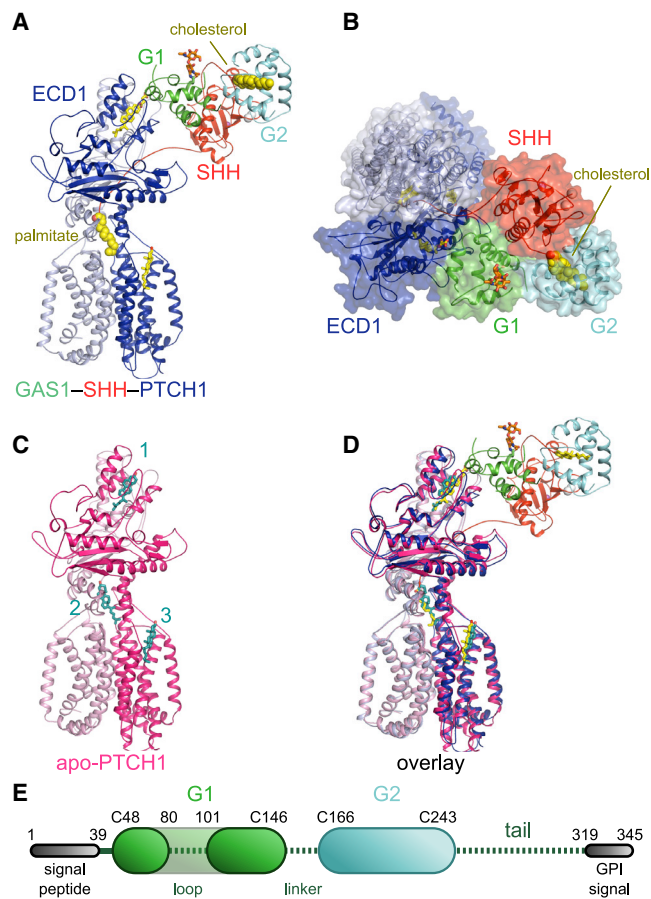## Article

CellPress

Figure 2. Structure of the GAS1–SHH–PTCH1 transfer intermediate

(A) Structure of GAS1–SHH–PTCH1 in nanodisc. First half of PTCH1 (blue), second half of PTCH1 (light blue), SHH (red), SHH lipids (yellow, space-filling), GAS1-G1 domain (green), GAS1-G2 domain (cyan), GAS1-G1 glycan (orange), cholesteryl hemisuccinate (CHS) (yellow, sticks) bound to site 1 (in PTCH1-ECD1), and cholesterol (yellow, sticks) bound to site 3 [in sterol-sensing domain (SSD) of PTCH1]. GAS1-G1 binds to PTCH1-ECD1. See Figures S2E–S2N for corresponding electron density images.

(B) As in (A), but rotated 110°, looking down toward the membrane. Molecular surface is displayed. GAS1-G1 contacts PTCH1, GAS1-G2, and SHH.

(C) Structure of apo-PTCH1 in nanodisc. First half of PTCH1 (deep pink), second half of PTCH1 (light pink), cholesterol molecules (light blue, sticks) bound to site 1, site 2 (juxta-membrane portion of PTCH1), and site 3. See Figures S2A–S2D for electron density images.

(D) GAS1–SHH–PTCH1 overlaid on apo-PTCH1. GAS1–SHH binding does not cause major changes in PTCH1 conformation. Cholesterol bound to site 2 is displaced by the N-terminal SHH palmitate. C-terminal SHH cholesterol is bound to a cavity in GAS1-G2. See Figures S5E and S5F for additional structural alignments.

(E) GAS1 schematic, showing boundaries of G1 and G2. Dotted line indicates unstructured regions.

co-migrated with PTCH1 nanodiscs, indicating SHH transfer (Figure 1B). Importantly, SHH transfer increased with PTCH1 concentration (Figure S1E), whereas SHH remained bound to GAS1 when incubated with empty nanodiscs (Figures 1B and S1E). More than 50% of SHH transferred from GAS1 to an equimolar amount of PTCH1, suggesting that forward transfer is energetically favored (Figure S1E). We also observed a small amount of GAS1 recruited with SHH to PTCH1 (Figure S1F), sug-

gestive of a transfer intermediate. Similar results were obtained using PTCH1 in amphipol, indicating that the membrane bilayer was not required for transfer (Figure S1G). Finally, transfer occurred rapidly, reaching 50% completion after 10 min (Figure S1G). Thus, the SHH–PTCH1 complex forms by direct transfer of SHH from GAS1.

SHH binds PTCH1 via two modes (Figure 1C): one between SHH lipids and two hydrophobic PTCH1 cavities (PTCH1-A, lipid-dependent) (Williams et al., 1999; Tukachinsky et al., 2016; Qi et al., 2018b) and another between the SHH pseudo-active site and the two extracellular domains (ECDs) of PTCH1 (PTCH1-B, lipid-independent) (Fuse et al., 1999; Pepinsky et al., 2000; Tukachinsky et al., 2016; Gong et al., 2018). We asked whether the PTCH1-B binding mode is necessary for SHH transfer from GAS1 to PTCH1, by assaying transfer in the presence of the anti-SHH antibody 5E1 (Ericson et al., 1996), which blocks the pseudo-active site (Maun et al., 2010). As shown in Figure 1D, 5E1 bound GAS1–SHH but did not affect SHH transfer to PTCH1. In contrast, 5E1 completely blocked binding of unlipidated SHH (Figures S1H and S1I) to PTCH1 (Figure 1D), an interaction that involves solely the PTCH1-B mode (Wierbowski et al., 2020). Thus, the PTCH1-A binding mode, but not PTCH1-B, drives SHH transfer from GAS1 to PTCH1.

Structure of the transition intermediate in SHH–PTCH1 complex assembly

To dissect the GAS1-mediated pathway for SHH–PTCH1 formation, we isolated a GAS1–SHH–PTCH1 complex. Briefly, we obtained stoichiometric GAS1–SHH by tandem affinity purification (Figures S1J and S1K) using internally tagged SHH (Wierbowski et al., 2020); importantly, this complex had similar potency to GAS1–SHH containing untagged SHH (Figure S1L). When PTCH1 nanodiscs were incubated with excess GAS1–SHH followed by size-exclusion chromatography, PTCH1, SHH, and GAS1 co-purified, suggesting complex formation (Figures S1M and S1N). We used cryo-electron microscopy (cryo-EM) to solve the structure of this ternary complex at 3.5 Å resolution (Figures 2A, 2B, S2, and S3). For structural comparison, we also determined the cryo-EM structure of unliganded *Xenopus laevis* PTCH1 (apo-PTCH1) in nanodisc at 3.0 Å (Figures 2C, S2, and S4).

Figure 2A shows the arrangement of SHH, PTCH1, and GAS1 within the complex. For model building, the SHH globular domain from a high-resolution crystal structure (Hall et al., 1995) and our apo-PTCH1 structure could be immediately docked into the cryo-EM map, as these two components are nearly identical to their isolated forms. The overall architecture of PTCH1 in nanodisc is very similar to that of PTCH1 in detergent, without major conformational changes (Gong et al., 2018; Qi et al., 2018a, 2018b, 2019; Qian et al., 2018; Zhang et al., 2018; Rudolf et al., 2019). The transmembrane domain (TMD) is almost identical in all structures, regardless of the presence of SHH, whereas ECD1 and ECD2 undergo only limited rigid body motion, both together and relative to each other (Figures 2D and S5A–S5F). As in other structures (Gong et al., 2018; Zhang et al., 2018; Qi et al., 2019), sterol-like densities are seen at three distinct locations in apo-PTCH1 (Figures S2A–S2D), which we interpret as bound cholesterol molecules (Figure 2C).

GAS1 consists of two cysteine-rich domains (G1 and G2) homologous to those in glial cell line–derived neurotrophic factor (GDNF) family receptors (GFRα) (Cabrera et al., 2006), connected through a linker, and a C-terminal unstructured tail (Figure 2E). The well-resolved side-chain densities for G1 allowed us to trace the amino acid sequence, yielding an α-helical fold resembling the homologous domains in GFRα (Wang et al., 2006; Parkash et al., 2008; Parkash and Goldman, 2009; Hsu et al., 2017; Sandmark et al., 2018; Li et al., 2019). While this manuscript was in revision, the AlphaFold Protein Structure Database (Jumper et al., 2021; Tunyasuvunakool et al., 2021) released the predicted GAS1 structure, containing a G1 domain nearly identical to that in our initial model. We then used the AlphaFold-predicted structure to build the model for GAS1-G2. The final GAS1 model contains two well-folded globular domains, leaving unresolved a low-complexity loop in G1, the interdomain linker, and the unstructured C-terminal tail (Figures 2A, 2B, and 2E). Importantly, a GAS1 construct lacking the loop, linker, and most of the tail (Figures S5G and S5H) readily accepted SHH from SCUBE2 (Figure S5I), indicating that the unresolved parts are not necessary for SHH engagement.

GAS1-G1 is a hub for protein–protein interactions in GAS1–SHH–PTCH1. G1 binds PTCH1-ECD1, partially covering the opening of its sterol-binding pocket (SBP), which is occupied by a copurifying molecule of cholesteryl hemisuccinate (CHS) (Figure 2A). G1 also forms contacts with G2, together grasping the SHH globular domain, which does not contact PTCH1 (Figure S5J). The palmitoylated N-terminal SHH peptide, no longer bound to GAS1, is inserted between PTCH1-ECD1 and -ECD2, displacing a cholesterol molecule. This palmitate position is the same as in the final SHH–PTCH1 complex (Qi et al., 2018a, 2018b; Qian et al., 2018; Rudolf et al., 2019). Strikingly, the C-terminal SHH cholesterol is bound inside a central cavity of GAS1-G2. Thus, the GAS1–SHH–PTCH1 structure captures a transition state in SHH transfer, with SHH palmitate already engaged with PTCH1, but SHH cholesterol still GAS1-bound. We speculate that CHS in the SBP stabilizes the transition state by blocking transfer of SHH cholesterol. Perhaps, complete SHH transfer to PTCH1 (Figure 1) results from excess GAS1 extracting CHS, freeing up the SBP to accept SHH cholesterol.

GAS1 is a modular palmitate- and cholesterol-binding protein

GAS1 is distantly related to GFRα1–4, which bind GDNF, neurturin (NRTN), artemin (ARTN), and persephin (PSPN) (Cabrera et al., 2006), and to the GFRα-like GFRAL, which binds GDF15 (Figure S6; Hsu et al., 2017). GFRα proteins and GFRAL typically contain three copies of the cysteine-rich domain (D1–D3). GAS1-G1 and -G2 adopt a similar fold, consisting of five α-helices (H1–H5) arranged in a triangular spiral, stabilized by five disulfide bonds (Figures 3A–3C). The conserved disulfide pattern within a small domain imposes overall fold conservation in spite of low sequence similarity (Figure S6A; Cabrera et al., 2006). GAS1-G1 and -G2 are most similar to GFRα-D2 (Figures S6B–S6D), which mediates all interactions with ligands (Figures S6E–S6I). In GFRα2–NRTN (Sandmark et al., 2018; Li et al., 2019), a concave surface in the center of a triangle formed by helices H1, H2, and H5 of GFRα2-D2 interacts with two protruding NRTN fingers (Figure 3D). In GAS1-G2, helices H1–H4 are well

aligned with GFRα2-D2, but the outward movement of H5 causes the concave binding area to collapse, forming a large cavity ($\sim$712 Å^3 volume) lined by mostly hydrophobic and nonpolar residues, which accommodates SHH cholesterol (Figure 3E). Similarly, because of H5 displacement, GAS1-G1 also contains a central cavity, with its opening facing PTCH1, but its volume is smaller ($\sim$390 Å^3), consistent with binding smaller hydrophobics, such as palmitate (Figure 3F).

The above suggest GAS1 is a modular lipid-binding protein, with G1 binding palmitate and G2 binding cholesterol (Figure 3G). To test this hypothesis, we purified G1 (Figures S7A and S7B) and G2 (Figures S7C and S7D) and assayed their ability to accept radiolabeled cholesterol (Figure 3H) or palmitate (Figure 3I) from full-length GAS1 ectodomain (Figures S7E and S7F; Wierbowski et al., 2020). G2, but not G1, bound cholesterol (Figure 3H), consistent with G2 binding the SHH cholesteryl moiety. In contrast, both G1 and G2 bound half as much palmitate as GAS1 (Figure 3I), suggesting each domain can accommodate palmitate. Importantly, GFRα1 (Figure S7G) did not bind cholesterol or palmitate (Figures 3H and 3I), confirming that lipid binding by GAS1 is unique among GFRα-related proteins.

We also assayed the interaction between palmitoylated SHH effector peptide (EP, SHH residues 24–45) (Tukachinsky et al., 2016) and GAS1 constructs, using cell-binding assays. GAS1 lacking G1 bound about half as much palmitoylated EP as full-length GAS1 (Figure S7H). Finally, we investigated SHH EP–GAS1 interaction by isothermal titration calorimetry. Palmitoylated EP bound GAS1 with low-micromolar affinity (K_d = 3.84 µM, Figure S7I). Shortening the fatty acid to 8 carbons reduced affinity $\sim$10-fold (K_d = 34.6 µM, Figure S7J), whereas removal of the lipid moiety abolished the interaction (Figure S7K). GAS1 bound a truncated palmitoylated SHH EP (residues 24–32) with similar affinity (K_d = 3.72 µM; Figure S7L), in contrast to PTCH1 (Tukachinsky et al., 2016), which prefers the longer peptide. In summary, our results suggest that GAS1-G1 and -G2 bind the palmitoylated and cholesterylated SHH termini, respectively. Future structural studies will be required to determine precisely how palmitate is bound in the pre-transfer GAS1–SHH complex.

Both palmitate and cholesterol binding are necessary for GAS1 function

We next tested the role of palmitate and cholesterol binding by GAS1 in SHH transfer from SCUBE2–SHH (Figure 1A). Neither G1 nor G2 (Figures S7A–S7D, S7M, and S7N) accepted SHH (Figure 3J), in contrast to GAS1 (Figures S7E and S7F). Surprisingly, a GAS1 mutant missing the entire unstructured tail (G1-G2) (Figures S7O and S7P) was also defective, suggesting additional requirements for SHH transfer besides lipid binding. To further investigate GAS1-G1 and -G2 lipid specificity, we assayed transfer of singly lipidated SHH from SCUBE2 (Figure 3K). Cholesterylated-only SHH was transferred to GAS1 and GAS1 missing G1 (G2-Tail), whereas palmitoylated-only SHH was transferred to GAS1, to G2-Tail, and, less robustly, to G1, consistent with the GAS1 tail requirement. Thus, G2 is a dedicated cholesterol-binding module, whereas G1 and G2 can bind palmitate. Since GAS1 binds both SHH lipids at once, these results indicate that G1 is the palmitate-binding site.

We probed the role of GAS1 cholesterol binding by structure-guided mutagenesis. Mutating a residue at the solvent interface
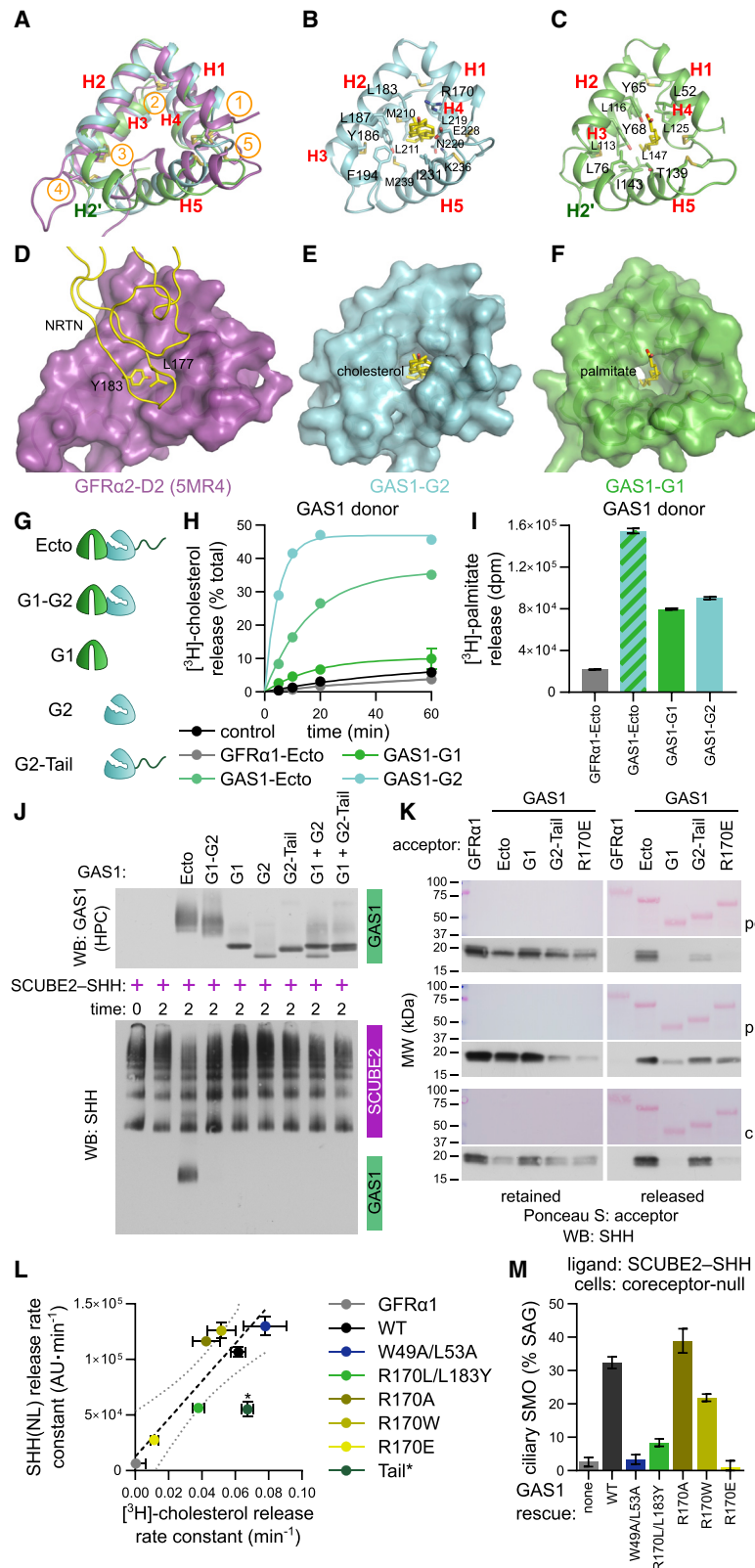
Figure 3. GAS1 is a dual lipid-binding protein essential for SHH reception

(A) Comparison of GAS1-G1 (green), GAS1-G2 (cyan), and GFRα2-D2 (magenta) (PDB ID: 5MR4). The domain fold consists of five helices (H1–H5) stabilized by five conserved disulfides (circled yellow numbers). Overall fold is highly conserved, with H1–H4 aligning well between GAS1-G1, GAS1-G2, and GFRα2-D2.

(B) As in (A), but showing only GAS1-G2. H5 movement creates a central cavity in GAS1-G2, in which SHH cholesterol (yellow sticks) inserts.

(C) As in (A), but showing only GAS1-G1. GAS1-G1 contains an additional short helix (H2′). Like G2, G1 contains a central hydrophobic cavity, but smaller, inside which a palmitate residue (yellow sticks) is modeled.

(D) Binding of neurturin (NRTN, yellow) to GFRα2-D2 (molecular surface, magenta) (PDB ID: 5MR4). Side chains of L177 and Y183 at the fingertip of NRTN bind a shallow pocket at the center of GFRα2-D2.

(E) As in (B), but showing molecular surface of GAS1-G2.

(F) As in (C), but showing molecular surface of GAS1-G1.

(G) Schematic of purified GAS1-Ecto variants used in (H)–(K).

(H) GAS1-Ecto loaded with [³H]-cholesterol was captured on beads, which were incubated with GAS1-Ecto (positive control), GAS1-G1, GAS1-G2, GFRα1-Ecto, or tag-only negative control (2 μM). Radioactivity released was measured as a function of time across four time points. Points represent average of three replicates, and error bars represent SEM. Data are fit with a one-phase association curve.

(I) As in (H), but with GAS1-Ecto loaded with [³H]-palmitate. Bars represent average release across the four time points, with error bars representing SEM. GAS1-Ecto and GFRα1-Ecto rates are the same as in Figure S6M of Wierbowski et al., 2020, as part of an experiment that included GAS1-G1 and -G2 (shown here).

(J) SCUBE2–SHH (400 nM) was incubated with indicated GAS1 variants (4 μM), and the reactions were analyzed by native PAGE and immunoblotting. GAS1-G1, GAS1-G2 and a region of the unstructured GAS1 tail are required to accept SHH from SCUBE2. The ladder-like pattern of SHH is due to SCUBE2 oligomerization (Wierbowski et al., 2020).

(K) GAS1-Ecto–SHH in which SHH is either dually lipidated (pc), palmitoylated-only (p), or cholesterylated-only (c), was immobilized on beads. Beads were incubated with GAS1 variants or GFRα1-Ecto (negative control) and released and retained material was analyzed by Ponceau staining and SHH immunoblotting. SHHpc is released only by GAS1-Ecto. SHHc is released by GAS1-Ecto and GAS1-G2-Tail, but not by GAS1(R170E)-Ecto (defective in cholesterol binding, see (L)). SHHp is released by all GAS1 constructs.

(L) Correlation between rates of cholesterol release (measured as in (H)) and of NanoLuc-tagged SHH [SHH(NL)] release from SCUBE2–SHH(NL) (Wierbowski et al., 2020) by purified GAS1 mutants. Rate constants for cholesterol were fit with a one-phase association curve, and for SHH with a linear regression. Error bars represent standard error of the fits. See Figures S7R and S7S for time courses. Dashed line represents linear regression ($R^2 = 0.839$) fit to all species except GAS1-Tail* (asterisk), and dotted line represents the 95% confidence interval of the linear fit. Release rate constants for cholesterol and SHH show good correlation. GAS1-Tail*, with mutations in the tail, exhibits robust cholesterol release but impaired SHH release (see Figure 5).

(M) Coreceptor-null MEFs (Mathew et al., 2014) stably expressing GAS1 constructs were treated with purified SCUBE2–SHH (0.3 nM, a barely saturating dose) (Wierbowski et al., 2020), and Hh pathway activation was measured by endogenous SMO recruitment to cilia. Data were normalized between untreated cells and cells treated with saturating SAG (100%) and were fit with a three-parameter curve. Bars represent average intensity of ciliary SMO for three replicates, and error bars represent SEM. At least 300 cilia were measured per replicate. Mutants defective in SHH transfer from SCUBE2 do not rescue signaling. The W49A/L53A mutant, which affects the interface with PTCH1, is also inactive (see Figure 6).
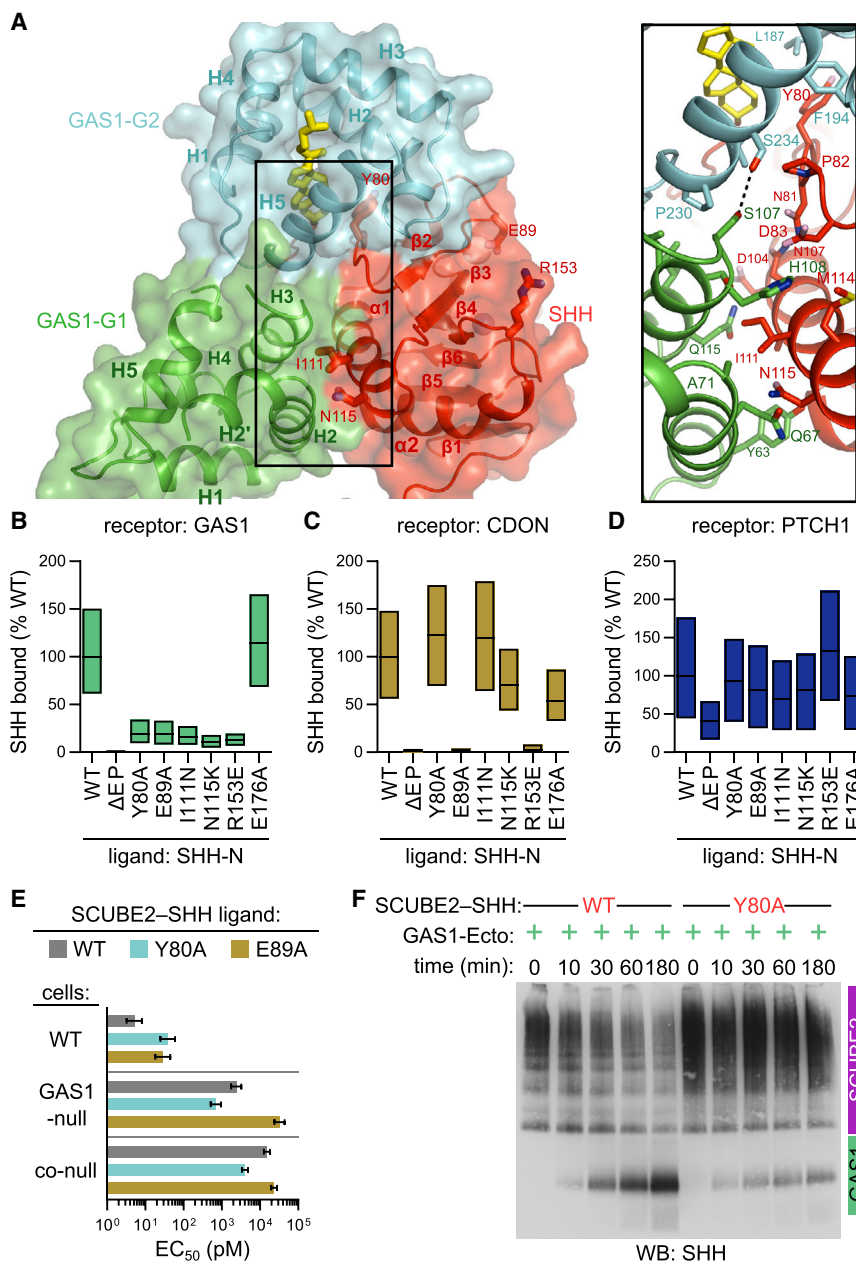
Figure 4. Human disease mutations disrupt the GAS1–SHH interface

(A) GAS1–SHH interaction interface. Left: GAS1-G1 (green) and GAS1-G2 (cyan) cooperate to grasp SHH (red). The major secondary structure elements of G1, G2, and SHH are indicated. Three SHH residues are labeled: I111 and N115 (mutated in HPE), and Y80 (implicated in GAS1–SHH interaction). Right: Close-up highlighting the point of convergence between G1, G2, and SHH. Residues mutated in HPE lie at the interaction interface.

(B) HEK293T cells expressing eGFP-tagged GAS1 were incubated with tetramethylrhodamine (TMR)-labeled palmitoylated SHH-N variants (500 nM), and bound ligand was measured by fluorescence microscopy. Boxplots show the median, and first and third quartiles of bound fluorescence. Data are normalized between binding of wild-type SHH-N to a negative control (SMO) and to wild-type GAS1 (100%). At least 300 cell objects were analyzed per condition. SHH-N species with mutations in five residues, including the three residues in (A), are defective in binding GAS1. SHH lacking the palmitoylated N-terminal peptide (ΔEP) does not bind GAS1.

(C) As in (B), but with binding to CDON. The three SHH-N mutants in (A) bind CDON normally, whereas the other two are defective.

(D) As in (B), but with binding to PTCH1. All five SHH-N mutants retain binding to PTCH1.

(E) Hh pathway activation by purified SCUBE2–SHH containing wild-type or mutant SHH, measured on wild-type, GAS1-null, and coreceptor-null cells. Bars represent best-fit EC_{50} values for a three-parameter curve, and error bars represent standard error of the fit. See Figures S8E–S8G for the dose-response curves. SHH(E89A) has a more severe signaling defect than SHH(Y80A) in GAS1-null cells, consistent with SHH(E89A) affecting both GAS1 and CDON binding, whereas SHH(Y80A) is impaired in GAS1 binding only.

(F) Purified SCUBE2–SHH (400 nM) containing wild-type SHH or SHH(Y80A) was incubated with GAS1-Ecto (2 μM) followed by native PAGE and immunoblotting. SHH transfer from SCUBE2 to GAS1 is impaired by Y80A mutation, which disrupts the GAS1–SHH interface.

of the G2 cavity (R170E) (Figure S7Q) caused a severe defect in cholesterol binding (Figures 3L and S7R). Consistent with this, GAS1(R170E) accepted SHH modified with palmitate only but not cholesterol-modified SHH species (Figure 3K). A GAS1 mutant (R170L/L183Y), in which two residues in helices H1 and H2 of G2 are changed to the analogous residues in G1 to reduce the volume of the G2 cavity, was also defective in cholesterol binding (Figures 3L, S7Q, and S7R). Both GAS1 mutants above were impaired in accepting SHH from SCUBE2, with good correlation between the rates of cholesterol and SHH transfer (Figures 3L and S7S), and they did not rescue responsiveness of coreceptor-null cells to SCUBE2–SHH (Figures 3M and S7T). These results show that cholesterol binding by GAS1 is required for SHH transfer from SCUBE2 and for Hh signaling.

SHH disease mutations affect GAS1–SHH interaction

Aside from lipid contacts, GAS1 binds two regions of the SHH globular domain (Figure 4A) in a manner distinct from CDON/BOC (McLellan et al., 2008; Kavran et al., 2010), HHIP (Bishop et al., 2009; Bosanac et al., 2009), 5E1 antibody (Maun et al., 2010), and PTCH1-B (Fuse et al., 1999; Pepinsky et al., 2000; Tukachinsky et al., 2016; Gong et al., 2018), which all exhibit Ca^{2+}-mediated binding to the SHH pseudo-active site. Helix α1 of SHH packs against H2 and H3 of GAS1-G1, whereas the loop preceding the β2 strand in SHH traverses a hydrophobic concave area near the entrance of the GAS1-G2 cholesterol-binding pocket (Figure 4A). Strikingly, two human HPE SHH mutations (I111N and N115K) (Roessler et al., 2009) affect G1–SHH interface residues (Figure 4A). Martinelli and Fan (2009) previously implicated

Developmental Cell
Article

CellPress

Figure 5. Coordination of SHH transfer from SCUBE2 to GAS1

(A) GAS1-G2–SHH interface, showing extra density extending from G2 (cyan) across the pseudo-active site of SHH (red). This density is close to the last residue built in the G2 model (C243), suggesting it represents the GAS1 tail. Two calcium ions (white spheres) and a zinc ion (pink sphere) are shown.

(B) As in (A), but with overlay of 5E1 Fab fragment (heavy chain, pink; light chain, gray) bound to SHH (PDB ID: 3MXW). GAS1–SHH and SHH–5E1 are aligned on SHH. GAS1 tail density clashes with 5E1.

(C) As in (B), but with overlay of heparin (green) bound to SHH (PDB ID: 4C4N). GAS1 tail density clashes with heparin.

(D) As in (B), but with overlay of the third fibronectin type III domain (FN3) of CDON (gold) bound to SHH (PDB ID: 3D1M). GAS1 tail density clashes with CDON.

(E) As in (B), but with overlay of PTCH1-B (orange) bound to SHH (PDB ID: 6RVD). GAS1 tail density clashes with PTCH1-B.

(F) HaloTag-GAS1 tail or HaloTag alone (negative control) were immobilized on beads, and mixed with unlipidated SHH-N, with or without preincubation with 5E1. Bound protein was analyzed by SDS-PAGE and Coomassie staining. GAS1 tail binds SHH, which is competed by 5E1.

(G) SCUBE2–SHH (500 nM) was incubated with scFv5E1 (5 µM), before or after incubation with GAS1-Ecto (2.5 µM). The mixtures were analyzed by native PAGE and immunoblotting. Preincubation with scFv5E1 greatly reduces SHH transfer from SCUBE2 to GAS1. Arrowhead indicates scFv5E1 alone.

N115K in GAS1 interaction, together with another surface mutation (Y80A), which affects the G2–SHH interface in our structure (Figure 4A). All three mutations above drastically reduce binding of palmitoylated SHH-N to GAS1 (Figures 4B, S8A, and S8B) but not to CDON, PTCH1, or 5E1 (Figures 4C, 4D, S8C, and S8D), indicating a specific defect in GAS1–SHH protein–protein contact. In contrast, two rational SHH mutants, E89A (Izzi et al., 2011) and R153E (Fuse et al., 1999), affected SHH-N binding to both GAS1 (Figures 4B and S8B) and CDON (Figures 4C and S8C).

To test the role of GAS1–SHH protein–protein contact, we measured signaling by SCUBE2 complexed with SHH mutants Y80A and E89A (Figures 4E and S8E–S8G). Mutant complexes were 10-fold less potent than SCUBE2–SHH on wild-type cells (Figure 4E) but still more potent than SCUBE2–SHH on GAS1-null cells, consistent with mutations not completely abolishing GAS1 binding (Figures 4B and S8B). SCUBE2–SHH(Y80A) and SCUBE2–SHH were equally potent on GAS1-null cells, confirming the defect was strictly GAS1-dependent; in contrast, SCUBE2–SHH(E89A) was less potent on GAS1-null cells, consistent with impaired binding to both GAS1 and CDON (Figures 4B, 4C, S8B, and S8C). As expected, all complexes had similar potency on cells lacking all coreceptors (BOC, CDON, and GAS1), consistent with an unperturbed SHH–PTCH1 interaction. Finally, SHH(Y80A) transfer from SCUBE2 to GAS1 was strongly impaired (Figure 4F), explaining the SCUBE2–SHH(Y80A) signaling defect. These results demonstrate the importance of the protein–protein GAS1–SHH interface in accepting SHH from SCUBE2 and explain SHH disease mutations. A perturbed GAS1-G2–SHH interface may also explain why tagging SHH within the C-terminal peptide leads to loss-of-function phenotypes (Chamberlain et al., 2008).

The tail of GAS1 coordinates SHH transfer from CDON–SCUBE2

Much of the GAS1 tail is dispensable for function (Figure S5I), but a portion is required (Figures 3J and S8H). Examination of the GAS1–SHH–PTCH1 cryo-EM map identifies extra density extending from the GAS1-G2 C-terminus (Figure 5A) across a region of the SHH pseudo-active site bound by many interactors (Figures 5B–5E). Although the density does not allow sequence assignment for this part of GAS1, its intensity is comparable to that of the C-terminal SHH peptide (Figure 5A). We asked whether the extra density reflects an interaction between GAS1 tail and SHH. Indeed, recombinant GAS1 tail bound unlipidated SHH (Figure 5F), which was competed by the 5E1 antibody, suggesting that the contact involves the SHH pseudo-active site (Figure 5B). Consistent with this, mutating the pseudo-active site residue R153 reduced GAS1 binding (Figure 4B).

We wondered whether GAS1 tail–SHH binding allows GAS1 to use the pseudo-active site as an initial "landing pad" for

engaging SCUBE2–SHH. Preincubating SCUBE2–SHH with 5E1 or recombinant GAS1 tail greatly reduced SHH transfer to GAS1 (Figures 5G and S8I). Additionally, a SCUBE2 complex with a SHH pseudo-active site mutant (Figure S8J; Fuse et al., 1999) showed reduced transfer to GAS1 (Figure 5H). Thus, interaction between GAS1 tail and the SHH pseudo-active site is required for SHH transfer from SCUBE2.

The GAS1 tail sequence is poorly conserved, except for a polyacidic motif (Figure S9A). Mutating acidic residues to uncharged ones (Figure S7Q) caused a striking defect in SHH transfer from SCUBE2 (Figures 3L and S7S), although cholesterol binding was unaltered (Figure S7R). Interestingly, GAS1 tail is located along a strip of basic residues in SHH (including R153) (Figures S9B and S9C), which has been shown to bind heparin (Figure 5C; Whalen et al., 2013). We propose that binding of GAS1 tail to the pseudo-active site depends on electrostatic interactions between the polyacidic motif and the SHH basic strip. Consistent with this idea, three GAS1 mutations (G259R, D270Y, and D288G) found in HPE (Ribeiro et al., 2010; Pineda-Alvarez et al., 2012) decrease the net negative charge of the tail.

Finally, we examined the role of the GAS1 tail in SHH transfer from the ternary CDON–SCUBE2–SHH complex to GAS1 (Figure 1A; Wierbowski et al., 2020). CDON and GAS1 compete for SHH (McLellan et al., 2008), which permits dissociation of CDON–SCUBE2 from GAS1–SHH during transfer (Wierbowski et al., 2020), but the mechanism is unknown. While SHH bound to the third fibronectin type III repeat of CDON (CDON-FN3) (McLellan et al., 2008) can be superimposed on the modeled GAS1–SHH–PTCH1 complex without steric clash, the GAS1 tail density overlaps with CDON-FN3 (Figure 5D). Indeed, SHH transfer from CDON–SCUBE2–SHH to GAS1 was abolished when the GAS1 tail polyacidic motif was replaced with uncharged residues (Figure 5I), as was signaling by SCUBE2–SHH in cells (Figure 5J). These data suggest that electrostatic GAS1 tail–SHH interactions displace CDON, followed by SHH lipid transfer to GAS1 and consequent SHH disengagement from SCUBE2 (Figure 5K).

Transient GAS1–PTCH1 contact mediates SHH delivery to PTCH1

The GAS1–PTCH1 interface forms between helix H1 and adjacent regions in GAS1-G1, and the tips of Loops I–III in PTCH1-ECD1 (Figures 6A and S9D). The interface involves hydrophobic interactions and shape complementarity. The side chains of W49 and L53 in GAS1-G1 helix H1 insert into the hydrophobic cleft in PTCH1-ECD1, above the CHS molecule, and W49 forms a π-cation interaction with K241 of PTCH1 (Xenopus numbering). No major conformational change is observed in PTCH1-ECD1 upon GAS1 binding (RMSD of 0.67 Å over the

---

(H) Purified SCUBE2–SHH containing wild-type SHH or SHH with three mutations in the pseudo-active site (3M) were assayed for transfer to GAS1 as in (G). The 3M mutant exhibits severely impaired transfer.

(I) Purified CDON–SCUBE2–SHH (400 nM) was incubated with GAS1-Ecto (2 μM) or a variant containing mutations in the polyacidic motif of the tail (Tail*). Tail mutations block SHH transfer from SCUBE2.

(J) Coreceptor-null cells rescued with GAS1 or GAS1-Tail* were treated with SCUBE2–SHH and Hh pathway activation was measured as in Figure 3M. At least 150 cilia were measured per replicate. GAS1-Tail* does not rescue responsiveness to SCUBE2–SHH.

(K) Model for SHH transfer to GAS1. GAS1 tail displaces CDON bound to the SHH pseudo-active site. This is followed by transfer of SHH lipids from SCUBE2 to GAS1, and then dissociation of CDON–SCUBE2 from GAS1–SHH.
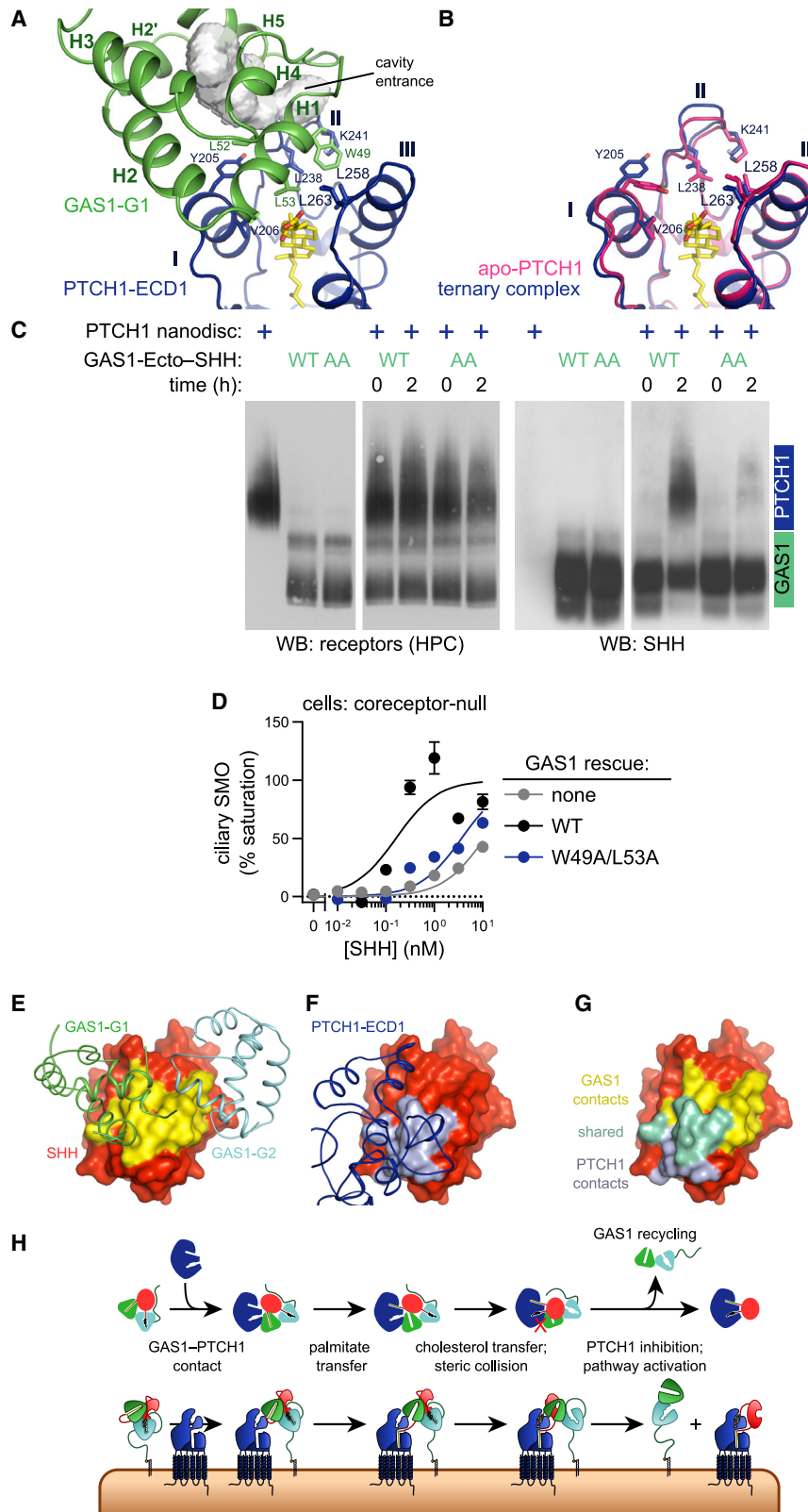
Figure 6. Mechanism of SHH transfer from GAS1 to PTCH1

(A) GAS1-G1–PTCH1 interface. PTCH1-ECD1 (blue) utilizes three fingers [I–III, which form the sterol-binding pocket (SBP)] to grasp helix H1 of GAS1-G1 (green). Important contact residues (4.5-Å cutoff) are labeled. CHS (yellow) in the SBP highlights that GAS1-G1 does not completely seal the SBP, leaving it accessible for transfer of SHH cholesterol. The palmitate-binding pocket of G1 is shown (white volume), its opening facing downward.

(B) Overlay of PTCH1-ECD1 bound to GAS1–SHH (blue) and PTCH1-ECD1 in apo-PTCH1 (pink). Only residue Y205 moves, to create space for GAS1-G1.

(C) Purified GAS1-Ecto–SHH complexes (100 nM) were incubated with PTCH1 nanodiscs (300 nM), followed by native PAGE and immunoblotting. Disruption of the GAS1–PTCH1 interface in the W49A/L53A mutant (AA) strongly impairs SHH transfer from GAS1 to PTCH1.

(D) Dose response of purified SCUBE2–SHH on coreceptor-null cells rescued with wild-type GAS1 or GAS1(W49A/L53A), measured as in Figure 3M. Data are represented as percentage of the theoretical maximum of the curve fit (% saturation). At least 250 cilia were measured per replicate. Curves for no rescue and rescue with wild-type GAS1 are shared with Figure S7T, as these mutants were assayed simultaneously.

(E) GAS1 (G1 green and G2 cyan) binding to SHH (molecular surface, red). Regions of SHH that interact with GAS1 are shown in yellow.

(F) PTCH1-A (blue) binding to SHH (molecular surface, red). Regions of SHH that interact with PTCH1-A are shown in light blue.

(G) Overlay of the binding surfaces in (E) and (F), showing a shared interaction surface in green.

(H) Model for SHH transfer from GAS1 to PTCH1. Initial protein–protein contact between GAS1-G1 and PTCH1-ECD1 is followed by transfer of SHH lipids to PTCH1. The cholesteryl moiety disrupts the GAS1–PTCH1 contact, leading to GAS1 dissociation.

Cαs of PTCH1 residues 195–280), except the slight outward movement of Loop II and the Y205 side-chain rotameric switch, which makes room for GAS1 (Figure 6B).

We tested the role of the GAS1–PTCH1 interface in SHH delivery and signaling. GAS1(W49A/L53A)-Ecto–SHH (Figure S9E) showed drastically reduced SHH transfer to PTCH1 (Figure 6C). Consistent with this defect, GAS1(W49A/L53A) failed to rescue responsiveness of coreceptor-null cells to SCUBE2–SHH (Figures 3M and 6D), demonstrating that the interface is critical for signaling. Importantly, GAS1(W49A/L53A)-Ecto bound cholesterol (Figure S7R) and accepted SHH from SCUBE2 (Figure S7S) normally, indicating specificity of the observed defects to the GAS1–PTCH1 interaction.

How does GAS1 binding to PTCH1 trigger SHH release? Intrinsic tryptophan fluorescence of GAS1 changes upon binding palmitoylated SHH EP (Figure S9F). We interpret this as due to W49 movement, since the only other tryptophan (W103) is located in the disordered loop connecting H2′ and H3 of G1 (Figure S9A), which is dispensable for SHH binding (Figure S5I). Thus, W49 might function as a switch (Figure S9G): when GAS1 binds SHH, W49 may adopt a "flip-in" rotameric conformation to enclose the palmitate; W49 flips out upon GAS1 binding PTCH1, allowing palmitate to move to PTCH1. SHH transfer is then completed when cholesterol moves from GAS1-G2 to the SBP in PTCH1-ECD1. While GAS1-G1 occupies most of the SBP entrance (Figure 6A), it leaves an opening near the sterol head group, perhaps permitting access of SHH cholesterol.

After SHH handoff, GAS1 dissociates from PTCH1 and is recycled (Wierbowski et al., 2020). Our structure suggests a mechanism for GAS1 dissociation. In SHH–PTCH1-A (Qi et al., 2018b), SHH helix α1 contacts PTCH1-ECD1, via an interface overlapping extensively with the GAS1-G1–SHH interface (Figures 6E–6G). The overlap includes two SHH residues mutated in HPE (I111 and N115), required for binding both GAS1 (Figures 4A and 4B) and PTCH1-A (Qi et al., 2018b). Perhaps following SHH lipid transfer to PTCH1, GAS1–SHH stability is greatly decreased, allowing SHH helix α1 to engage PTCH1-ECD1 and thereby release GAS1 (Figure 6H).

PTCH1 dimerization occurs downstream of SHH transfer from GAS1 and causes PTCH1 internalization

SHH–PTCH1 structures show SHH engaging two PTCH1 molecules, PTCH1-A and PTCH1-B (Qi et al., 2018a; Qian et al., 2018; Rudolf et al., 2019). We refer to this PTCH1-bridging activity of SHH as ligand-induced PTCH1 dimerization, although PTCH1-A and PTCH1-B might be part of higher-order unliganded oligomers. Our structure implies that the PTCH1-B interaction mode occurs only after SHH is transferred from GAS1 to PTCH1 via the PTCH1-A mode. First, GAS1 tail clashes with the PTCH1-B interface (Figure 5E), suggesting GAS1–SHH cannot interact with PTCH1-B. Furthermore, docking PTCH1-B onto SHH in GAS1–SHH–PTCH1 results in substantial clash between the TMDs of PTCH1 molecules (Figure 7A); accordingly, we did not observe GAS1–SHH–PTCH1 complexes bound via the PTCH1-B mode in our cryo-EM samples. Finally, the PTCH1-B binding mode is dispensable for SHH transfer from GAS1 to PTCH1 (Figure 1D). These results suggest that SHH induces PTCH1 dimerization only after transfer from GAS1 to PTCH1-A.

SHH engagement of PTCH1-A suffices for PTCH1 inhibition and Hh signaling (Tukachinsky et al., 2016). The PTCH1-B interaction mode was thought to be required for PTCH1 inhibition because 5E1 antibody blocks signaling *in vivo* (Ericson et al., 1996) and SHH-N activity in cultured cells (Maun et al., 2010). We find that 5E1 also antagonizes SCUBE2–SHH signaling (Figure S9H); however, this is sufficiently explained by blocking SHH transfer to GAS1 (Figure 5G). To test the role of the PTCH1-B interaction mode, we assayed SCUBE2–SHH containing SHH pseudo-active site mutants (Fuse et al., 1999). The mutant complexes were completely inactive on coreceptor-null cells, in contrast to SCUBE2–SHH (Figure 7B), indicating that the SHH mutations abolished the PTCH1-B interaction, which is necessary for SCUBE2–SHH to engage PTCH1 in the absence of coreceptors (Wierbowski et al., 2020). The SCUBE2–SHH mutants exhibited greatly reduced potency on wild-type cells (Figure 7C), consistent with impaired SHH transfer from SCUBE2 to GAS1 (Figure 5H); however, the mutants were still active at high dose, indicating that the PTCH1-B binding mode is not absolutely necessary for SCUBE2–SHH signaling when coreceptors are present.

We also tested SCUBE2–SHH pseudo-active site mutants in ligand-induced PTCH1 internalization from cilia, a process dependent on the PTCH1-B binding mode (Tukachinsky et al., 2016). Both wild-type and mutant SCUBE2–SHH caused SMO accumulation in cilia, indicative of Hh pathway activation (Figure 7D). Strikingly, in contrast to SCUBE2–SHH, which reduced PTCH1 in cilia, SCUBE2–SHH mutants led to PTCH1 accumulation in cilia (Figure 7D), similar to palmitoylated SHH EP (Tukachinsky et al., 2016). This result indicates that the PTCH1-B interaction is necessary for ligand-induced PTCH1 internalization.

Finally, we asked what leads to SHH–PTCH1 internalization, since SHH binding does not cause any major conformational change in PTCH1 (Figures 2D and S5A–S5F; Qi et al., 2018a; Qian et al., 2018). Neither SHH-N^ΔEP (Figure S8A), which lacks the palmitoylated EP and cannot bind PTCH1-A, nor the pseudo-active site mutant SHH-N^3M (Figure S9I), which cannot bind PTCH1-B, caused PTCH1 internalization, in contrast to wild-type SHH-N (Figure 7D). Thus, both PTCH1-A and PTCH1-B binding modes are required for internalization, suggesting it is triggered by SHH bridging PTCH1. We tested this model in two experiments. First, we measured PTCH1 internalization as function of SHH-N concentration, reasoning that increasing SHH-N should reduce 1:2 SHH–PTCH1 complexes by trapping PTCH1 as 1:1 SHH–PTCH1-A and SHH–PTCH1-B. When SHH-N is titrated, ciliary PTCH1 levels drop precipitously but start increasing at higher SHH-N dose (Figure 7E), as expected if ligand-induced dimerization were the signal for internalization. Second, we asked whether artificial PTCH1 dimerization suffices to drive internalization. To this end, we generated synthetic ligands bearing one or two copies of the anti-PTCH1 nanobody, TI23 (Figures S9J and S9K; Zhang et al., 2020). At low concentration, the dimerized nanobody, which should be able to bind two PTCH1 molecules, induced PTCH1 internalization to a similar extent as unlipidated SHH ligand, in contrast to the monomeric nanobody (Figure 7F). Collectively, our data suggest that SHH is transferred from GAS1 to PTCH1-A, causing PTCH1 inhibition, followed by PTCH1-B binding, which triggers clearance of SHH–PTCH1 from cilia (Figure 7G).
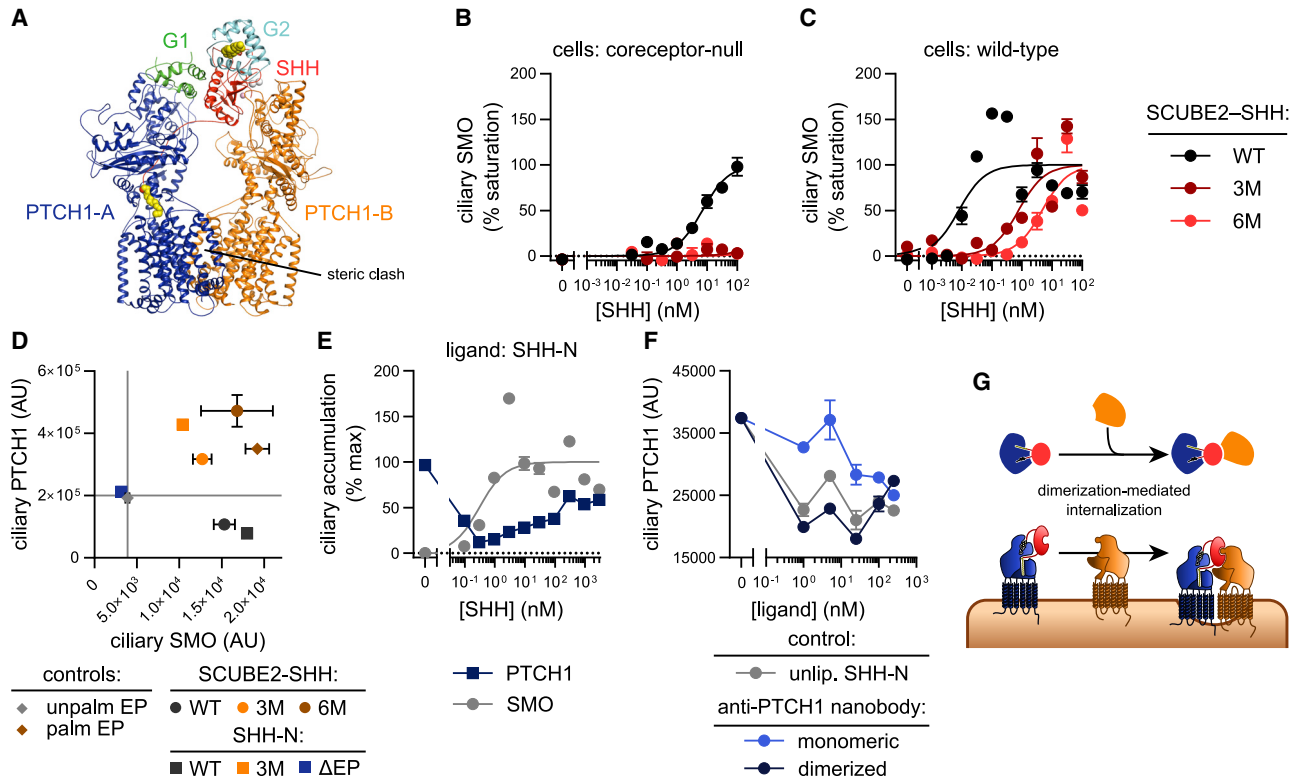
Developmental Cell
Article

CellPress

Figure 7. SHH-induced PTCH1 dimerization causes PTCH1 internalization

(A) GAS1–SHH–PTCH1 (G1, green; G2, cyan; SHH, red; and PTCH1-A, blue) overlaid on SHH–PTCH1-B (orange, PDB ID: 6RVD), aligned on SHH. Binding of PTCH1-B to SHH in the ternary complex would lead to steric collision between TMDs of the two PTCH1 molecules, which would also not be in the same plane.

(B) Dose response of purified SCUBE2–SHH containing wild-type SHH or SHH with three (3M) or six (6M) mutations in the pseudo-active site, measured on coreceptor-null cells as in Figure 6D. At least 300 cilia were measured per replicate. In the absence of coreceptors, the PTCH1-B interface is essential for Hh signaling.

(C) As in (B), but for wild-type cells. The PTCH1-B interface is not absolutely required for signaling when coreceptors are present.

(D) PTCH1-null MEFs rescued with mCherry-tagged PTCH1 were treated with SCUBE2–SHH complexes (circles), palmitoylated-only SHH-N variants (squares), or synthetic effector peptide (EP) with or without palmitoylation (diamonds). Ciliary levels of PTCH1 and SMO were measured by fluorescence microscopy and automated image analysis. Points represent average ciliary intensities for three replicates, and error bars represent SEM. At least 200 cilia were measured per replicate. Wild-type SHH species (dark gray) cause SMO accumulation and PTCH1 loss from cilia, whereas SHH species defective in PTCH1-B interaction, including the palmitoylated EP (orange and brown points), cause both SMO and PTCH1 accumulation. As expected, unpalmitoylated EP and SHH-N lacking the EP (ΔEP) are inactive.

(E) As in (D), but with titration of purified palmitoylated SHH-N. Data for SMO are represented as a percentage of the theoretical maximum, fit as in (B), whereas data for PTCH1 are represented as a percentage of the initial level in untreated cells, with lines connecting sequential points. High doses of SHH-N reverse PTCH1 internalization from cilia.

(F) As in (D), but NIH 3T3 cells expressing eGFP-tagged PTCH1 and mCherry-tagged SMO were treated with purified monomeric or dimerized TI23 anti-PTCH1 nanobody (Zhang et al., 2020) or with unlipidated SHH-N (positive control). Low levels of dimerized anti-PTCH1 nanobody induce PTCH1 exit, similar to un-lipidated SHH-N.

(G) Model of ligand-induced SHH–PTCH1 internalization. SHH transferred from GAS1 forms SHH–PTCH1-A complex in which PTCH1 is inactive, triggering signaling. SHH–PTCH1-A interacts with PTCH1-B, leading to internalization from the cell surface.

DISCUSSION

The present work defines the mechanism of SHH–PTCH1 complex assembly, which triggers the Hh pathway. The dually lipidated SHH morphogen is released from cells bound to SCUBE2. CDON/BOC recruit the SCUBE2–SHH complex to target cells via contacts with both components (Wierbowski et al., 2020; Figure 1A). GAS1 then coordinates two lipid-dependent transfers: unloading SHH from CDON/BOC–SCUBE2 (Figure 5K), followed by SHH handoff to PTCH1 (Figure 6H). Our results support the following mechanism for GAS1. First, GAS1 is recruited to CDON/BOC–SCUBE2–SHH by the GAS1 tail polyacidic motif binding to the SHH pseudo-active site, thus displacing CDON/BOC. Transfer of SHH lipids from SCUBE2 to GAS1 then occurs, resulting in GAS1–SHH dissociation from SCUBE2–CDON/BOC. Second, GAS1-G1 helix H1 engages PTCH1, facilitating transfer of SHH lipids to PTCH1, via the PTCH1-A interaction mode; this suffices to inactivate PTCH1 and activate Hh signaling. As PTCH1-A competes with GAS1-G1 for binding SHH, GAS1 dissociates from SHH–PTCH1-A and is recycled (Figure 6H). Finally, GAS1 displacement permits engagement of SHH with a second PTCH1 molecule, via the PTCH1-B interaction mode, leading to internalization of the 1:2 SHH–PTCH1 complex (Figure 7G; Qi et al., 2018a; Qian et al., 2018; Rudolf et al., 2019).

Lipid moieties play a key role in sequential SHH transfer between mutually exclusive binding partners. GAS1 illustrates a general mechanism for how SHH-binding proteins achieve interactions that are specific and sufficiently dynamic for SHH exchange. GAS1 binds both SHH palmitate and cholesterol, and also makes broad contacts across the SHH globular domain. Specific SHH recognition by GAS1 thus arises through avidity conferred by multiple low-affinity contacts. This architecture is amenable to rapid ligand exchange, as shown by the role of GAS1 tail in SHH receipt from SCUBE2, and that of the GAS1–PTCH1 interaction in SHH delivery to PTCH1. Interestingly, a recent structure of DISP1 (Wang et al., 2021) shows a highly charged unstructured loop engaging the SHH pseudo-active site in a similar manner to the GAS1 tail, suggesting that low-affinity interactions might also coordinate SHH transfer from DISP1 to SCUBE2. We speculate that SHH movement from DISP1 to SCUBE2 to GAS1 to PTCH1, is driven, at least in part, by incrementally higher affinity for SHH lipids, particularly cholesterol (Wierbowski et al., 2020). Although SHH cholesterol is not required for inhibiting PTCH1, it is necessary for controlled deployment of SHH by DISP1/SCUBE2 and provides a handle for directional transfers. We expect avidity-based mechanisms for ligand exchange between mutually exclusive interactors to control ligand movement in other signaling pathways as well.

Structural analysis of GAS1 permits some speculation on its divergence from GFRα coreceptors. In GFRα proteins, D2 and D3 domains pack against each other to form an extended module that binds both ligand and the tyrosine kinase receptor RET. In GAS1, the homologous G1 and G2 domains are more loosely connected, consistent with repurposing as SHH lipid-binding modules. While GFRα proteins are the linchpin in a ternary ligand–coreceptor–receptor complex, GAS1 is physically uncoupled from both upstream SCUBE2 (from which it accepts SHH) and downstream PTCH1 (to which it donates SHH). Thus GAS1 has evolved unique binding modes, involving dual lipid recognition and transient association with other Hh pathway components. Notably, both SCUBE2 and GAS1 are lipid-dependent SHH-binding proteins found only in vertebrates, suggesting possible coevolution.

While SCUBE proteins are critical for DISP1-dependent SHH release, GAS1 can also accept SHH from DISP1 (Figure S9L). We speculate this might be important for short-range Hh signaling (autocrine and juxtacrine), as opposed to long-range signaling promoted by SCUBE. Several structures of DISP1 in complex with SHH have been reported (Chen et al., 2020; Li et al., 2021; Wang et al., 2021) but none elucidate how SHH is transferred to acceptors, likely because they interface with DISP1 only transiently. Occlusion of individual lipid-binding sites may facilitate the generation of "trapped" transfer intermediates, analogous to the intermediate described in this study, for use in future investigations of SHH transfer from DISP1 to extracellular acceptors.

Because SHH–PTCH1-A binding is necessary and sufficient to activate Hh signaling (Tukachinsky et al., 2016), the role of SHH–PTCH1-B binding had remained elusive. Our results indicate it is specifically required for ligand–receptor internalization. How does SHH-binding two PTCH1 molecules signal internalization in the absence of conformational change in PTCH1 protomers? We speculate that SHH bridging facilitates interactions between the cytoplasmic domains of PTCH1 protomers, leading to recognition by the endocytosis machinery. Consistent with this idea, the cytoplasmic domain contains sequences recognized by HECT E3 ligases involved in PTCH1 turnover (Huang et al., 2013; Yue et al., 2014; Kim et al., 2015), and interactions between cytoplasmic domains were implicated in ligand-induced PTCH1 exit from cilia (Fleet et al., 2016). Interestingly, single-molecule studies in live cells show that SHH reduces the free diffusive motion of some PTCH1 particles while increasing the diffusion coefficient of remaining particles (Weiss et al., 2019). It is tempting to imagine that the two particle populations correspond to 1:2 and 1:1 SHH–PTCH1 complexes. Finally, although it is unclear how SHH-induced PTCH1 dimers relate to the higher-order PTCH1 assemblies observed in vitro (Qian et al., 2018), it is notable that the PTCH1 construct used by Qian et al. contained large cytoplasmic regions deleted in other PTCH1 structures. Future studies will be necessary to probe SHH-induced PTCH1 dimerization in cells, to understand its relationship with PTCH1 oligomerization and motional dynamics, and to determine how cytoplasmic domains control PTCH1 internalization.

A key mechanism for graded Hh signaling during development is negative feedback (Chen and Struhl, 1996) by downregulation of SHH coreceptors (Tenzen et al., 2006; Allen et al., 2007; Martinelli and Fan, 2007) and upregulation of antagonists (Marigo and Tabin, 1996; Motoyama et al., 1998; Chuang and McMahon, 1999). Our results can explain how cells switch from a signaling regime highly sensitive to ligand, to one less sensitive and geared toward ligand clearance (Chen and Struhl, 1996; Briscoe et al., 2001; Holtz et al., 2013). Unstimulated cells express CDON/BOC and GAS1, which permit detection of picomolar SCUBE2–SHH (Wierbowski et al., 2020). In this regime, SHH moves from SCUBE2 through GAS1 to PTCH1-A, recruiting PTCH1-B secondarily, for ligand clearance. SHH-stimulated cells downregulate CDON/BOC and GAS1 and upregulate PTCH1. Without coreceptors, SCUBE2–SHH must be recruited through direct interaction with PTCH1-B, which occurs at much higher concentration. The PTCH1-A interaction is perhaps engaged second, displacing SCUBE2 and triggering signaling and ligand clearance. This activation route is dramatically less sensitive to SHH.

Our results illustrate a surprising coreceptor mechanism in which GAS1 catalyzes the formation of the ligand–receptor complex rather than being a stable component of it. Similar catalytic roles have been reported for cell-surface proteoglycans. In TGFβ signaling, betaglycan scaffolds association of the TGFβ ligand with type II receptor but is subsequently displaced upon type I receptor binding and formation of the final ligand–receptor complex (López-Casillas et al., 1993). Cell-surface heparan sulfate plays a similar role in BMP signaling, catalyzing recruitment, in trans, of a type II receptor to the BMP–type I receptor complex (Kuo et al., 2010). The role of sulfated proteoglycans in catalyzing ligand–receptor assembly has been previously noted (Lander, 1998), and it is striking that GAS1 coordinates SHH receipt from SCUBE2 by engaging the pseudo-active site through a heparin-mimetic polyacidic motif. We speculate that the catalytic coreception paradigm exemplified by GAS1 and proteoglycans is likely to be widespread in signaling pathways.

Developmental Cell
Article

CellPress

Limitations of the study

(1) We describe the mechanism of GAS1-catalyzed assembly of SHH–PTCH1. We define the role of GAS1–SHH interactions in SHH receipt from SCUBE2 and GAS1–PTCH1 interactions in SHH delivery to PTCH1. It is unclear how SHH lipids engage GAS1/PTCH1 and whether palmitoyl and cholesteryl moieties are transferred in a defined sequence.

(2) Our study does not address the nature of unliganded PTCH1 *in vivo*, which is unknown. Biochemical experiments indicate that a fraction of unliganded PTCH1 purified in detergent is oligomeric (Qian et al., 2018), but whether such species exist in cells and what role they might play in SHH reception and Hh signaling remains unresolved.

(3) The lipidation status of SHH mutants contained in purified SCUBE2–SHH complexes was not directly quantified. Such measurements will be required for further validation of our model of successive SHH handoff from SCUBE2 to GAS1 to PTCH1.

(4) It is unknown how GAS1-catalyzed SHH–PTCH1 complex formation is regulated *in vivo.* Future studies will determine how this mechanism modulates signaling in various tissue contexts.

STAR★METHODS

Detailed methods are provided in the online version of this paper and include the following:

- KEY RESOURCES TABLE
- RESOURCE AVAILABILITY
  - Lead contact
  - Materials availability
  - Data and code availability
- EXPERIMENTAL MODEL AND SUBJECT DETAILS
  - Cell culture
  - Generation of stable cell lines
- METHOD DETAILS
  - Antibodies
  - DNA constructs
  - Protein expression and purification
  - Cryo-EM sample preparation and data collection
  - Cryo-EM image processing
  - Model building, refinement, and analysis
  - Immunoblotting
  - Immunofluorescence microscopy of ciliary SMO and PTCH1
  - Site-specific labeling of HT7 fusion proteins
  - Preparation of fluorescent streptavidin peptide ligands
  - Cell-based ligand-binding assays
  - Blue native PAGE SHH transfer assays
  - Radioactive lipid transfer assays
  - Bead-based SHH transfer assays
  - Luciferase-based SHH release assays
  - GAS1 tail immunoprecipitations
  - Isothermal titration calorimetry
  - Tryptophan fluorescence spectroscopy
  - Gel and blot image processing
- QUANTIFICATION AND STATISTICAL ANALYSIS

AUTHOR CONTRIBUTIONS

B.M.W., P.H., and A.S. designed reagents and experiments. B.M.W. generated reagents, purified proteins, and performed activity assays, ligand-binding experiments, and *in vitro* transfer experiments. C.C. purified PTCH1, assembled PTCH1 amphipols, and performed *in vitro* transfer experiments. P.H. purified PTCH1, assembled PTCH1 nanodiscs and GAS1–SHH–PTCH1 complex, and built and analyzed structure models. T.L. prepared cryo-EM grids and acquired cryo-EM images. T.L. and J.J. analyzed cryo-EM data. S.G.-L. purified proteins and performed ITC and Trp fluorescence measurements. A.S. generated reagents and performed experiments. B.M.W. performed image analysis. All authors analyzed data. B.M.W., P.H., J.J., and A.S. wrote the manuscript, with input from all authors.

DECLARATION OF INTERESTS

The authors declare no competing interests.

SUPPORTING CITATIONS

The following references appear in the supplemental information: Porter et al., (1996a).

REFERENCES

Adams, P.D., Afonine, P.V., Bunkóczi, G., Chen, V.B., Davis, I.W., Echols, N., Headd, J.J., Hung, L.W., Kapral, G.J., Grosse-Kunstleve, R.W., et al. (2010). Phenix: a comprehensive Python-based system for macromolecular structure solution. Acta Crystallogr. D Biol. Crystallogr. *66*, 213–221.

Alcedo, J., Ayzenzon, M., Von Ohlen, T., Noll, M., and Hooper, J.E. (1996). The Drosophila smoothened gene encodes a seven-pass membrane protein, a putative receptor for the hedgehog signal. Cell *86*, 221–232.

Allen, B.L., Song, J.Y., Izzi, L., Althaus, I.W., Kang, J.S., Charron, F., Krauss, R.S., and McMahon, A.P. (2011). Overlapping roles and collective requirement for the coreceptors GAS1, CDO, and BOC in SHH pathway function. Dev. Cell *20*, 775–787.

Allen, B.L., Tenzen, T., and McMahon, A.P. (2007). The Hedgehog-binding proteins Gas1 and Cdo cooperate to positively regulate Shh signaling during mouse development. Genes Dev. *21*, 1244–1257.

Beachy, P.A., Cooper, M.K., Young, K.E., von Kessler, D.P., Park, W.J., Hall, T.M., Leahy, D.J., and Porter, J.A. (1997). Multiple roles of cholesterol in hedgehog protein biogenesis and signaling. Cold Spring Harb. Symp. Quant. Biol. *62*, 191–204.

Beachy, P.A., Hymowitz, S.G., Lazarus, R.A., Leahy, D.J., and Siebold, C. (2010). Interactions between Hedgehog proteins and their binding partners come into view. Genes Dev. 24, 2001–2012.

Bishop, B., Aricescu, A.R., Harlos, K., O'Callaghan, C.A., Jones, E.Y., and Siebold, C. (2009). Structural insights into hedgehog ligand sequestration by the human hedgehog-interacting protein HHIP. Nat. Struct. Mol. Biol. 16, 698–703.

Bosanac, I., Maun, H.R., Scales, S.J., Wen, X., Lingel, A., Bazan, J.F., de Sauvage, F.J., Hymowitz, S.G., and Lazarus, R.A. (2009). The structure of SHH in complex with HHIP reveals a recognition role for the Shh pseudo active site in signaling. Nat. Struct. Mol. Biol. 16, 691–697.

Braberg, H., Webb, B.M., Tjioe, E., Pieper, U., Sali, A., and Madhusudhan, M.S. (2012). SALIGN: a web server for alignment of multiple protein sequences and structures. Bioinformatics Oxf. Engl. 28, 2072–2073.

Briscoe, J., Chen, Y., Jessell, T.M., and Struhl, G. (2001). A hedgehog-insensitive form of patched provides evidence for direct long-range morphogen activity of sonic hedgehog in the neural tube. Mol. Cell 7, 1279–1291.

Cabrera, J.R., Sanchez-Pulido, L., Rojas, A.M., Valencia, A., Mañes, S., Naranjo, J.R., and Mellström, B. (2006). Gas1 is related to the glial cell-derived neurotrophic factor family receptors alpha and regulates Ret signaling. J. Biol. Chem. 281, 14330–14339.

Chamberlain, C.E., Jeong, J., Guo, C., Allen, B.L., and McMahon, A.P. (2008). Notochord-derived Shh concentrates in close association with the apically positioned basal body in neural target cells and forms a dynamic gradient during neural patterning. Development 135, 1097–1106.

Chang, D.T., López, A., von Kessler, D.P., Chiang, C., Simandl, B.K., Zhao, R., Seldin, M.F., Fallon, J.F., and Beachy, P.A. (1994). Products, genetic linkage and limb patterning activity of a murine hedgehog gene. Development 120, 3339–3353.

Chen, H., Liu, Y., and Li, X. (2020). Structure of human Dispatched-1 provides insights into Hedgehog ligand biogenesis. Life Sci. Alliance 3.

Chen, J.K., Taipale, J., Young, K.E., Maiti, T., and Beachy, P.A. (2002). Small molecule modulation of smoothened activity. Proc. Natl. Acad. Sci. U S A 99, 14071–14076.

Chen, Y., and Struhl, G. (1996). Dual roles for patched in sequestering and transducing Hedgehog. Cell 87, 553–563.

Chong, S., Mersha, F.B., Comb, D.G., Scott, M.E., Landry, D., Vence, L.M., Perler, F.B., Benner, J., Kucera, R.B., Hirvonen, C.A., et al. (1997). Single-column purification of free recombinant proteins using a self-cleavable affinity tag derived from a protein splicing element. Gene 192, 271–281.

Chuang, P.T., and McMahon, A.P. (1999). Vertebrate Hedgehog signalling modulated by induction of a Hedgehog-binding protein. Nature 397, 617–621.

Creanga, A., Glenn, T.D., Mann, R.K., Saunders, A.M., Talbot, W.S., and Beachy, P.A. (2012). Scube/You activity mediates release of dually lipid-modified Hedgehog signal in soluble form. Genes Dev. 26, 1312–1325.

de Antonio, C., Martínez del Pozo, A., Mancheño, J.M., Oñaderra, M., Lacadena, J., Martínez-Ruiz, A., Pérez-Cañadillas, J.M., Bruix, M., and Gavilanes, J.G. (2000). Assignment of the contribution of the tryptophan residues to the spectroscopic and functional properties of the ribotoxin alpha-sarcin. Proteins 41, 350–361.

Echelard, Y., Epstein, D.J., St-Jacques, B., Shen, L., Mohler, J., McMahon, J.A., and McMahon, A.P. (1993). Sonic hedgehog, a member of a family of putative signaling molecules, is implicated in the regulation of CNS polarity. Cell 75, 1417–1430.

Emsley, P., Lohkamp, B., Scott, W.G., and Cowtan, K. (2010). Features and development of coot. Acta Crystallogr. D Biol. Crystallogr. 66, 486–501.

Ericson, J., Morton, S., Kawakami, A., Roelink, H., and Jessell, T.M. (1996). Two critical periods of Sonic Hedgehog signaling required for the specification of motor neuron identity. Cell 87, 661–673.

Fleet, A., Lee, J.P., Tamachi, A., Javeed, I., and Hamel, P.A. (2016). Activities of the cytoplasmic domains of Patched-1 modulate but are not essential for the regulation of canonical hedgehog signaling. J. Biol. Chem. 291, 17557–17568.

Fuse, N., Maiti, T., Wang, B., Porter, J.A., Hall, T.M., Leahy, D.J., and Beachy, P.A. (1999). Sonic hedgehog protein signals not as a hydrolytic enzyme but as an apparent ligand for patched. Proc. Natl. Acad. Sci. U S A 96, 10992–10999.

García-Linares, S., Maula, T., Rivera-de-Torre, E., Gavilanes, J.G., Slotte, J.P., and Martínez-Del-Pozo, Á. (2016). Role of the tryptophan residues in the Specific Interaction of the Sea Anemone Stichodactyla helianthus's Actinoporin Sticholysin II with Biological Membranes. Biochemistry 55, 6406–6420.

Gong, X., Gong, X., Qian, H., Cao, P., Zhao, X., Zhou, Q., and Lei, J. (2018). Structural basis for the recognition of Sonic Hedgehog by human Patched1. Science 361, eaas8935.

Goodrich, L.V., Milenković, L., Higgins, K.M., and Scott, M.P. (1997). Altered neural cell fates and medulloblastoma in mouse patched mutants. Science 277, 1109–1113.

Hall, T.M., Porter, J.A., Beachy, P.A., and Leahy, D.J. (1995). A potential catalytic site revealed by the 1.7-A crystal structure of the amino-terminal signalling domain of Sonic hedgehog. Nature 378, 212–216.

Hollway, G.E., Maule, J., Gautier, P., Evans, T.M., Keenan, D.G., Lohs, C., Fischer, D., Wicking, C., and Currie, P.D. (2006). Scube2 mediates Hedgehog signalling in the zebrafish embryo. Dev. Biol. 294, 104–118.

Holtz, A.M., Peterson, K.A., Nishi, Y., Morin, S., Song, J.Y., Charron, F., McMahon, A.P., and Allen, B.L. (2013). Essential role for ligand-dependent feedback antagonism of vertebrate hedgehog signaling by PTCH1, PTCH2 and HHIP1 during neural patterning. Development 140, 3423–3434.

Hsu, J.Y., Crawley, S., Chen, M., Ayupova, D.A., Lindhout, D.A., Higbee, J., Kutach, A., Joo, W., Gao, Z., Fu, D., et al. (2017). Non-homeostatic body weight regulation through a brainstem-restricted receptor for GDF15. Nature 550, 255–259.

Huang, P., Nedelcu, D., Watanabe, M., Jao, C., Kim, Y., Liu, J., and Salic, A. (2016). Cellular cholesterol directly activates smoothened in hedgehog signaling. Cell 166, 1176–1187.e14.

Huang, S., Zhang, Z., Zhang, C., Lv, X., Zheng, X., Chen, Z., Sun, L., Wang, H., Zhu, Y., Zhang, J., et al. (2013). Activation of Smurf E3 ligase promoted by smoothened regulates hedgehog signaling through targeting patched turnover. PLoS Biol. 11, e1001721.

Humke, E.W., Dorn, K.V., Milenkovic, L., Scott, M.P., and Rohatgi, R. (2010). The output of Hedgehog signaling is controlled by the dynamic association between Suppressor of Fused and the Gli proteins. Genes Dev. 24, 670–682.

Ingham, P.W., and McMahon, A.P. (2001). Hedgehog signaling in animal development: paradigms and principles. Genes Dev. 15, 3059–3087.

Izzi, L., Lévesque, M., Morin, S., Laniel, D., Wilkes, B.C., Mille, F., Krauss, R.S., McMahon, A.P., Allen, B.L., and Charron, F. (2011). Boc and Gas1 each form distinct Shh receptor complexes with Ptch1 and are required for Shh-mediated cell proliferation. Dev. Cell 20, 788–801.

Jumper, J., Evans, R., Pritzel, A., Green, T., Figurnov, M., Ronneberger, O., Tunyasuvunakool, K., Bates, R., Žídek, A., Potapenko, A., et al. (2021). Highly accurate protein structure prediction with AlphaFold. Nature 596, 583–589.

Kavran, J.M., Ward, M.D., Oladosu, O.O., Mulepati, S., and Leahy, D.J. (2010). All mammalian hedgehog proteins interact with cell adhesion molecule, downregulated by oncogenes (CDO) and brother of CDO (BOC) in a conserved manner. J. Biol. Chem. 285, 24584–24590.

Kawakami, A., Nojima, Y., Toyoda, A., Takahoko, M., Satoh, M., Tanaka, H., Wada, H., Masai, I., Terasaki, H., Sakaki, Y., et al. (2005). The zebrafish-secreted matrix protein you/scube2 is implicated in long-range regulation of hedgehog signaling. Curr. Biol. 15, 480–488.

Kim, J., Hsia, E.Y., Brigui, A., Plessis, A., Beachy, P.A., and Zheng, X. (2015). The role of ciliary trafficking in Hedgehog receptor signaling. Sci. Signal. 8, ra55.

Krauss, S., Concordet, J.P., and Ingham, P.W. (1993). A functionally conserved homolog of the Drosophila segment polarity gene hh is expressed in tissues with polarizing activity in zebrafish embryos. Cell 75, 1431–1444.

Developmental Cell
Article

CellPress

Kuo, W.J., Digman, M.A., and Lander, A.D. (2010). Heparan sulfate acts as a bone morphogenetic protein coreceptor by facilitating ligand-induced receptor hetero-oligomerization. Mol. Biol. Cell 21, 4028–4041.

Lander, A.D. (1998). Proteoglycans: master regulators of molecular encounter? Matrix Biol. 17, 465–472.

Lee, C.S., Buttitta, L., and Fan, C.M. (2001). Evidence that the WNT-inducible growth arrest-specific gene 1 encodes an antagonist of sonic hedgehog signaling in the somite. Proc. Natl. Acad. Sci. U S A 98, 11347–11352.

Li, J., Shang, G., Chen, Y.J., Brautigam, C.A., Liou, J., Zhang, X., and Bai, X.C. (2019). Cryo-EM analyses reveal the common mechanism and diversification in the activation of RET by different ligands. eLife 8, e47650.

Li, W., Wang, L., Wierbowski, B.M., Lu, M., Dong, F., Liu, W., Li, S., Wang, P., Salic, A., and Gong, X. (2021). Structural insights into proteolytic activation of the human Dispatched1 transporter for Hedgehog morphogen release. Nat. Commun. 12, 6966.

López-Casillas, F., Wrana, J.L., and Massagué, J. (1993). Betaglycan presents ligand to the TGF beta signaling receptor. Cell 73, 1435–1444.

Los, G.V., Encell, L.P., McDougall, M.G., Hartzell, D.D., Karassina, N., Zimprich, C., Wood, M.G., Learish, R., Ohana, R.F., Urh, M., et al. (2008). HaloTag: A novel protein labeling technology for cell imaging and protein analysis. ACS Chem. Biol. 3, 373–382.

Luchetti, G., Sircar, R., Kong, J.H., Nachtergaele, S., Sagner, A., Byrne, E.F., Covey, D.F., Siebold, C., and Rohatgi, R. (2016). Cholesterol activates the G-protein coupled receptor smoothened to promote Hedgehog signaling. eLife 5, e20304.

Lum, L., and Beachy, P.A. (2004). The Hedgehog response network: sensors, switches, and routers. Science 304, 1755–1759.

Marigo, V., Davey, R.A., Zuo, Y., Cunningham, J.M., and Tabin, C.J. (1996). Biochemical evidence that patched is the Hedgehog receptor. Nature 384, 176–179.

Marigo, V., and Tabin, C.J. (1996). Regulation of patched by sonic hedgehog in the developing neural tube. Proc. Natl. Acad. Sci. U S A 93, 9346–9351.

Martinelli, D.C., and Fan, C.M. (2007). Gas1 extends the range of Hedgehog action by facilitating its signaling. Genes Dev. 21, 1231–1243.

Martinelli, D.C., and Fan, C.M. (2009). A sonic hedgehog missense mutation associated with holoprosencephaly causes defective binding to GAS1. J. Biol. Chem. 284, 19169–19172.

Mathew, E., Zhang, Y., Holtz, A.M., Kane, K.T., Song, J.Y., Allen, B.L., and Pasca di Magliano, M.P. (2014). Dosage-dependent regulation of pancreatic cancer growth and angiogenesis by Hedgehog signaling. Cell Rep. 9, 484–494.

Maun, H.R., Wen, X., Lingel, A., de Sauvage, F.J., Lazarus, R.A., Scales, S.J., and Hymowitz, S.G. (2010). Hedgehog pathway antagonist 5E1 binds hedgehog at the pseudo-active site. J. Biol. Chem. 285, 26570–26580.

McLellan, J.S., Zheng, X., Hauk, G., Ghirlando, R., Beachy, P.A., and Leahy, D.J. (2008). The mode of Hedgehog binding to Ihog homologues is not conserved across different phyla. Nature 455, 979–983.

Mostoslavsky, G., Fabian, A.J., Rooney, S., Alt, F.W., and Mulligan, R.C. (2006). Complete correction of murine Artemis immunodeficiency by lentiviral vector-mediated gene transfer. Proc. Natl. Acad. Sci. U S A 103, 16406–16411.

Motoyama, J., Takabatake, T., Takeshima, K., and Hui, C. (1998). Ptch2, a second mouse Patched gene is co-expressed with Sonic hedgehog. Nat. Genet. 18, 104–106.

Nedelcu, D., Liu, J., Xu, Y., Jao, C., and Salic, A. (2013). Oxysterol binding to the extracellular domain of smoothened in Hedgehog signaling. Nat. Chem. Biol. 9, 557–564.

Nikaido, H. (2018). RND transporters in the living world. Res. Microbiol. 169, 363–371.

Ohana, R.F., Encell, L.P., Zhao, K., Simpson, D., Slater, M.R., Urh, M., and Wood, K.V. (2009). HaloTag7: a genetically engineered tag that enhances bacterial expression of soluble proteins and improves protein purification. Protein Expr. Purif. 68, 110–120.

Okada, A., Charron, F., Morin, S., Shin, D.S., Wong, K., Fabre, P.J., Tessier-Lavigne, M., and McConnell, S.K. (2006). Boc is a receptor for sonic hedgehog in the guidance of commissural axons. Nature 444, 369–373.

Parkash, V., and Goldman, A. (2009). Comparison of GFL-GFRalpha complexes: further evidence relating GFL bend angle to RET signalling. Acta Crystallogr. Sect. F Struct. Biol. Cryst. Commun. 65, 551–558.

Parkash, V., Leppänen, V.M., Virtanen, H., Jurvansuu, J.M., Bespalov, M.M., Sidorova, Y.A., Runeberg-Roos, P., Saarma, M., and Goldman, A. (2008). The structure of the glial cell line-derived neurotrophic factor-coreceptor complex: insights into RET signaling and heparin binding. J. Biol. Chem. 283, 35164–35172.

Pepinsky, R.B., Rayhorn, P., Day, E.S., Dergay, A., Williams, K.P., Galdes, A., Taylor, F.R., Boriack-Sjodin, P.A., and Garber, E.A. (2000). Mapping Sonic hedgehog-receptor interactions by steric interference. J. Biol. Chem. 275, 10995–11001.

Pepinsky, R.B., Zeng, C., Wen, D., Rayhorn, P., Baker, D.P., Williams, K.P., Bixler, S.A., Ambrose, C.M., Garber, E.A., Miatkowski, K., et al. (1998). Identification of a palmitic acid-modified form of human Sonic hedgehog. J. Biol. Chem. 273, 14037–14045.

Petrov, K., de Almeida Magalhaes, T., and Salic, A. (2021). Mechanism and ultrasensitivity in Hedgehog signaling revealed by Patched1 disease mutations. Proc. Natl. Acad. Sci. U S A 118.

Petrov, K., Wierbowski, B.M., Liu, J., and Salic, A. (2020). Distinct cation gradients power cholesterol transport at different key points in the Hedgehog signaling pathway. Dev. Cell 55, 314–327.e7.

Pineda-Alvarez, D.E., Roessler, E., Hu, P., Srivastava, K., Solomon, B.D., Siple, C.E., Fan, C.M., and Muenke, M. (2012). Missense substitutions in the GAS1 protein present in holoprosencephaly patients reduce the affinity for its ligand. SHH. Hum. Genet. 131, 301–310.

Porter, J.A., Ekker, S.C., Park, W.J., Von Kessler, D.P., Young, K.E., Chen, C.H., Ma, Y., Woods, A.S., Cotter, R.J., Koonin, E.V., et al. (1996a). Hedgehog patterning activity: role of a lipophilic modification mediated by the carboxy-terminal autoprocessing domain. Cell 86, 21–34.

Porter, J.A., Young, K.E., and Beachy, P.A. (1996b). Cholesterol modification of hedgehog signaling proteins in animal development. Science 274, 255–259.

Punjani, A., Rubinstein, J.L., Fleet, D.J., and Brubaker, M.A. (2017). cryoSPARC: algorithms for rapid unsupervised cryo-EM structure determination. Nat. Methods 14, 290–296.

Qi, C., Di Minin, G., Vercellino, I., Wutz, A., and Korkhov, V.M. (2019). Structural basis of sterol recognition by human hedgehog receptor PTCH1. Sci. Adv. 5, eaaw6490.

Qi, X., Schmiege, P., Coutavas, E., and Li, X. (2018a). Two Patched molecules engage distinct sites on Hedgehog yielding a signaling-competent complex. Science 362, eaas8843.

Qi, X., Schmiege, P., Coutavas, E., Wang, J., and Li, X. (2018b). Structures of human Patched and its complex with native palmitoylated sonic hedgehog. Nature 560, 128–132.

Qian, H., Cao, P., Hu, M., Gao, S., Yan, N., and Gong, X. (2018). Inhibition of tetrameric Patched1 by Sonic Hedgehog through an asymmetric paradigm. Nat. Commun. 10, 2320.

Reeves, P.J., Callewaert, N., Contreras, R., and Khorana, H.G. (2002). Structure and function in rhodopsin: high-level expression of rhodopsin with restricted and homogeneous N-glycosylation by a tetracycline-inducible N-acetylglucosaminyltransferase I-negative HEK293S stable mammalian cell line. Proc. Natl. Acad. Sci. U S A 99, 13419–13424.

Ribeiro, L.A., Quiezi, R.G., Nascimento, A., Bertolacini, C.P., and Richieri-Costa, A. (2010). Holoprosencephaly and holoprosencephaly-like phenotype and GAS1 DNA sequence changes: report of four Brazilian patients. Am. J. Med. Genet. A 152A, 1688–1694.

Riddle, R.D., Johnson, R.L., Laufer, E., and Tabin, C. (1993). Sonic hedgehog mediates the polarizing activity of the ZPA. Cell 75, 1401–1416.

Ritchie, T.K., Grinkova, Y.V., Bayburt, T.H., Denisov, I.G., Zolnerciks, J.K., Atkins, W.M., and Sligar, S.G. (2009). Chapter 11 - Reconstitution of

membrane proteins in phospholipid bilayer nanodiscs. Methods Enzymol. *464*, 211–231.

Roessler, E., El-Jaick, K.B., Dubourg, C., Vélez, J.I., Solomon, B.D., Pineda-Alvarez, D.E., Lacbawan, F., Zhou, N., Ouspenskaia, M., Paulussen, A., et al. (2009). The mutational spectrum of holoprosencephaly-associated changes within the SHH gene in humans predicts loss-of-function Through either key structural alterations of the ligand or its altered synthesis. Hum. Mutat. *30*, E921–E935.

Rohou, A., and Grigorieff, N. (2015). CTFFIND4: fast and accurate defocus estimation from electron micrographs. J. Struct. Biol. *192*, 216–221.

Rubin, L.L., and de Sauvage, F.J. (2006). Targeting the Hedgehog pathway in cancer. Nat. Rev. Drug Discov. *5*, 1026–1033.

Rudolf, A.F., Kinnebrew, M., Kowatsch, C., Ansell, T.B., El Omari, K.E., Bishop, B., Pardon, E., Schwab, R.A., Malinauskas, T., Qian, M., et al. (2019). The morphogen Sonic hedgehog inhibits its receptor Patched by a pincer grasp mechanism. Nat. Chem. Biol. *15*, 975–982.

Sandmark, J., Dahl, G., Öster, L., Xu, B., Johansson, P., Akerud, T., Aagaard, A., Davidsson, P., Bigalke, J.M., Winzell, M.S., et al. (2018). Structure and biophysical characterization of the human full-length neurturin-GFRa2 complex: A role for heparan sulfate in signaling. J. Biol. Chem. *293*, 5492–5508.

Stone, D.M., Hynes, M., Armanini, M., Swanson, T.A., Gu, Q., Johnson, R.L., Scott, M.P., Pennica, D., Goddard, A., Phillips, H., et al. (1996). The tumour-suppressor gene patched encodes a candidate receptor for Sonic hedgehog. Nature *384*, 129–134.

Suloway, C., Pulokas, J., Fellmann, D., Cheng, A., Guerra, F., Quispe, J., Stagg, S., Potter, C.S., and Carragher, B. (2005). Automated molecular microscopy: the new Leginon system. J. Struct. Biol. *151*, 41–60.

Tenzen, T., Allen, B.L., Cole, F., Kang, J.S., Krauss, R.S., and McMahon, A.P. (2006). The cell surface membrane proteins Cdo and Boc are components and targets of the Hedgehog signaling pathway and feedback network in mice. Dev. Cell *10*, 647–656.

Trinh, M.N., Lu, F., Li, X., Das, A., Liang, Q., De Brabander, J.K., Brown, M.S., and Goldstein, J.L. (2017). Triazoles inhibit cholesterol export from lysosomes by binding to NPC1. Proc. Natl. Acad. Sci. U S A *114*, 89–94.

Tukachinsky, H., Kuzmickas, R.P., Jao, C.Y., Liu, J., and Salic, A. (2012). Dispatched and scube mediate the efficient secretion of the cholesterol-modified hedgehog ligand. Cell Rep. *2*, 308–320.

Tukachinsky, H., Lopez, L.V., and Salic, A. (2010). A mechanism for vertebrate Hedgehog signaling: recruitment to cilia and dissociation of SuFu-Gli protein complexes. J. Cell Biol. *191*, 415–428.

Tukachinsky, H., Petrov, K., Watanabe, M., and Salic, A. (2016). Mechanism of inhibition of the tumor suppressor Patched by Sonic Hedgehog. Proc. Natl. Acad. Sci. U S A *113*, E5866–E5875.

Tunyasuvunakool, K., Adler, J., Wu, Z., Green, T., Zielinski, M., Žídek, A., Bridgland, A., Cowie, A., Meyer, C., Laydon, A., et al. (2021). Highly accurate protein structure prediction for the human proteome. Nature *596*, 590–596.

van den Heuvel, M., and Ingham, P.W. (1996). smoothened encodes a receptor-like serpentine protein required for hedgehog signalling. Nature *382*, 547–551.

Velazquez-Campoy, A., Leavitt, S.A., and Freire, E. (2015). Characterization of protein-protein interactions by isothermal titration calorimetry. Methods Mol. Biol. Clifton NJ *1278*, 183–204.

Voss, N.R., and Gerstein, M. (2010). 3V: cavity, channel and cleft volume calculator and extractor. Nucleic Acids Res. *38*, W555–W562.

Wang, Q., Asarnow, D.E., Ding, K., Mann, R.K., Hatakeyama, J., Zhang, Y., Ma, Y., Cheng, Y., and Beachy, P.A. (2021). Dispatched uses Na(+) flux to power release of lipid-modified Hedgehog. Nature *599*, 320–324.

Wang, X., Baloh, R.H., Milbrandt, J., and Garcia, K.C. (2006). Structure of artemin complexed with its receptor GFRalpha3: convergent recognition of glial cell line-derived neurotrophic factors. Structure *14*, 1083–1092.

Waterhouse, A.M., Procter, J.B., Martin, D.M., Clamp, M., and Barton, G.J. (2009). Jalview Version 2–a multiple sequence alignment editor and analysis workbench. Bioinformatics Oxf. Engl. version *2 25*, 1189–1191.

Weiss, L.E., Milenkovic, L., Yoon, J., Stearns, T., and Moerner, W.E. (2019). Motional dynamics of single Patched1 molecules in cilia are controlled by Hedgehog and cholesterol. Proc. Natl. Acad. Sci. U S A *116*, 5550–5557.

Whalen, D.M., Malinauskas, T., Gilbert, R.J.C., and Siebold, C. (2013). Structural insights into proteoglycan-shaped Hedgehog signaling. Proc. Natl. Acad. Sci. U S A *110*, 16420–16425.

Wierbowski, B.M., Petrov, K., Aravena, L., Gu, G., Xu, Y., and Salic, A. (2020). Hedgehog pathway activation requires Coreceptor-catalyzed, lipid-dependent relay of the sonic hedgehog ligand. Dev. Cell *55*, 450–467.e8.

Williams, K.P., Rayhorn, P., Chi-Rosso, G., Garber, E.A., Strauch, K.L., Horan, G.S., Reilly, J.O., Baker, D.P., Taylor, F.R., Koteliansky, V., et al. (1999). Functional antagonists of sonic hedgehog reveal the importance of the N terminus for activity. J. Cell Sci. *112*, 4405–4414.

Woods, I.G., and Talbot, W.S. (2005). The you gene encodes an EGF-CUB protein essential for Hedgehog signaling in zebrafish. PLoS Biol. *3*, e66.

Yao, S., Lum, L., and Beachy, P. (2006). The Ihog cell-surface proteins bind hedgehog and mediate pathway activation. Cell *125*, 343–357.

Yue, S., Tang, L.Y., Tang, Y., Tang, Y., Shen, Q.H., Ding, J., Chen, Y., Zhang, Z., Yu, T.T., Zhang, Y.E., et al. (2014). Requirement of Smurf-mediated endocytosis of Patched1 in sonic hedgehog signal reception. eLife *3*, e02555.

Zhang, W., Kang, J.S., Cole, F., Yi, M.J., and Krauss, R.S. (2006). Cdo functions at multiple points in the sonic hedgehog pathway, and cdo-deficient mice accurately model human holoprosencephaly. Dev. Cell *10*, 657–665.

Zhang, Y., Bulkley, D.P., Xin, Y., Roberts, K.J., Asarnow, D.E., Sharma, A., Myers, B.R., Cho, W., Cheng, Y., and Beachy, P.A. (2018). Structural basis for cholesterol transport-like activity of the hedgehog receptor patched. Cell *175*, 1352–1364.e14.

Zhang, Y.X., Lu, W.J., Bulkley, D.P., Liang, J.H., Ralko, A., Han, S., Roberts, K.J., Li, A.P., Cho, W., Cheng, Y.F., et al. (2020). Hedgehog pathway activation through nanobody-mediated conformational blockade of the Patched sterol conduit. Proc. Natl. Acad. Sci. U S A *117*, 28838–28846.

Zheng, S.Q., Palovcak, E., Armache, J.P., Verba, K.A., Cheng, Y., and Agard, D.A. (2017). MotionCor2: anisotropic correction of beam-induced motion for improved cryo-electron microscopy. Nat. Methods *14*, 331–332.

Zivanov, J., Nakane, T., Forsberg, B.O., Kimanius, D., Hagen, W.J., Lindahl, E., and Scheres, S.H. (2018). New tools for automated high-resolution cryo-EM structure determination in RELION-3. eLife *7*, e42166.

Developmental Cell
Article

CellPress

STAR★METHODS

KEY RESOURCES TABLE

REAGENT or RESOURCE	SOURCE	IDENTIFIER
Antibodies		
chicken polyclonal anti-mARL13B	Petrov et al., 2020	N/A
rabbit polyclonal anti-mCherry	Nedelcu et al., 2013	N/A
goat polyclonal anti-mSMO	Nedelcu et al., 2013	N/A
mouse monoclonal anti-FLAG M1	A.C. Kruse; ATCC	Cat# HB-9259; RRID: CVCL_J730
mouse monoclonal anti-HPC	A.C. Kruse	N/A
rabbit monoclonal anti-SHH (clone C9C5)	Cell Signaling Technology	Cat# 2207S; RRID: AB_2188191
mouse monoclonal anti-SHH (clone 5E1)	DSHB; Ericson et al., 1996	Cat# 5e1; RRID: AB_528466
donkey anti-chicken IgY–Alexa Fluor® 647 conjugate	Jackson ImmunoResearch	Cat# 703-605-155; RRID: AB_2340379
donkey anti-rabbit IgG–Alexa Fluor® 555 conjugate	Thermo	Cat# A-31572; RRID: AB_162543
donkey anti-goat IgG–Alexa Fluor® 488 conjugate	Thermo	Cat# A-11055; RRID: AB_2534102
sheep anti-mouse IgG–HRP conjugate	Jackson ImmunoResearch	Cat# 515-005-003; RRID: AB_2340287
donkey anti-rabbit IgG–HRP conjugate	GE Healthcare	Cat# NA934; RRID: AB_772206
Bacterial and Virus Strains		
E. coli BL21 (DE3) pLysS	Sigma	Cat# 69451
Chemicals, Peptides, and Recombinant Proteins		
cholesterol ($\geq$ 99%)	Sigma	Cat# C8667
cholesteryl hemisuccinate (CHS)	Sigma	Cat# C6512
n-dodecyl-β-D-maltopyranoside (DDM)	Anatrace	Cat# D310
1-palmitoyl-2-oleoyl-glycero-3-phosphocholine (POPC)	Avanti	Cat# 850457C
Amphipol A8-35	Anatrace	Cat# A835
cOmplete™, mini, EDTA-free protease inhibitor cocktail tablets	Roche	Cat# 11836170001
cycloheximide	Sigma	Cat# 01810
SAG (SMO agonist)	Axxora; Chen et al., 2002	Cat# BV-1939
cholesterol [24,25-3H]	American Radiolabeled Chemicals	Cat# ART 1987
palmitic acid [9,10-3H(N)]	American Radiolabeled Chemicals	Cat# ART 0129
Ultima Gold™ liquid scintillation cocktail	Perkin-Elmer	Cat# 6013329
HaloTag® TMR ligand	Promega	Cat# G8251
HaloTag® amine (O4) ligand	Promega	Cat# P6741
FLAG elution peptide: NH₂-DYKDDDDK-OH	Genscript	N/A
HPC elution peptide: NH₂-EDQVDPRLIDGK-OH	Genscript	N/A
palmitoylated SHH EP: palm-SGPGRGFGKRRHPKKLTPLAYK-OH	Biomatik; Tukachinsky et al., 2016	N/A
unpalmitoylated SHH EP: NH₂-SGPGRGFGKRRHPKKLTPLAYK-OH	Biomatik; Tukachinsky et al., 2016	N/A
octanoylated SHH EP: oct-SGPGRGFGKRRHPKKLTPLAYK-OH	Biomatik; this paper	N/A
truncated, palmitoylated SHH EP (9aa): palm-SGPGRGFGK-OH	Biomatik; this paper	N/A
biotinylated, palmitoylated SHH EP: palm-CGPGRGFGKRRHPKKLTPLAYKK-biotin	Biomatik; Tukachinsky et al., 2016	N/A

Continued

REAGENT or RESOURCE	SOURCE	IDENTIFIER
biotinylated, unpalmitoylated SHH EP: NH_2-CGPGRGFGKRRHPKKLTPLAYKK-biotin	Biomatik; Tukachinsky et al., 2016	N/A
streptavidin–Alexa Fluor® 594 conjugate	Thermo	Cat# S11227
PreScission protease	GE Healthcare	Cat# 27084301
See Table S5 for a list of all purified proteins utilized in this study.	This paper	N/A
Critical Commercial Assays		
Bac-to-Bac™ Baculovirus Expression System	Thermo	Cat# 10359016
BioBeads™ SM-2	Bio-Rad	Cat# 1523920
CNBr-activated sepharose	GE Healthcare	Cat# 17-0430-01
Ni-NTA agarose	QIAGEN	Cat# 30230
chitin resin	New England Biolabs; Chong et al., 1997	Cat# S6651
HaloLink™ resin	Promega	Cat# G1914
illustra NAP™-5 columns	GE Healthcare	Cat# 17085301
Superdex® 200, 10/300 GL column	GE Healthcare	Cat# 17517501
Superose® 6 column	GE Healthcase	N/A
HiLoad® Superdex® 200 26/60 pg column	GE Healthcare	Cat# 28989336
Amicon® Ultra-0.5 centrifugal filter unit – 10kDa cutoff	Millipore	Cat# UFC5010
Amicon® Ultra-4 centrifugal filter unit – 10kDa cutoff	Millipore	Cat# UFC8010
QUANTIFOIL® R1.2/1.3, copper, 300 mesh, holey carbon-coated grids	Electron Microscopy Sciences	Cat# Q350CR1.3
3–12% NativePAGE™ Bis-Tris gels	Thermo	Cat# BN1001BOX
Nano-Glo® luciferase assay	Promega	Cat# N1120
Deposited data		
atomic coordinates, apo-PTCH1 nanodisc structure	Protein Data Bank; this paper	PDB: 7RHR
cryo-EM map, apo-PTCH1 nanodisc structure	Electron Microscopy Data Bank; this paper	EMDB: EMD-24467
atomic coordinates, GAS1–SHH–PTCH1 nanodisc ternary complex structure	Protein Data Bank; this paper	PDB: 7RHQ
cryo-EM map, GAS1–SHH–PTCH1 nanodisc ternary complex structure	Electron Microscopy Data Bank; this paper	EMDB: EMD-24466
Experimental Models: Cell Lines		
Human: HEK293T	ATCC	Cat# CRL-3216
Human: *MGAT1* $^{-/-}$ HEK293S	A.C. Kruse; ATCC; Reeves et al., 2002	Cat# CRL-3022
Insect: Sf9	ATCC	Cat# CRL-1711
Mouse: *Cdon* $^{-/-}$; *Boc* $^{-/-}$; *Gas1* $^{-/-}$ (coreceptor-null) MEF	B.L. Allen; Mathew et al., 2014	N/A
Mouse: *Gas1* $^{-/-}$ (GAS1-null) MEF	Wierbowski et al., 2020	N/A
Mouse: *Ptch1* $^{-/-}$ (PTCH1-null) MEF	M.P. Scott; Goodrich et al., 1997	N/A
See Table S4 for a complete list of cell lines utilized in this study.	This paper	N/A
Recombinant DNA		
See Table S3 for a list of all plasmids utilized in this study.	This paper	N/A
Software and Algorithms		
3V	Voss and Gerstein, 2010	https://3vee.molmovdb.org/
COOT	Emsley et al., 2010	https://www2.mrc-lmb.cam.ac.uk/personal/pemsley/coot/; RRID: SCR_014222

(Continued on next page)

Developmental Cell
Article

CellPress

Continued

REAGENT or RESOURCE	SOURCE	IDENTIFIER
cryoSPARC v2.15.0	Punjani et al. (2017)	https://cryosparc.com/; RRID: SCR_016501
CTFFIND4.1	Rohou and Grigorieff, 2015	https://grigorrieflab.umassmed.edu/ctffind4; RRID: SCR_016732
FIJI	National Institutes of Health	http://fiji.sc; RRID: SCR_002285
Gautomatch	K. Zhang	https://www2.mrc-lmb.cam.ac.uk/research/locally-developed-software/zhang-software/
Inkscape	Inkscape	https://inkscape.org/en/; RRID: SCR_014479
JalView	Waterhouse et al., 2009	http://www.jalview.org/; RRID: SCR_006459
Leginon	Suloway et al., 2005	http://emg.nysbc.org/redmine/projects/leginon/wiki/Leginon_Homepage; RRID: SCR_016731
MATLAB	MathWorks	http://www.mathworks.com/products/matlab/; RRID: SCR_001622
MetaMorph Microscopy Automation and Image Analysis Software	Molecular Devices	http://www.moleculardevices.com/Products/Software/Meta-Imaging-Series/MetaMorph.html; RRID: SCR_002368
MotionCor2	Zheng et al., 2017	N/A
Origin	OriginLab	http://www.originlab.com/index.aspx?go=PRODUCTS/Origin; RRID: SCR_014212
PHENIX	Adams et al., 2010	https://www.phenix-online.org/; RRID: SCR_014224
Photoshop CS5	Adobe	https://www.adobe.com/products/photoshop.html; RRID: SCR_014199
Prism 8	GraphPad	http://www.graphpad.com/; RRID: SCR_002798
PyMOL	Schrödinger	https://pymol.org/2/; RRID: SCR_000305
RELION 3.1.0	Zivanov et al., 2018	https://www3.mrc-lmb.cam.ac.uk/relion; RRID: SCR_016274
SALIGN	Braberg et al., 2012	https://salilab.org/salign
Other		
FEI Vitrobot™ Mark IV plunger	Thermo	N/A
K2 Summit® direct electron detection camera	Gatan	N/A
GIF Quantum® LS imaging energy filter	Gatan	N/A
Titan Krios™ G3 transmission electron microscope	Thermo	N/A
MicroCal™ iTC200 calorimeter	Malvern Panalytical	N/A
SpectraMax® M5 multi-mode microplate reader	Molecular Devices	N/A
Wallac VICTOR3™ microplate reader	Perkin-Elmer	N/A
Tri-Carb® 2910 TR liquid scintillation counter	Perkin-Elmer	N/A
10x PlanApo 0.45NA air objective lens	Nikon	N/A
40x PlanApo 0.95NA air objective lens	Nikon	N/A
ORCA®-Flash4.0 V3 digital CMOS camera	Hamamatsu	N/A
ECLIPSE Ti2-E microscope	Nikon	N/A

RESOURCE AVAILABILITY

Lead contact
Further information and requests for reagents should be directed to, and will be fulfilled by, the Lead Contact, Adrian Salic (adrian_salic@hms.harvard.edu).

Materials availability
New reagents generated in this study, such as expression constructs, may be requested directly from the Lead Contact.

Data and code availability
- Atomic coordinates and cryo-EM maps have been deposited in Protein Data Bank and Electron Microscopy Data Bank, respectively, and are publicly available as of the date of publication. PDB IDs, EMDB IDs, and their corresponding DOIs are listed in the key resources table.
- This paper does not report original code.
- Any additional information required to reanalyze the data reported in this paper is available from the Lead Contact upon request.

EXPERIMENTAL MODEL AND SUBJECT DETAILS

Cell culture
A complete list of cell lines utilized in this study is provided in Table S4. *MGAT1* $^{-/-}$ HEK293S cells (Reeves et al., 2002) were a gift from Andrew Kruse (Harvard Medical School). *Cdon* $^{-/-}$; *Boc* $^{-/-}$; *Gas1* $^{-/-}$ (coreceptor-null) MEFs (Mathew et al., 2014) were a gift from Ben Allen (University of Michigan). *Ptch1 -/-* (PTCH1-null) MEFs (Goodrich et al., 1997) were a gift from Matt Scott (Stanford). All cell lines were grown in DMEM (Corning) supplemented with 10% (v/v) fetal bovine serum (VWR) and penicillin/streptomycin (Corning) and maintained under standard growth conditions (37°C, 5% CO_2).

Generation of stable cell lines
Cell lines stably expressing transgenes for protein expression or rescue were generated by lentiviral transduction using virus produced with the third-generation lentiviral vector pHAGE (Mostoslavsky et al., 2006), containing the indicated promoters and resistance markers. HEK293T cells were transiently transfected to produce lentiviral particle–conditioned medium, which was mixed with polybrene (1 μg/mL, Sigma) to facilitate infection of target cells. After 48 h, transduced cells were isolated by selection with the appropriate antibiotic.

METHOD DETAILS

Antibodies
Mouse monoclonal anti-FLAG-M1 and mouse monoclonal anti–human protein C (HPC) antibodies were a generous gift from Andrew Kruse (Harvard Medical School). Mouse monoclonal anti-SHH antibody (clone 5E1) (Ericson et al., 1996) was obtained from the Developmental Studies Hybridoma Bank (University of Iowa). Primary antibodies for immunoblotting were used at 1–2 μg/mL, in TBST [10 mM Tris-HCl, pH 7.6; 150 mM NaCl; 0.2% (v/v) Triton X-100] with 5% (w/v) non-fat dry milk. In experiments using calcium-dependent anti-FLAG-M1 and anti-HPC antibodies, all buffers were supplemented with 2 mM $CaCl_2$. Secondary antibodies used for immunoblotting (0.2 μg/mL final concentration) were: sheep anti-mouse IgG–HRP conjugate (Jackson ImmunoResearch) and donkey anti-rabbit IgG–HRP conjugate (GE Healthcare). Primary and secondary antibodies for immunofluorescence were used at 1 μg/mL, in TBST with 5% (w/v) bovine serum albumin (BSA). Immunofluorescence secondary antibodies were: donkey anti-chicken IgY–Alexa Fluor 647 conjugate (Jackson ImmunoResearch), donkey anti-rabbit IgG–Alexa Fluor 555 conjugate (Thermo), and donkey anti-goat IgG–Alexa Fluor 488 conjugate (Thermo).

DNA constructs
A list of the plasmids utilized in this study is provided in Table S3. Sequences of mouse SCUBE2, internally tagged human SHH variants, and gene blocks for single-chain variable fragment 5E1 (scFv5E1) and human GAS1 were reported previously (Petrov et al., 2020; Wierbowski et al., 2020). The *Xenopus laevis* PTCH1 construct for baculoviral expression consisted of amino acids 1–1178, followed by eight histidine residues and one copy of the HPC epitope. Sequences encoding monomeric and dimerized anti-PTCH1 nanobody (Zhang et al., 2020), C-terminally tagged with a hexahistidine tag, were subcloned into the pMAL-p2X vector (New England Biolabs). For the dimerized variant, the linker (GGGSGGGT)$_3$ was introduced between the two copies of the nanobody.

Protein expression and purification
A list of the proteins utilized in this study, with information about tags, purification, and in-text use, can be found in Table S5. Select procedures are described briefly below.
Xenopus laevis *PTCH1 purification and reconstitution*
Baculovirus encoding *Xenopus laevis* PTCH1 with the C-terminal intracellular domain deleted (residues 1–1178) and followed by an eight-residue histidine tag and the HPC epitope, was generated with the Bac-to-Bac system (Thermo Fisher). The baculovirus was used to infect Sf9 cells at a density of 3×10^6/mL. The cells were harvested 48 h after infection, and were stored frozen at –80°C until use. Cell pellets were thawed and lysed in hypotonic buffer (20 mM HEPES, pH 7.5) supplemented with EDTA-free protease inhibitor cocktail (Roche). Cell membranes were then solubilized in solubilization buffer [20 mM HEPES, pH 7.5; 150 mM NaCl; 1% (w/v)

Developmental Cell
Article

CellPress

n-dodecyl-β-D-maltopyranoside (DDM, Anatrace); and 0.1% (w/v) cholesteryl hemisuccinate (CHS, Sigma)]. The clarified supernatant was supplemented with 2 mM $CaCl_2$ and was loaded on an anti-HPC antibody affinity column. The column was extensively washed in solubilization buffer with 2 mM $CaCl_2$ and gradually reduced detergent concentration, and was eluted with elution buffer [20 mM HEPES, pH 7.5; 150 mM NaCl; 5 mM EDTA; 100 μg/mL HPC peptide; 0.03% (w/v) DDM; and 0.003% (w/v) CHS]. The eluted protein was concentrated and purified by size-exclusion chromatography on a Superdex 200 10/300 GL column (GE Healthcare), in 20 mM HEPES, pH 7.5; 150 mM NaCl; 0.03% (w/v) DDM; and 0.003% (w/v) CHS. Membrane scaffold protein MSP1D1 was expressed and purified from *E. coli* as previously described (Ritchie et al., 2009).

Nanodisc reconstitution of apo-PTCH1 was performed following a reported protocol for NPC1, with modifications (Trinh et al., 2017). In brief, concentrated PTCH1 was mixed with MSP1D1 and a cholate-solubilized lipid stock consisting of 90% (w/w) POPC (1-palmitoyl-2-oleoyl-glycero-3-phosphocholine, Avanti) and 10% (w/w) cholesterol (Sigma) at a ratio of 1:10:1000. After incubation at 4°C for 1 h, 0.8 g/mL of BioBeads SM-2 (Bio-Rad) were added and the mixture was rotated overnight at 4°C, to remove detergent and to allow nanodisc assembly. BioBeads were then removed and 3 mM $CaCl_2$ was added to the sample. To remove empty nanodiscs, PTCH1 was recaptured on anti-HPC resin and was washed extensively with binding buffer (20 mM HEPES, pH 7.5; 150 mM NaCl; 2 mM $CaCl_2$). The PTCH1 nanodiscs were eluted in elution buffer without detergent, and were further purified on a Superdex 200 10/300 GL column in binding buffer.

For amphipol reconstitution, concentrated PTCH1 was mixed with Amphipol A8-35 (Anatrace) at a mass ratio of 1:3. After incubation at 4°C for 4 h, the mixture was incubated with ~40 mg/mL BioBeads SM-2 overnight at 4°C. Following BioBead removal, the sample was concentrated and purified by size-exclusion chromatography on a Superose 6 column (GE Healthcare) in 20 mM HEPES, pH 7.5; 150 mM NaCl. The PTCH1 amphipols were concentrated to ~1 mg/mL and stored in 20 mM HEPES, pH 7.5; 150 mM NaCl; 15% (v/v) glycerol at -80°C.

Ternary GAS1–SHH–PTCH1 complex assembly
Stoichiometric 1:1 GAS1–SHH complex was isolated by dual affinity purification from conditioned medium produced by stably transduced *MGAT1* $^{-/-}$ HEK293S cells. Briefly, FLAG- and HaloTag7 (HT7)–tagged (Los et al., 2008; Ohana et al., 2009) GAS1-Ecto was coexpressed with internally HPC-tagged SHH [SHH(HPC7)] (Wierbowski et al., 2020). Two liters of conditioned medium (DMEM, supplemented with 1% FBS) were supplemented with $CaCl_2$ (2 mM) and were passed over anti-FLAG resin. After washing with TBS with 2 mM $CaCl_2$, bound protein was eluted with elution buffer (20 mM HEPES, pH 7.5; 200 mM NaCl; 5 mM EDTA; 100 μg/mL FLAG peptide). Eluted protein was buffer-exchanged to remove EDTA, and treated overnight at 4°C with PreScission protease (GE Healthcare), to remove the N-terminal FLAG-HT7 tag on GAS1-Ecto. Cleaved protein was supplemented with $CaCl_2$ to 2 mM, and passed over anti-HPC resin, to separate free tag and unliganded GAS1 from GAS1–SHH(HPC7). Washes and elution were performed as above, except using elution buffer with HPC peptide. Eluted protein was concentrated using a 10-kDa cutoff centrifugal filter unit (Millipore) and then loaded on Superdex 200 10/300, to isolate monomeric complex.

The cryo-EM sample for GAS1–SHH–PTCH1 complex was prepared by incubating nanodisc-embedded *Xenopus* PTCH1 (1.1 μM) with GAS1–SHH(HPC7) (3.3 μM) in 3 mL binding buffer (20 mM HEPES, pH 7.5; 150 mM NaCl; 2 mM $CaCl_2$), for 3 hours at room temperature. Excess GAS1–SHH(HPC7) was then removed by purification on Superdex 200 10/300 GL, in binding buffer. Fractions containing the GAS1–SHH–PTCH1 complex were pooled and were concentrated using a 100-kDa cutoff centrifugal filter (Millipore Sigma), followed by grid freezing and cryo-EM analysis.

Mammalian expression and purification of other secreted proteins
Secreted proteins—including SHH-N, GFRα1-Ecto, GAS1-Ecto, SCUBE2, and variants and complexes thereof—were stably expressed as FLAG-HT7- or HPC-HT7-tagged fusions in *MGAT1* $^{-/-}$ HEK293S cells, or were transiently expressed in HEK293T cells, as previously described (Wierbowski et al., 2020). Complexes of GAS1-Ecto with SHH singly modified with palmitate or cholesterol were prepared by co-expressing FLAG-HT7-GAS1-Ecto with SHH-N or with SHH(C24A), respectively. Purification from conditioned media was carried out essentially as above for the GAS1–SHH(HPC7) complex, except that a single round of affinity purification was used. Where indicated, proteins were further purified by size-exclusion chromatography on Superdex 200 10/300 GL, to isolate fractions containing monomeric species. The fractions were concentrated to above 1 mg/mL, flash frozen, and stored at -80 °C. For purification of SHH complexes, EDTA was omitted from elution buffer, to avoid disrupting calcium-dependent interactions (McLellan et al., 2008; Beachy et al., 2010). SHH-containing complexes were normalized by SHH concentration, as determined by immunoblotting alongside a standard curve of recombinant unlipidated SHH-N.

Bacterial expression and purification of proteins
Recombinant GAS1 tail was expressed as a 6xHis- (pET, Millipore) and HT7-tagged fusion protein in BL21 *E. coli*. To generate unlipidated SHH-N containing the native N-terminus, SHH-N was expressed as an N-terminal intein fusion (IMPACT–TWIN system, NEB) in BL21 *E. coli*. Expression, purification and intein cleavage were performed according to manufacturers' instructions. Recombinant SHH-N thus obtained was further purified by size-exclusion chromatography on a Superdex 200 26/60 column. The monomeric and dimerized anti-PTCH1 nanobody fusions were expressed in BL21 *E. coli* and were purified from the periplasm, first on Ni-NTA beads and then on amylose beads, according to the manufacturers' instructions. The purified protein was dialyzed against storage buffer (20 mM HEPES, pH 7.5; 150 mM NaCl), concentrated, flash frozen and stored at -80 °C until use.

Cryo-EM sample preparation and data collection
Apo-PTCH1 nanodisc and GAS1–SHH–PTCH1 complex nanodisc samples were concentrated to ~1 mg/mL. A sample of 3 μL was loaded onto a glow-discharged holey carbon grid (Quantifoil R1.2/1.3, copper, 300 mesh). All the grids were blotted for 4 s at 16 °C

and 100% relative humidity using an FEI Vitrobot Mark IV plunger before being plunge-frozen in liquid nitrogen–cooled liquid ethane. Cryo-EM data were collected using a Titan Krios G3 electron microscope (Thermo Fisher Scientific) operated at 300kV. Micrographs were acquired at the nominal magnification of 130,000x (calibrated pixel size of 1.06 Å on the sample level) using a K2 Summit camera (Gatan) equipped with a Quantum LS imaging energy filter (Gatan) with the slit width set at 20 eV. The dose rate on the camera was set to 8 e–/pixel/s. The total exposure time for each micrograph was 10 s fractionated into 50 frames with 0.2-s exposure time for each frame. The data collection was automated using the Leginon software package (Suloway et al., 2005). A total of 26,139 micrographs from 3 data collection sessions were collected for the apo-PTCH1 sample, and a total of 5,571 micrographs were collected from 2 data collection sessions for the GAS1–SHH–PTCH1 complex sample.

Cryo-EM image processing

The data processing procedures are shown in Figure S3 for GAS1–SHH–PTCH1 and Figure S4 for apo-PTCH1. Both datasets were processed in RELION 3.1.0 (Zivanov et al., 2018) and cryoSPARC v2.15.0 (Punjani et al., 2017) following the standard procedures. The beam-induced image drift was corrected using MotionCor2 (Zheng et al., 2017). The averaged images without dose weighting were used for defocus determination using CTFFIND4.1 (Rohou and Grigorieff, 2015) and images with dose weighting were used for particle picking and extraction. Particles were automatically picked by Gautomatch (https://www2.mrc-lmb.cam.ac.uk/research/locally-developed-software/zhang-software/).

A total of 3,793,918 particles were picked for the GAS1–SHH–PTCH1 complex. Bad particles were removed by 2D classification using particles with 2x binning. 861,929 particles were selected and submitted for single class 3D classification. Particles were then re-extracted without binning, re-centered and deduplicated. One more batch of 2D classification and two more batches of 3D classification using finer angular sampling rate (3.7° for first 30 iterations and 1.8° for another 20 iterations) for the second time were applied to the particles. The best 75,517 particles were selected for consensus refinement and resulted in a 4.2 Å map, followed by Bayesian polishing and 3D classification without alignment. Then 54,175 particles were selected for final refinement. After CTF refinement and a second round of Bayesian polishing using the first 30 frames, a 3.53 Å map was generated for model building.

A similar procedure was applied to the apo-PTCH1 dataset (Figure S4) to generate a 3D reconstruction at 3.0 Å resolution for model building.

Model building, refinement, and analysis

The human PTCH1 model from the revised cryo-EM structure of the human 1:2 SHH–PTCH1 complex (PDB ID: 6RVD) was used as an initial template to solve the apo-PTCH1 structure in nanodisc. The residues were mutated to match the sequence of *Xenopus* PTCH1, and the model was then iteratively adjusted manually in COOT (Emsley et al., 2010) and refined with phenix.real_space_refine in PHENIX (Adams et al., 2010). The resulting *Xenopus* PTCH1 structure, together with the high-resolution crystal structures of mouse SHH (PDB ID: 1VHH) and the D2 domain of hGFRα2 (PDB ID: 5MR4), were used to search for components in the GAS1–SHH–PTCH1 complex. The structure of GAS1 was initially modeled by docking two copies of the D2 domain of human GFRα2 into the density map, which identified the position of the G1 and G2 domains. The G1 domain structure was built by manually replacing its amino acid sequence. The G2 domain model was built manually, using the GAS1-G2 structure predicted by AlphaFold (Jumper et al., 2021; Tunyasuvunakool et al., 2021) as an initial template. The full model was rebuilt in COOT (Emsley et al., 2010) and refined using PHENIX (Adams et al., 2010). The volumes of ligand-binding cavities in GAS1 were calculated using the 3V program (Voss and Gerstein, 2010). Structural alignment between GAS1 and GFRα receptors were performed by SALIGN (Braberg et al., 2012). All structure figures were prepared in PyMOL. Data collection and refinement statistics are summarized in Table S1.

Immunoblotting

Mini-PROTEAN TGX 4–20% precast gels (Bio-Rad) were used for SDS-PAGE. Gels were equilibrated in transfer buffer [48 mM Tris, pH 9.2; 39 mM glycine; 1.3 mM SDS; 20% (v/v) methanol] for 30 min at room temperature prior to semi-dry transfer (Trans-Blot SD, Bio-Rad) to PVDF membranes (Bio-Rad). Membranes were incubated in blocking buffer [TBST with 5% (w/v) non-fat dry milk] at room temperature and then with primary antibody, in blocking buffer, overnight at 4°C. Following TBST washes, membranes were blocked again and then incubated in secondary antibody, in blocking buffer, for 1 h at room temperature. After washing, antibody signal was detected by chemiluminescence. For native PAGE, 3–12% NativePAGE Bis-Tris gels (Thermo) were used. Transfer was performed as above, except that membranes were subsequently fixed for 25 min in 8% (v/v) acetic acid. Air-dried membranes were rinsed with methanol to remove excess Coomassie dye and then immunoblotted as above.

Immunofluorescence microscopy of ciliary SMO and PTCH1

Immunofluorescence microscopy was used to measure ciliary localization of SMO (endogenous or mCherry-tagged), as readout for Hh pathway activation. Where indicated, mCherry- or eGFP-tagged PTCH1 was imaged in parallel, to measure SHH-dependent PTCH1 exit from cilia. Immunofluorescence imaging of Hh pathway components at primary cilia was performed as described (Wierbowski et al., 2020). Briefly, MEFs or NIH 3T3 cells were plated on gelatin-coated coverslips in 24-well plates, at a density of 1x10^5 cells/well. The cells were serum-starved overnight to induce ciliation, and then overnight treatments were applied in serum-free DMEM. Cells were fixed with 3.7% (w/v) formaldehyde in PBS for 30 min at room temperature, and ARL13B (ciliary marker) and Hh pathway components (SMO or PTCH1) were detected by immunofluorescence. Coverslips mounted in PBS with 50% (v/v) glycerol were imaged on an ECLIPSE Ti2-E microscope (Nikon) equipped with an ORCA-Flash4.0 camera (Hamamatsu) and a

Developmental Cell
Article

 CellPress

40x PlanApo 0.95NA air objective (Nikon). MetaMorph image acquisition software was used to acquire 5-slice z-stacks (at 1-μm intervals) for 30 fields of view per condition. A script written in FIJI (NIH) was used to generate maximum intensity projections (Wierbowski et al., 2020), and custom analysis software written in MATLAB (Nedelcu et al., 2013) was used to segment cilia by local adaptive thresholding of ARL13B images, and quantify associated background-subtracted SMO and PTCH1 intensities. Bars and points report median intensity (average of three subsets per condition), and error bars represent SEM. Unless otherwise noted, points are fit with a three-parameter curve in Prism.

Site-specific labeling of HT7 fusion proteins
Purified proteins containing the HT7 tag were fluorescently labeled for cell-based binding assays as described (Tukachinsky et al., 2016). Briefly, proteins were mixed with five-fold molar excess of HaloTag tetramethylrhodamine (TMR) ligand (Promega). After 1-h incubation at room temperature, a NAP-5 desalting column (GE Healthcare) was used to separate labeled protein from unincorporated dye.

Preparation of fluorescent streptavidin peptide ligands
To assay the interaction between the N-terminal palmitoylated effector peptide (EP) of SHH and receptors, we used a synthetic peptide (Biomatik) comprising residues 24–45 of human SHH, modified N-terminally with palmitate and C-terminally with biotin (Tukachinsky et al., 2016). Peptide was mixed with streptavidin–Alexa Fluor 594 (Thermo) at a 1:1 ratio. After 1 h at room temperature, unoccupied biotin-binding sites were blocked with excess free biotin.

Cell-based ligand-binding assays
Cell-based ligand–receptor binding assays were performed as described (Wierbowski et al., 2020). Briefly, HEK293T cells plated in poly-D-lysine–coated wells were transfected with eGFP-tagged receptor constructs. Two days later, cells were incubated with purified fluorescently labeled ligands for 1.5 h at 37°C, washed, and fixed in 3.7% (w/v) formaldehyde in PBS. Fixed cells were washed and imaged on an ECLIPSE Ti2-E epifluorescence microscope (Nikon) equipped with a 10x PlanApo 0.45NA air objective (Nikon). Four fields of view were acquired for each well, for the receptor and ligand channels, using MetaMorph software (Molecular Devices). Custom software written in MATLAB was used to segment eGFP-positive cells and calculate background-subtracted ligand intensity for each cell object. Distributions of ligand to area ratios for the cell objects for each condition are represented as box plots that span from the first to third intensity quartiles, with a line indicating the median. In dose-response experiments, each point represents median ligand:area ratio (average of four fields), and the data are fit with a three-parameter curve in Prism.

Blue native PAGE SHH transfer assays
SHH transfer assays were performed essentially as described (Wierbowski et al., 2020). Purified SCUBE2–SHH or GAS1-Ecto–SHH complexes were mixed with the indicated purified proteins (GAS1 species or PTCH1 in nanodisc or amphipol), in 20 mM HEPES, pH 8; 200 mM NaCl; 2 mM $CaCl_2$. The mixtures were incubated at 28°C, moved to ice, and subjected immediately to native PAGE, followed by immunoblotting. For native PAGE experiments, SHH migration is compared to that of various purified proteins, which serve as markers; their position is indicated to the right of each gel. For endpoint experiments, where not indicated, reactions were carried out for 2 h. For time course experiments, reactions were initiated at staggered time intervals, for simultaneous loading on gel. For competition experiments, SHH donor complexes were mixed with competitor for 30 min either prior to ("pre") or following ("post") a 2-h incubation with acceptor.

Radioactive lipid transfer assays
Radioligand transfer assays were performed as described (Wierbowski et al., 2020). GAS1–lipid beads were generated by incubating purified HT7-tagged GAS1-Ecto with either [^{3}H]-cholesterol (100 μCi/mL) or [^{3}H]-palmitic acid (100 μCi/mL) in TBST at room temperature for 1 h, followed by capture on HaloLink beads (Promega). Beads were washed four times with wash buffer (20 mM HEPES, pH 7.5; 150 mM NaCl) and were mixed with purified GAS1 constructs (2 μM) and tumbled at room temperature. Samples of the supernatant were collected at the indicated timepoints, and radioactivity released from the beads was measured by scintillation counting using Ultima Gold cocktail (Perkin-Elmer) and a Tri-Carb 2910 TR scintillation counter (Perkin-Elmer). When acceptor proteins were HT7-tagged, they were first reacted with excess HaloTag amine (O4) ligand (Promega), to block their capture on HaloLink beads. Radioactive cholesterol transfer data were fit with a one-phase association curve in Prism.

Bead-based SHH transfer assays
Luciferase-based measurements of SHH transfer from SCUBE2 to GAS1 were performed as described (Wierbowski et al., 2020). Briefly, purified SCUBE2–SHH containing NanoLuc luciferase–tagged SHH [SHH(NL7)], was captured on HaloLink resin. The beads were tumbled at room temperature with purified GAS1 acceptor proteins, and aliquots of the supernatant were collected at the indicated timepoints. Luminescence released into the supernatant was measured using Nano-Glo luciferase assay substrate (Promega), according to the manufacturer's instructions, and a VICTOR3 microplate reader (Perkin-Elmer). Luminescence transfer data were fit with a linear regression in Prism. Transfer of differentially lipidated SHH species from GAS1-Ecto to different GAS1 constructs was measured by immobilizing GAS1-Ecto–SHH complexes on HaloLink resin, and incubating the beads with acceptors as above, for 2 h.

Supernatant containing released SHH was separated from the beads, which were washed and then mixed with SDS-PAGE sample buffer, to elute SHH remaining bound to GAS1-Ecto donor. Equal fractions of material from the supernatant and the beads were separated on SDS-PAGE, followed by immunoblotting for SHH.

Luciferase-based SHH release assays

Luciferase-based measurements of SHH release from wild-type or DISP1-null cells were performed as described (Petrov et al., 2020). Briefly, HEK293T cells stably expressing SHH tagged with NanoLuc luciferase at an internal site were washed into serum-free medium, pre-incubated for 30 min with cycloheximide (100 μg/mL) (Sigma), and then treated with purified proteins in the continued presence of cycloheximide. Culture medium was collected at the indicated times, was clarified by centrifugation, and NanoLuc luciferase activity was measured using the Nano-Glo Luciferase Assay Substrate (Promega) in accordance with the manufacturer's instructions.

GAS1 tail immunoprecipitations

To assay interaction between GAS1 tail and unlipidated SHH-N, purified 6xHis-HT7-tagged GAS1-Tail or 6xHis-HT7 alone was immobilized on HaloLink beads. Recombinant SHH-N was added to the beads in binding buffer [20 mM HEPES, pH 7.5; 150 mM NaCl; and 2 mM CaCl$_2$], with or without a 30-min preincubation with the anti-SHH monoclonal antibody 5E1. After washing, bound SHH was eluted by boiling in sample buffer with DTT, and samples were analyzed by SDS-PAGE.

Isothermal titration calorimetry

Interaction between GAS1 and variants of the SHH EP was measured by isothermal titration calorimetry (ITC) using a MicroCal iTC200 calorimeter (Malvern Panalytical). Briefly, purified GAS1-Ecto at 50 μM in TBS was titrated by injection of 2 μL aliquots of 500 μM EP at constant temperature (25$°$C), with continuous stirring (750 rpm), giving rise to negative power peaks. The heat released in each injection was calculated from the raw data by integration of the peaks, after baseline subtraction. Binding isotherms were adjusted to a model in which the protein binds to N peptide molecules (Velazquez-Campoy et al., 2015). The integrated heat data were fit with a one-site binding model using Origin software (OriginLab) to calculate ΔH, K$_d$, and number of thermodynamically equivalent binding sites (N), reported in Table S2; ΔG and ΔS were calculated from these values using standard thermodynamic equations.

Tryptophan fluorescence spectroscopy

Trp fluorescence spectra were recorded for GAS1-Ecto, with or without palmitoylated or unpalmitoylated EP, at a GAS1:EP ratio of 1:3, as previously described (de Antonio et al., 2000; García-Linares et al., 2016). Fluorescence emission spectra were recorded on a SpectraMax M5 Multi-Mode Microplate Reader at 25$°$C, using a slit width of 4 nm for both excitation and emission. The spectra were recorded for excitation at 295 nm, where Tyr absorption is negligible. Thermostatically controlled cells with a path length of 0.2 and 1.0 cm for the excitation and emission beams, respectively, were used.

Gel and blot image processing

Images of blots and gels were cropped in Photoshop CS5, with white space left if lanes were omitted. Some grayscale Coomassie-stained gel images were pseudocolored in FIJI with a custom LUT that interpolates between #1919c6 (0) and #fefefe (255), to help differentiate them from immunoblots. Original images are available upon request.

QUANTIFICATION AND STATISTICAL ANALYSIS

Statistical parameters for imaging experiments involving quantitative comparisons are reported in figure legends and in the Method Details. All imaging-based assays report on fluorescence intensity values for at least 50 cells or cilia per condition. Results are typically shown as bars or points representing the population median (average of three or four subsets), with error bars representing SEM. Unless otherwise noted, dose-dependent responses are represented using population median values fit with a three-parameter response curve in Prism (GraphPad). To facilitate comparisons, measures of binding or ciliary localization have been normalized to a positive control, as described in figure legends. Qualitative experiments were performed at least twice on separate days, using independent batches of the proteins whenever possible.

Supplemental information

Structural basis for catalyzed assembly

of the Sonic hedgehog–Patched1 signaling complex

Pengxiang Huang, Bradley M. Wierbowski, Tengfei Lian, Charlene Chan, Sara García-Linares, Jiansen Jiang, and Adrian Salic
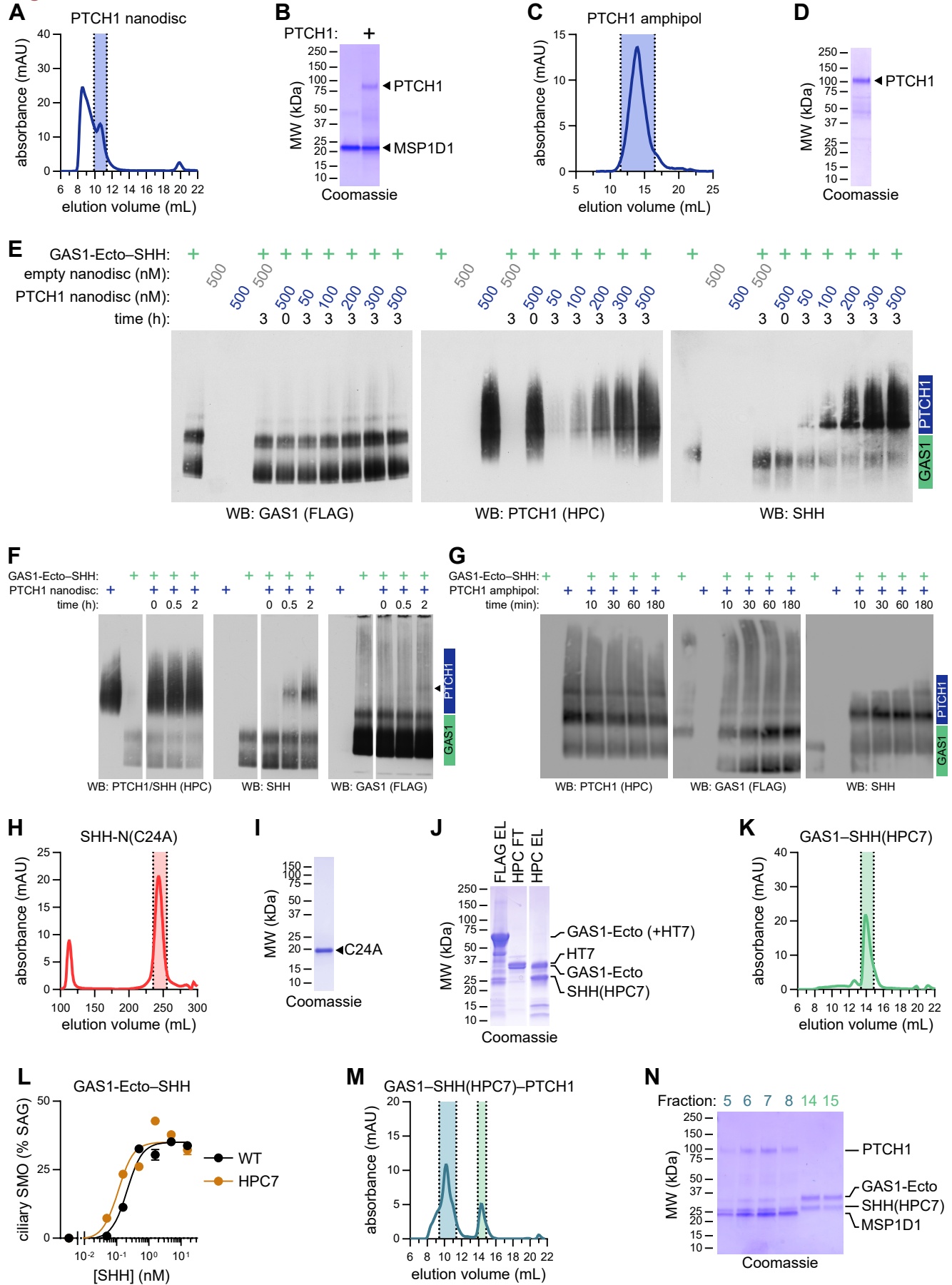
Figure S1

Figure S1. Generation of apo-PTCH1 and GAS1–SHH–PTCH1 ternary complex reconstituted in nanodiscs, Related to Figures 1 and 2

(A) Size-exclusion chromatogram (Superdex 200 10/300) of purified PTCH1, after reconstitution into MSP1D1 lipid nanodiscs. The indicated fractions (shaded) were pooled, concentrated and used for cryo-EM and SHH transfer assays.

(B) PTCH1 nanodiscs from (A) were analyzed alongside empty MSP1D1 nanodiscs, by SDS-PAGE and Coomassie staining.

(C) Size-exclusion chromatogram (Superose 6) of purified PTCH1 after reconstitution into amphipol. The indicated fractions (shaded) were pooled, concentrated and used for SHH transfer assays.

(D) PTCH1 reconstituted in amphipol from (C) was analyzed by SDS-PAGE and Coomassie staining.

(E) Purified GAS1-Ecto–SHH complex (200 nM) was incubated with increasing concentrations of PTCH1 nanodiscs, followed by separation by native PAGE and immunoblotting. A proportionally larger fraction of SHH transfers from GAS1 to PTCH1 at higher doses of PTCH1 nanodiscs.

(F) As in (E), but with tandem purified GAS1-Ecto–SHH(HPC7) complex. A small amount of GAS1 is retained with SHH on PTCH1 (arrowhead).

(G) As in (E), but with PTCH1 reconstituted in amphipols.

(H) Size-exclusion chromatogram (Superdex 200 26/60) of purified unlipidated SHH-N(C24A). The indicated monomeric fractions (shaded) were pooled and concentrated.

(I) Monomeric SHH-N(C24A) from (H) was analyzed by SDS-PAGE and Coomassie staining.

(J) GAS1-Ecto, tagged with FLAG and HaloTag, was co-expressed with SHH internally tagged with an HPC epitope (HPC7) (Wierbowski et al., 2020), and sub-stoichiometric GAS1-Ecto–SHH(HPC7) complex was isolated by affinity purification on FLAG resin (lane 1). Following PreScission protease treatment for GAS1 tag removal, HPC affinity was employed to separate the cleaved tag and unliganded GAS1 (lane 2) from the 1:1 GAS1-Ecto–SHH(HPC7) complex (lane 3).

(K) Size-exclusion chromatogram (Superdex 200 10/300) of the 1:1 GAS1-Ecto–SHH(HPC7) complex from (J).

(L) Dose-response of purified GAS1-Ecto–SHH and GAS1-Ecto–SHH(HPC7) complexes, measured on wild-type MEFs. Hh pathway activation was measured by recruitment of endogenous SMO to cilia. Data are normalized between Hh pathway activation for untreated cells and cells treated with saturating SAG (100%). Points represent average ciliary SMO for three replicates, and error bars represent SEM. At least 600 cilia were measured per replicate. Data are fit with a four-parameter curve. The HPC7 tag does not affect SHH potency.

(M) PTCH1 nanodiscs from (A) were incubated with an excess of GAS1-Ecto–SHH(HPC7) complex from (K) for 3 h at room temperature and were separated by size-exclusion chromatography (Superdex 200 10/300). Fractions corresponding to the ternary GAS1-Ecto–SHH(HPC7)–PTCH1 complex (shaded teal) and excess GAS1-Ecto–SHH(HPC7) complex (shaded green) were isolated.

(N) Fractions from the shaded regions in (M) were analyzed by SDS-PAGE and Coomassie staining. Fractions 6 and 7 were pooled and concentrated for cryo-EM.
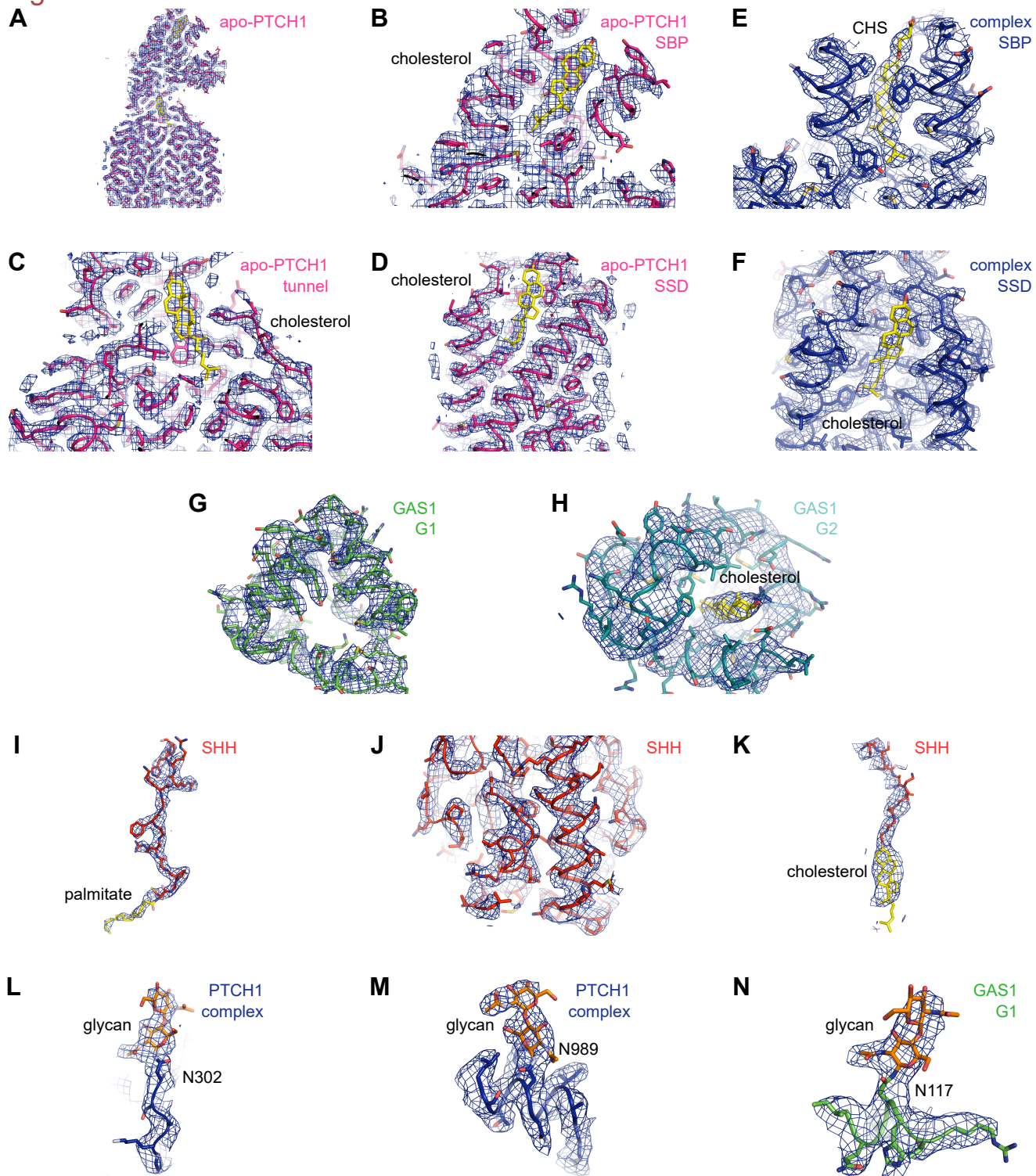
Figure S2

Figure S2. Cryo-EM maps for representative features in apo-PTCH1 and GAS1–SHH–PTCH1 complex, Related to Figure 2

(A) Overall density for apo-PTCH1, showing two cholesterol molecules, one in the ECD1 sterol-binding pocket (SBP) (Gong et al., 2018; Qi et al., 2018a; Qi et al., 2018b; Qi et al., 2019) and another in a juxta-membrane position (Qian et al., 2018; Zhang et al., 2018), corresponding to the binding site for the SHH palmitoyl moiety (Qi et al., 2018b).

(B) Close-up view of (A), showing the cholesterol in the SBP.

(C) Close-up view of (A), showing the cholesterol in the juxta-membrane tunnel.

(D) The sterol-sensing domain (SSD) contains a third cholesterol, as observed previously (Gong et al., 2018; Qi et al., 2018a; Qi et al., 2018b; Qian et al., 2018; Zhang et al., 2018; Qi et al., 2019).

(E) Density for PTCH1 in the GAS1–SHH1–PTCH1 ternary complex, showing cholesteryl hemisuccinate (CHS) in the SBP.

(F) As in (E), but showing cholesterol in the SSD.

(G) Density for GAS1-G1 domain in the GAS1–SHH–PTCH1 ternary complex.

(H) As in (G), but showing the GAS1-G2 domain with bound cholesterol.

(I) Density for the palmitoylated N-terminal SHH peptide in the GAS1–SHH–PTCH1 ternary complex.

(J) Density for the SHH globular domain in the GAS1–SHH–PTCH1 ternary complex.

(K) Density for the cholesterylated C-terminal SHH peptide in the GAS1–SHH–PTCH1 ternary complex.

(L) As in (E), but showing a representative glycan attached to N302 in PTCH1.

(M) As in (L), but for glycan attached to N989 in PTCH1.

(N) As in (G), but showing a representative glycan attached to N117 in GAS1-G1.

Figure S3

Figure S3. Cryo-EM data processing flowchart and model assessment for GAS1–SHH–PTCH1, Related to Figure 2

(A) Representative cryo-EM micrograph of the GAS1–SHH–PTCH1 nanodisc sample.

(B) Representative 2D class averages showing views at different angles.

(C) Flowchart of the data processing procedures (see STAR Methods).

(D) Angular distribution of the particles in the final refinement.

(E) Local resolution map.

(F) Gold-standard Fourier shell correlation (FSC) curve for the final map indicate overall resolution of 3.53 Å.

Figure S4

A

B

C

26139 micrographs → Manual selection → 23116 micrographs → Autopick by Gautomatch → 15951543 particles → 2D classification (2x binning) → 5132625 particles

Initial model from cryoSPARC

Re-center, re-extract and dedupilicate particles (1x binning) ← 1195646 particles ← 2D classification

27.86%   17.66%   17.00%   22.58%   14.90%

3D classification
iter 1-30: 3.7°
iter 31-50: 1.8°

9.17%   24.87%   30.83%   35.11%

3D auto-refine

3D classification without alignment

20.91%   27.16%   25.51%   26.40%   3.6 Å

3D auto-refine

CTF Refinement
2x Bayesian Polishing
3D auto-refine
Post processing

3.4 Å   3.0 Å

D

E   4.2   3.9   3.6   3.3   3.0

F

FSC=0.143   3.0 Å

Fourier Shell Correlation

Spatial Frequency (1/Å)

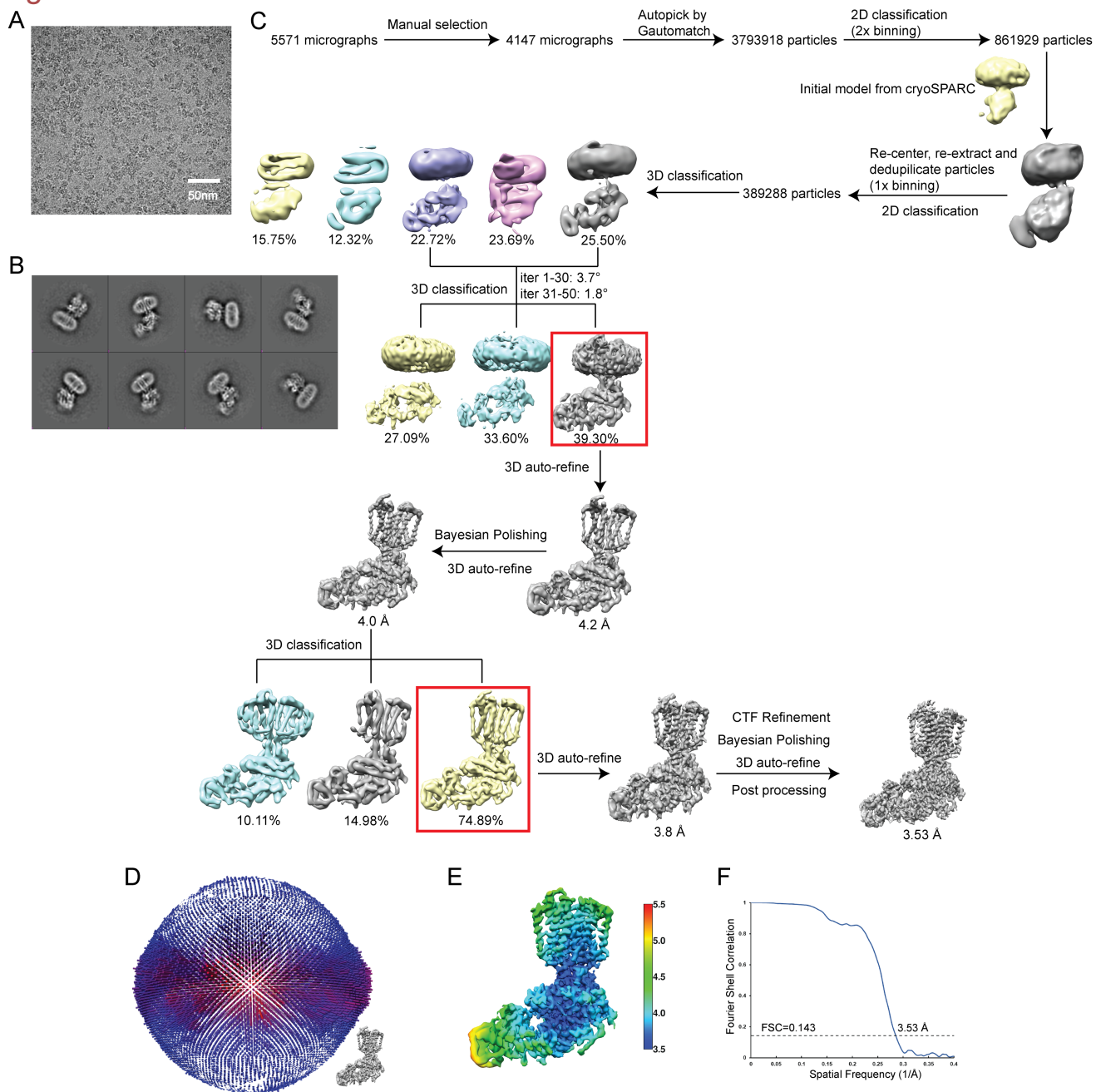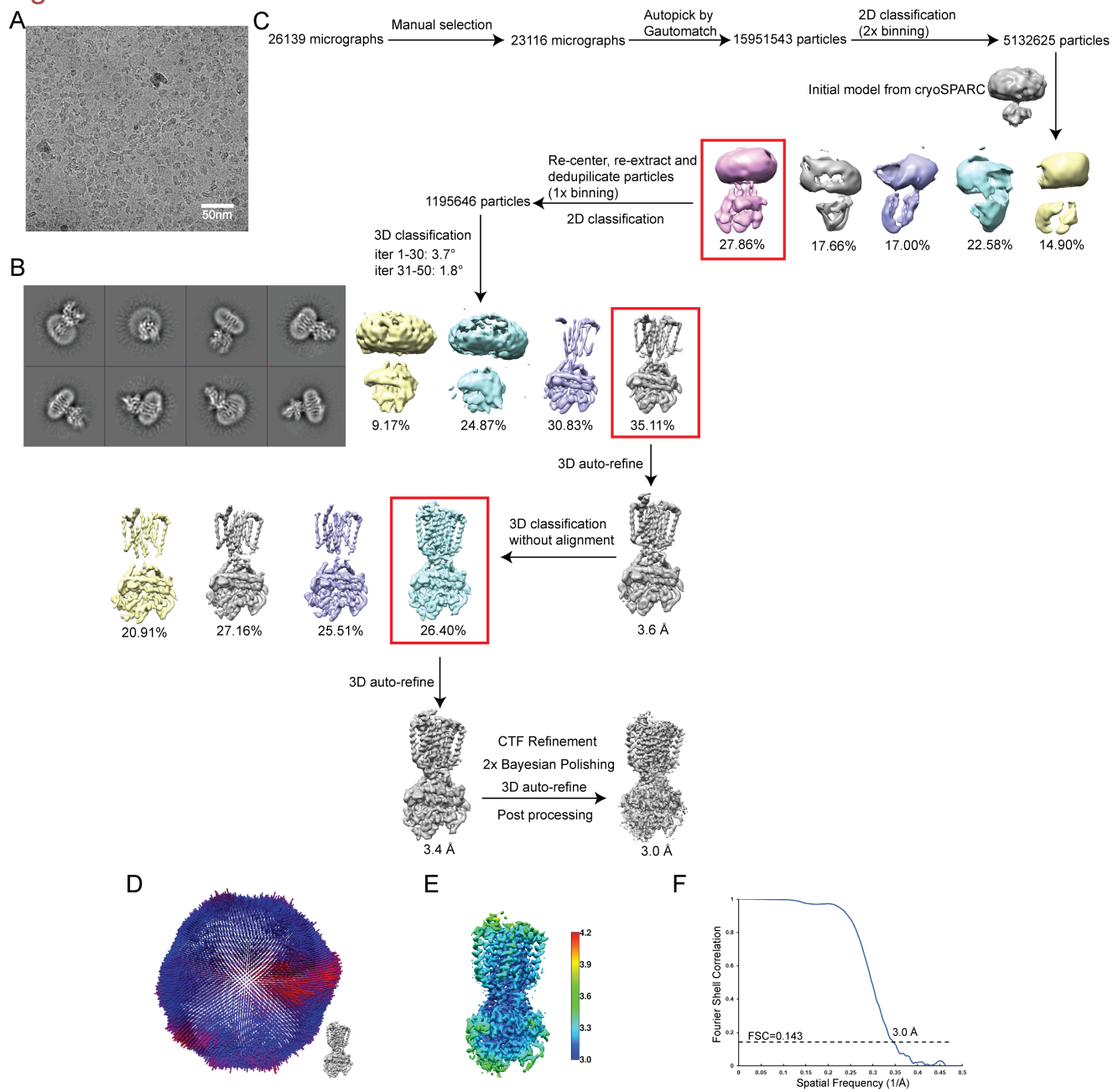**Figure S4. Cryo-EM data processing flowchart and model assessment for apo-PTCH1, Related to Figure 2**

(A) Representative cryo-EM micrograph of the apo-PTCH1 nanodisc sample.
(B) Representative 2D class averages showing views at different angles.
(C) Flowchart of the data processing procedures (see STAR Methods).
(D) Angular distribution of the particles in the final refinement.
(E) Local resolution map.
(F) Gold-standard Fourier shell correlation (FSC) curve for the final map indicate overall resolution of 3.0 Å.

Figure S5

A TM domains

B ECD1 + ECD2

C ECD1

D ECD2

apo-PTCH1
apo-PTCH1 (6DMB)
PTCH1-A (6RVD)
PTCH1-B (6RVD)

E TM domains

F ECD1 + ECD2

apo
complex

G

GAS1-ΔLoLiTa
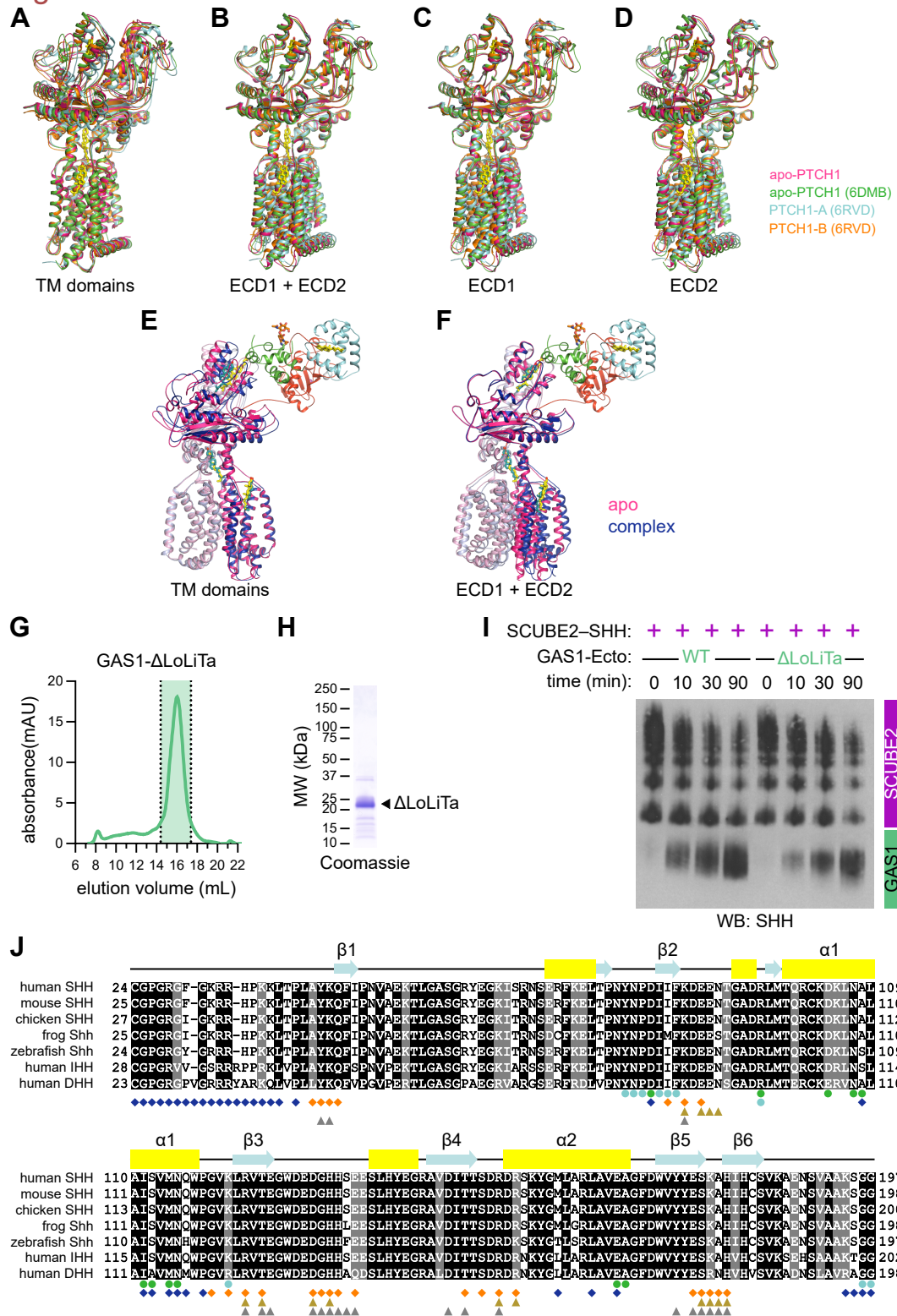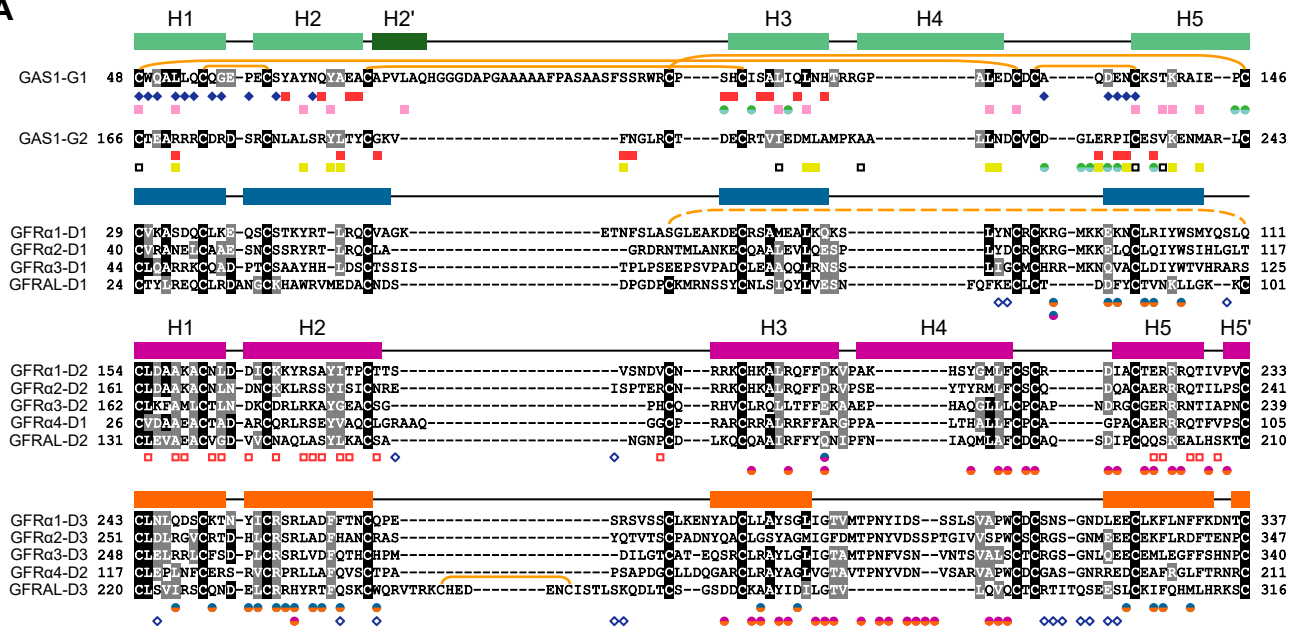
H

ΔLoLiTa

Coomassie

I

WB: SHH

Figure S5. Additional aspects of apo-PTCH1 and GAS1–SHH–PTCH1 ternary complex structures, Related to Figure 2
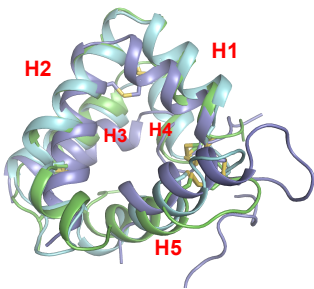
(A) Comparison of *Xenopus* apo-PTCH1 (deep pink) with previously solved human PTCH1 structures: apo-PTCH1 from Gong et al. (2018) (PDB ID: 6DMB, green), and PTCH1-A (cyan) and PTCH1-B (orange) from the Rudolf et al. (2019) rebuilding of the 1:2 SHH–PTCH1 complex in Qi et al. (2018a) (PDB ID: 6RVD). Structures are aligned on the TMDs, which are nearly identical regardless of the presence of SHH.

(B) As in (A), but with structures aligned on PTCH1-ECD1 and -ECD2.

(C) As in (A), but with structures aligned on PTCH1-ECD1.

(D) As in (A), but with structures aligned on PTCH1-ECD2.

(E) Apo-PTCH1 and GAS1–SHH–PTCH1 ternary complex structures aligned on TMDs, related to Figure 2D.

(F) As in (E), but with structures aligned on PTCH1-ECD1 and -ECD2. The TMDs and ECDs are nearly identical if viewed in isolation, but there is relative rigid-body movement between them upon GAS1–SHH binding.

(G) Size-exclusion chromatogram (Superdex 200 10/300) of purified GAS1-Ecto lacking the loop, linker, and the portion of the tail after the polyacidic motif (ΔLoLiTa), following FLAG-HT7 tag removal. The indicated monomeric fractions (shaded) were pooled and concentrated.

(H) Purified monomeric GAS1-ΔLoLiTa from (G) was analyzed by SDS-PAGE and Coomassie staining.

(I) Purified SCUBE2–SHH (400 nM) was incubated with full-length GAS1-Ecto or GAS1-ΔLoLiTa (2 μM), followed by native PAGE and immunoblotting. Both GAS1-Ecto and GAS1-ΔLoLiTa accept SHH from SCUBE2.

(J) Sequence alignment of SHH homologs, with major secondary elements labeled. Residues that interact (4.5-Å cutoff) with GAS1-G1 (green circle), GAS1-G2 (cyan circle), PTCH1-A (blue diamond), PTCH1-B (orange diamond), CDON-FN3 (gold triangle), and 5E1 (gray triangle) are indicated. GAS1 largely covers the PTCH1-A binding site on SHH. CDON and 5E1 bind to the PTCH1-B binding site on SHH.
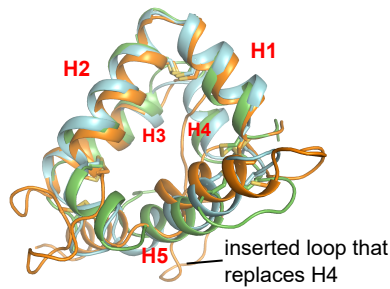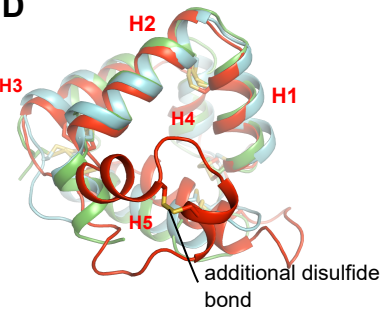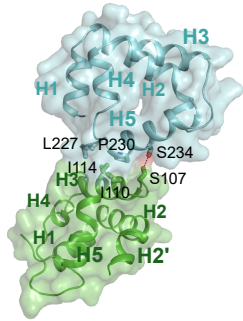
A

GAS1-G1   48 CWQALLQCQGE-PECSYAYNQYAEACAPVLAQHGGGDAPGAAAAAFPASAASFSSRWRCP---SHCISALIQLNHIRRGP--------ALEDCDCA---QDENCKSTKRAIE--PC 146
GAS1-G2   166 GTEARRRCDRD-SRCNLALSRYLTYCGKV-----------------------------FNGLRCT--DECRTVIEDMLAMPKAA------GLNDCVCD--GLERPICESVKENMAR-LC 243

GFRα1-D1   29 CVKASDQCLKE-QSCSTKYRT-IRQCVAGK-----------ETNFSLASGLEAKDECRSAMEALKQKS---LYNCRCKRG-MKKENCLRIYWSMYQSLQ 111
GFRα2-D1   40 CVRANEICAE-SNCSSRYRT-IRQCLA-----------GRDRNTMLANKECQAAIEVLQGSP---LYDCRCKRG-MKKLQCLQIYWSIHLGLT 117
GFRα3-D1   44 CLQARRKCQID-PTCSAAYHH-IDSCTSSIS-----------TPLPSEEPSVPADCLEAAQQLRNSS---LIGCMCHRR-MKNQVACLDIYWTVHRARS 125
GFRAL-D1   24 CTYPREQCLRDANGCKHAWRVMEDACNDS--------------DPGDPCKMRNSSYCNLSIQYLVESN---FQFKECLCT------DDFYCTVNKLLGK--KC 101

GFRα1-D2 154 CLDAAKTCNID-DICKKYRSAYITPCTTS------------VSNDVCN--RRKCHKAIRQFFDKVPAK---HSYGMUFCSCR--DIACTERRQTIVPVC 233
GFRα2-D2 161 CLDAAKTCNIN-DNCKKLRSSYISICNRE------------ISPTERCN--RRKCHKAIRQFFDRVPSE---YTYRMUFCSCQ--DQACAERRQTILPSC 241
GFRα3-D2 162 CLKFAMICTLN-DKCDRLRKAYCEACSG-------------PHCQ--RHVCLRQILTFFFEKAEP---LIGCMCHRR-MKNQVACLDIYWTVHRARS 239
GFRα4-D1   26 CVDAAEICTLD-ARCQRLRSEYVAQCLGRAAQ-----------GGCP--RARCRRAIRRFFARCPPA---LTHILIPCPCA--GPACAERRQTFVPSC 105
GFRAL-D2 131 CLEVAEACVGD-VYCNAQLASYIKACSA--------------NGNPCD--LKQCQAAIRFFYQNIPFN---IAQMLICDCAQ--SDIPCQQSKEALHSKTC 210

GFRα1-D3 243 CLNLQDSCKTN-YICRSRLADIFTNCQPE------------SRSVSSCLKENYADCLLAYSGLIGTVMTPNYIDS--SSLSVAPWCDCSNS-GNDLEECLKFLNFFKDNTC 337
GFRα2-D3 251 CLDIRGVCRTD-HICRSRLADEHANCRAS------------YQTVTSCPADNYQACLGSYAGMIGFDMTPNYVDSSPTGIV-SPWCSCRGS-GNMEECKFLRDFTENPC 347
GFRα3-D3 248 CLEIPRRICFSD-PLCRSRLVDEQTHCHPM-----------DILGTCAT--EQSRCLRAYLGLIGTVAMTPNFVSN--VNTSVALSCTCRGS-GNLEECEMLEGFFSHNPC 340
GFRα4-D2 117 CLEPLNFCERS-RVCPRLLABQVSCTPA------------PSAPDGCLLDQGARCLRAYAGLIGTVAVTPNYVDN--VSARVAPWCDCGAS-GNRREDCEAFRGLFTRNRC 211
GFRAL-D3 220 CISVIRSCQND-EICRHYRTFQSKCWQRVTRKCHED-----ENCISTLSKQDLTCS--GSDDCKAAYIDILGTV--------LQVCTCRTITQSESLCKIFQHMLHRKSC 316

B

C

inserted loop that replaces H4

D

additional disulfide bond

E

F

inserted loop that replaces H4 in D3

G

H

GAS1–SHH–PTCH1

I

GFRα2–NRTN–RET

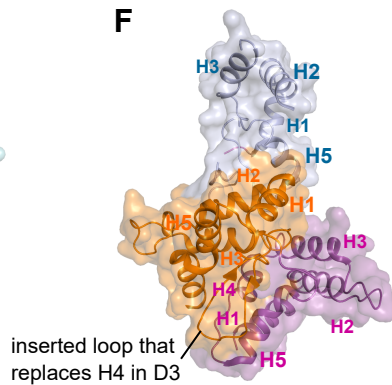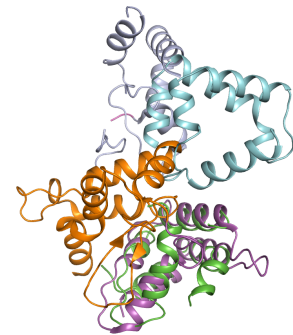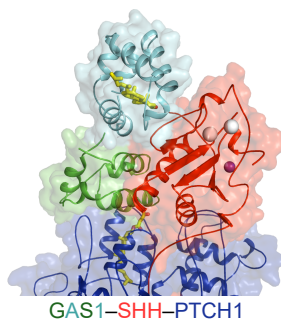**Figure S6. Additional comparisons of GAS1 and GFRα family proteins, Related to Figure 2 and 3**

(A) Sequence alignment of human GAS1 and GFRα family proteins (Cabrera et al., 2006). The sequences are grouped into four categories: GAS1-G1 and -G2 domains, all D1 domains (except for GFRα4, which lacks the homologous domain), all D2 domains, and all D3 domains. Helices are labeled (H1-H5) for G1 and D2. H4 is missing in D1 and D3, and H5 is broken into H5 and H5' in D2 and D3. Conserved disulfide bonds are indicated in yellow above GAS1-G1. The fourth disulfide bond is missing in GFRα1-3 (dashed line), while D3 of GFRAL contains an additional disulfide in the loop between H2 and H3. Residues involved in various interactions (4.5-Å cutoff) are labeled for GAS1 and GFRα2 (PDB ID: 6Q2O). For GAS1-G1 and -G2, the following are labeled: residues at the G1–G2 interface (green/cyan circles); residues that line the palmitate-binding hydrophobic cavity in G1 (pink squares); residues that line the hydrophobic cavity in G2 (black outline squares), some of which contact the SHH cholesteryl moiety (yellow squares); residues that contact the SHH globular domain (red squares); and residues that contact PTCH1-ECD1 (blue diamonds). For GFRα2-D1, -D2, and -D3, the following are labeled: residues at the D1–D2 interface (slate blue/purple circles); residues at the D1–D3 interface (slate blue/orange circles); residues at the D2–D3 interface (purple/orange circles); residues contacting GFL ligands (red outline squares); residues contacting the RET receptor (blue outline diamonds).

(B) GAS1-G1 (green) and GAS1-G2 (cyan) overlayed on GFRα2-D1 (slate blue), Related to Figure 3A. The fourth disulfide bond is invisible because it is located in a disordered region.

(C) As in (B), but overlayed on GFRα2-D3 (orange). In D3, in addition to H5 movement, H4 is replaced by a long inserted loop, which forms a large interface with D2 in full-length GFRα receptor structures (see below).

(D) As in (B), but overlayed on GFRAL (PDB ID: 5VZ4, red). As above, H5 moves. The five-disulfide pattern is conserved, except that an additional disulfide bond is located in the insertion between H2 and H3.

(E) Domain arrangement of full-length GAS1, showing the molecular surface. GAS1-G1 (green) and G2 (cyan) form a relatively small hydrophobic interface that mostly involves I110/I114 from G1 and L227/P230 from G2, stabilized by a hydrogen bond between S107, located in H3 of G1, and S234, located in H5 of G2.

(F) As in (E), but for GFRα2. D3 forms large interfaces with both D2 and D1. D3 and D2 are packed together by the inserted loop in D3 (labeled), which is absent in G1 and G2.

(G) Overlay of (E) and (F), with G1 and D2 aligned. The interdomain interface residues conserved in GFRα receptors are absent in GAS1, resulting in substantial differences in overall domain architecture.

(H) Coreceptor–ligand–receptor ternary complex for GAS1–SHH–PTCH1. GAS1 is colored as in (E), while SHH is red and PTCH1 is blue. SHH contains two calcium ions (white) and one zinc ion (pink). GAS1 contacts the SHH ligand through a large, extended interface and forms a smaller interface with the PTCH1 receptor.

(I) Coreceptor–ligand–receptor ternary complex for GFRα2–NRTN–RET (PDB ID: 6Q2O), with GFRα2-D2 aligned on GAS1-G1 in (H). GFRα2 is colored as in (F), while NRTN is red and RET is blue. In contrast to GAS1, GFRα2 contacts the RET receptor through a large, extended interface and forms a smaller interface with the NRTN ligand.
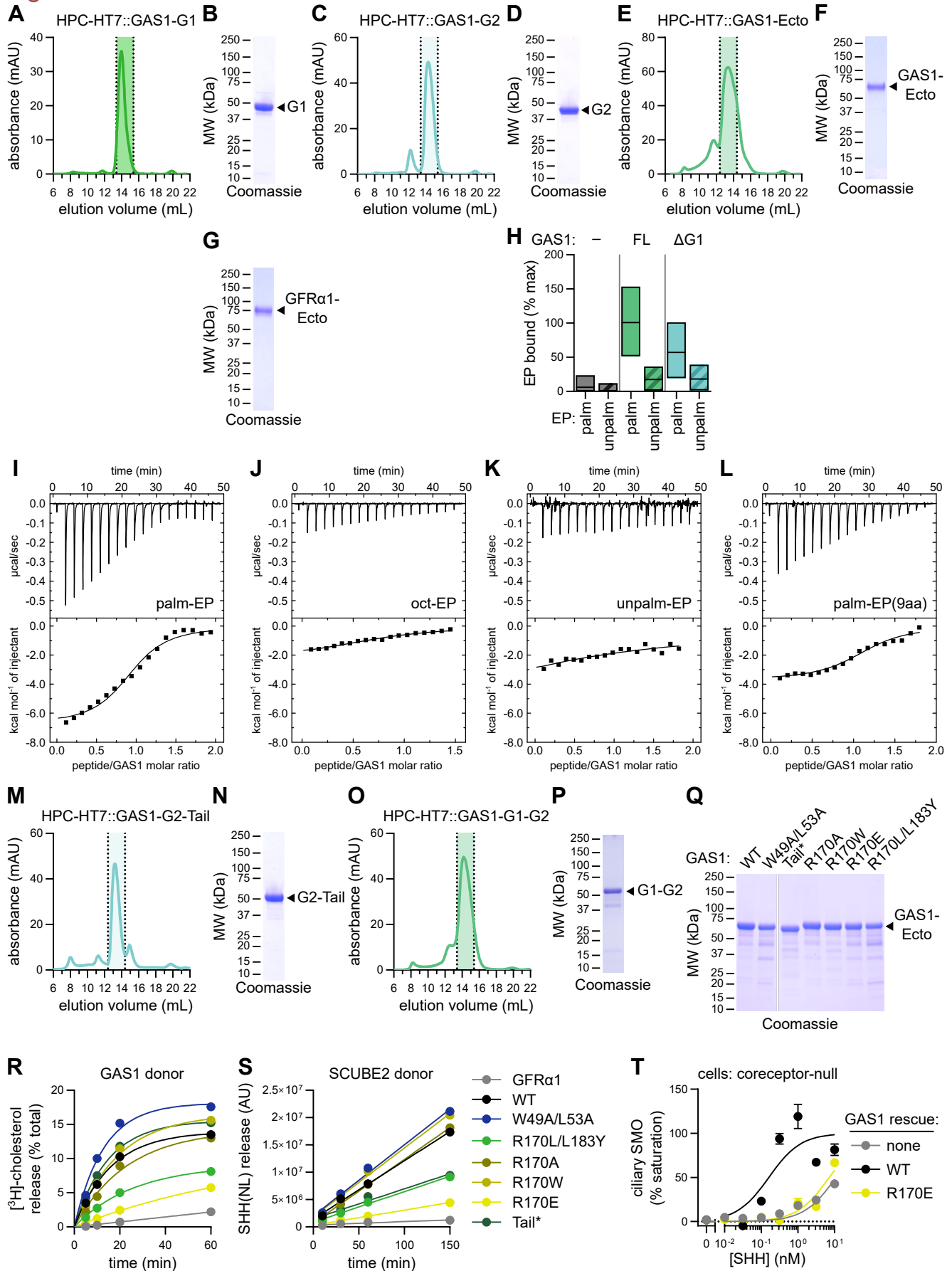
Figure S7. Biochemical and functional analysis of GAS1 constructs, Related to Figure 3

(A) Size-exclusion chromatogram (Superdex 200 10/300) of purified GAS1-G1. The indicated monomeric fractions (shaded) were pooled and concentrated.

(B) Purified monomeric GAS1-G1 from (A) was analyzed by SDS-PAGE and Coomassie staining.

(C) Size-exclusion chromatogram (Superdex 200 10/300) of purified GAS1-G2. The indicated monomeric fractions (shaded) were pooled and concentrated.

(D) Purified monomeric GAS1-G2 from (C) was analyzed by SDS-PAGE and Coomassie staining.

(E) Size-exclusion chromatogram (Superdex 200 10/300) of purified GAS1-Ecto. The indicated monomeric fractions (shaded) were pooled and concentrated.

(F) Purified monomeric GAS1-Ecto from (E) was analyzed by SDS-PAGE and Coomassie staining.

(G) Purified GFRα1-Ecto was analyzed by SDS-PAGE and Coomassie staining.

(H) HEK293T cells expressing eGFP-tagged full-length GAS1, GAS1-ΔG1, or SMO (negative control) were incubated with fluorescent SHH N-terminal effector peptide (EP, 2.5 μM), with or without palmitate (see STAR Methods). Bound EP was measured by fluorescence microscopy and automated image analysis. Data are normalized between EP binding to the negative control and to full-length GAS1 (100%). Box plots represent median, and first and third quartiles of bound EP. At least 400 cell objects were measured per condition. Data for SMO and GAS1 were reported in Figure S6D of Wierbowski et al. (2020). GAS1-ΔG1 was tested simultaneously, as part of the same experiment.

(I) Isothermal titration calorimetry (ITC) thermogram, showing binding of palmitoylated SHH EP (first 22 residues of human SHH) to GAS1-Ecto. Purified GAS1-Ecto (50 μM) was titrated by injection of 2 μL peptide aliquots (500 μM) at 25 °C. Binding isotherms were fit with a model in which the protein binds to N molecules of peptide. See Table S2 for the corresponding thermodynamic values, binding constants and N.

(J) As in (I), but with octanoylated SHH EP, which shows greatly reduced binding to GAS1-Ecto.

(K) As in (I), but for unpalmitoylated SHH EP, which shows no binding to GAS1-Ecto.

(L) As in (I), but for a truncated palmitoylated SHH EP (first 9 residues of human SHH), which shows significant binding to GAS1.

(M) Size-exclusion chromatogram (Superdex 200 10/300) of purified GAS1-G2-Tail. The indicated monomeric fractions (shaded) were pooled and concentrated.

(N) Purified monomeric GAS1-G2-Tail from (M) was analyzed by SDS-PAGE and Coomassie staining.

(O) Size-exclusion chromatogram (Superdex 200 10/300) of purified GAS1-G1-G2. The indicated monomeric fractions (shaded) were pooled and concentrated.

(P) Purified monomeric GAS1-G1-G2 from (O) was analyzed by SDS-PAGE and Coomassie staining.

(Q) Purified GAS1-Ecto variants containing the indicated mutations were analyzed by SDS-PAGE and Coomassie staining.

(R) Individual cholesterol release curves for GAS1 variants, used for deriving rate constants reported in Figure 3L. GAS1-Ecto was loaded with [^{3}H]-cholesterol and was captured on beads. The beads were incubated with purified GAS1-Ecto variants, or GFRα1-Ecto (negative control) (2 μM). Radioactivity released from the beads was measured at four time points, by scintillation counting. Data are fit with a one-phase association curve.

(S) As in (R), but measuring release of SHH(NL) from purified SCUBE2–SHH(NL) complex immobilized on beads, by NanoLuc luciferase assay. Data are fit with a linear regression, used to calculate the rate constants reported in Figure 3L.

(T) Dose-response of purified SCUBE2–SHH complex measured on coreceptor-null cells, rescued or not with wild-type GAS1 or R170E mutant. Data were normalized between Hh pathway activation for untreated cells and cells treated with saturating SAG, and were fit with a three-parameter curve. Data are reported as percentage of the theoretical maximum (% saturation). Points represent average ciliary SMO intensity for three replicates, and error bars represent SEM. At least 250 cilia were measured per replicate. The curves for no rescue and rescue with wild-type GAS1 are shared with Figure 6D, as the point mutants were assayed simultaneously.
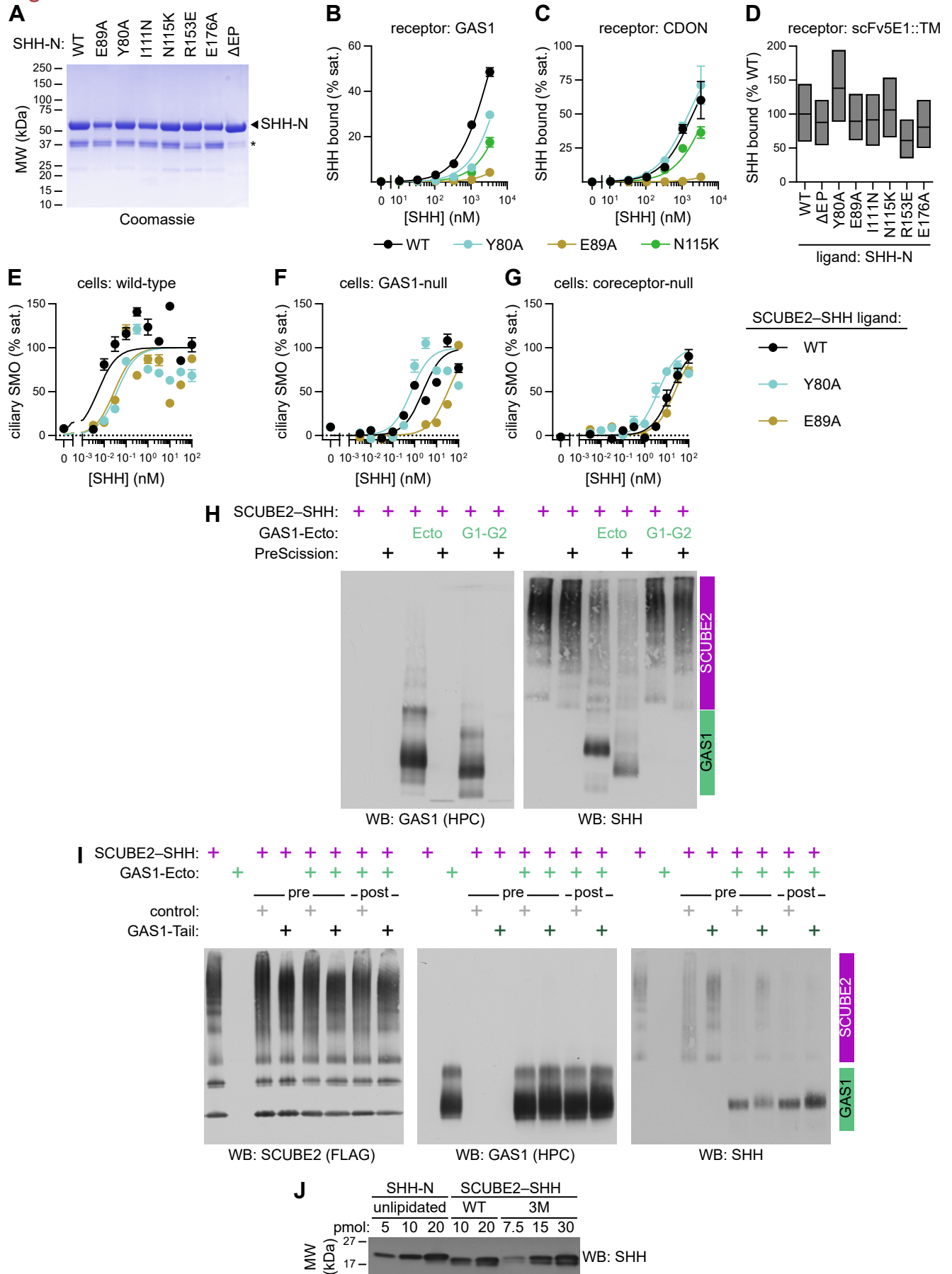
Figure S8

Figure S8. Biochemical and functional analysis of GAS1–SHH interfaces, Related to Figures 4 and 5
(A) SHH-N variants containing the indicated mutations were affinity purified from conditioned media of HEK293T cells and were analyzed by SDS-PAGE and Coomassie staining. Asterisk indicates a degradation product resulting from clipping in the flexible linker between SHH-N and the C-terminal HaloTag-HPC tag.
(B) HEK293T cells expressing eGFP-tagged GAS1 were incubated with varying amounts of purified tetramethylrhodamine (TMR)-labeled SHH-N variants, and bound ligand was quantified by fluorescence microscopy. Data are normalized between background signal (untreated cells) and theoretical maximum SHH-N binding (defined as 100%), as fit with a three-parameter curve. Points represent average binding for four replicates, and error bars represent SEM. At least 50 cell objects were measured per replicate. The three mutants show impaired binding to GAS1, of varying severity.
(C) As in (B), but measuring binding to CDON. SHH-N(E89A) does not bind CDON.
(D) As in (B), but measuring binding of SHH-N variants (500 nM) to a membrane-tethered variant of the scFv5E1 antibody (scFv5E1::TM). Box plots represent median, and first and third quartiles of binding. Data are normalized between binding of wild-type SHH-N to a negative control (SMO) and to scFv5E1 (100%). At least 300 cell objects were analyzed per condition. All SHH-N mutants bind scFv5E1.
(E) Dose-response of purified SCUBE2–SHH complex, containing wild-type SHH or SHH mutants defective in coreceptor binding, measured on wild-type MEFs, Related to Figure 4E. Hh pathway activation was measured by recruitment of endogenous SMO to cilia. Data were normalized between Hh pathway activation for untreated cells and cells treated with saturating SAG and fit with a three-parameter curve. Data are reported as a percentage of the theoretical maximum (% saturation). Points represent average ciliary SMO intensity for three replicates, and error bars represent SEM. At least 100 cilia were measured per replicate. The data for the wild-type SCUBE2–SHH complex were previously reported in Figure 3D of Wierbowski et al. (2020), as the mutant complexes were tested simultaneously. Both SHH mutants are less potent.
(F) As in (E), but for GAS1-null MEFs. The SHH(Y80A) mutant exhibits no further defect compared to wild-type SHH, consistent with its specific defect in binding GAS1. The SHH(E89A) mutant is more severely impaired, due to loss of both GAS1 and CDON binding.
(G) As in (E), but for coreceptor-null MEFs. The data for the wild-type complex were previously reported in Figure 3D of Wierbowski et al. (2020), as the mutant complexes were tested simultaneously. Wild-type SHH and the two HPE mutants have similar potency in the absence of CDON, BOC and GAS1, consistent with similar binding to PTCH1, as seen in Figure 4D.
(H) Purified SCUBE2–SHH (400 nM) was incubated with GAS1-Ecto or GAS1-G1-G2 (4 µM). GAS1 species were either tagged or the tag was removed by pretreatment with PreScission protease. The reactions were analyzed by native PAGE and immunoblotting. The inability of GAS1-G1-G2 to accept SHH from SCUBE2 is not a consequence of construct tagging.
(I) Purified SCUBE2–SHH complex (400 nM) was incubated with GAS1-Ecto (4 µM), before or after incubation of SCUBE2–SHH with recombinant HaloTag-GAS1 tail or HaloTag control (40 µM). Reaction mixes were analyzed as in (H). Preincubation with GAS1 tail reduces SHH transfer from SCUBE2 to GAS1.
(J) Purified SCUBE2–SHH complexes containing wild-type SHH or SHH with three mutations in the pseudo–active site (3M) were analyzed alongside recombinant unlipidated SHH-N by SDS-PAGE and immunoblotting. Both complexes contain comparable amounts of SHH species with slightly enhanced electrophoretic mobility relative to unlipidated SHH-N, characteristic of dually lipidated SHH (Porter et al., 1996a; Wierbowski et al., 2020). The SHH species are of the expected ~20-kDa molecular weight, indicative of proper cholesterol-dependent autoproteolysis in the endoplasmic reticulum. SHH lipidation is further suggested by co-purification with SCUBE2 and by signaling activity.

Figure S9

Figure S9. Biochemical and functional analysis of GAS1-catalyzed SHH–PTCH1 complex assembly, Related to Figures 5, 6, and 7

(A) Sequence alignment of GAS1 homologs, showing major structural features, including the polyacidic tail motif. Residues involved in various interactions (4.5-Å cutoff) are labeled as follows: residues at the G1–G2 interface (green/cyan circles); residues that line the palmitate-binding hydrophobic cavity in G1 (pink squares); residues that line the hydrophobic cavity in G2 (black outline squares), some of which contact the SHH cholesteryl moiety (yellow squares); residues that contact the SHH globular domain (red squares); and residues that contact PTCH1-ECD1 (blue diamonds).

(B) View of the GAS1-G2–SHH interface, showing density and SHH electrostatic surface potential. Electrostatic potential spans from red to blue (−4 kBT/ec to +4 kBT/ec). The extra density of GAS1 extends from G2 across a strip of basic residues on the SHH surface.

(C) As in (B), but showing overlay with heparin (green) (PDB ID: 4C4N). Heparin, a polyanion, binds along the SHH basic strip, in the same region as the extra density of GAS1. The polyacidic motif in GAS1 tail may bind SHH through a similar electrostatic interaction.

(D) Sequence alignment of the sterol-binding pocket (SBP) from PTCH1 homologs, with the three helices comprising the fingers of the pocket labeled (I, II, III). Residues involved in the following interactions (4.5-Å cutoff) are labeled: PTCH1-A and GAS1-G1 (green), PTCH1-A and SHH globular domain (blue/red square), and PTCH-B and SHH globular domain (orange/red square). Note the high degree of overlap between residues in PTCH1-A involved in binding GAS1 and SHH.

(E) Purified GAS1–SHH complexes, containing wild-type GAS1 or the GAS1(W49A/L53A) mutant, were analyzed by SDS-PAGE and Coomassie staining.

(F) Tryptophan (Trp) fluorescence emission (see STAR Methods) was measured for purified GAS1-Ecto incubated with palmitoylated SHH effector peptide (EP). Incubation with unpalmitoylated EP or buffer alone served as negative controls. Binding of GAS1-Ecto to palmitoylated EP causes Trp fluorescence quenching, suggesting movement of the W49 residue.

(G) Putative role of GAS1 residue W49 in coupling PTCH1 binding to palmitate release. In the GAS1–SHH–PTCH1 structure, W49 adopts an open conformation (green) and is inserted into the SBP of PTCH1-ECD1. In GAS1–SHH, W49 may flip (purple), to help enclose palmitate, consistent with the observed change in Trp fluorescence.

(H) SAG (1 μM), SHH-N conditioned medium, or SCUBE2–SHH conditioned medium were preincubated or not with the 5E1 antibody (400 nM), after which they were added to wild-type MEFs. Hh pathway activation was measured by endogenous SMO recruitment to cilia. Data were normalized between Hh pathway activation for untreated cells and SAG-treated cells (100%). Box plots represent median, and first and third quartiles of pathway activation. At least 400 cilia were analyzed per condition. 5E1 antagonizes both SCUBE2–SHH and SHH-N, but not SAG.

(I) The pseudo–active site triple mutant SHH-N^{3M} was expressed in HEK293T cells and was affinity purified from conditioned media. The protein was analyzed by SDS-PAGE and Coomassie staining. Asterisk indicates a degradation product resulting from clipping between SHH-N and the C-terminal HaloTag-HPC tag.

(J) Monomeric or dimerized TI23 anti-PTCH1 nanobody (Zhang et al., 2020), tagged with maltose-binding protein (MBP) at the N-terminus and a hexahistidine sequence at the C-terminus, were expressed and purified as described in STAR Methods. Purified proteins were analyzed by SDS-PAGE and Coomassie staining.

(K) NIH 3T3 cells expressing eGFP-tagged PTCH1 and mCherry-tagged SMO were treated with purified monomeric or dimerized TI23 anti-PTCH1 nanobody, or unlipidated SHH-N (positive control). Levels of ciliary SMO were measured by fluorescence microscopy and automated image analysis. Data were normalized between untreated cells and cells treated with saturating SAG (100%) and fit with a three-parameter curve. Points represent average ciliary SMO for three replicates, and error bars represent SEM. Both TI23 nanobody fusions cause Hh pathway activation, as reported (Zhang et al., 2020), indicating that they are functional.

(L) Purified GAS1-Ecto, SCUBE2, or BSA (negative control) was added (1 μM) to wild-type or DISP1-null (*DISP1*^{KO}) HEK293T cells stably expressing NanoLuc luciferase-tagged SHH [SHH(NL)], and SHH(NL) release was measured as a function of time. Bars represent average release rate across six time points, and error bars represent standard error of the linear fit to the release time course. In the absence of DISP1, GAS1 exhibits a partial defect in SHH release; in contrast, SHH release by SCUBE2 is strictly DISP1-dependent. The data for SHH release from wild-type cells were previously reported in Figure 5H of Wierbowski et al. (2020), as release from *DISP1*^{KO} cells was tested simultaneously.

Table S1. Data collection and model refinement parameters, Related to Figure 2

Data collection and processing

Magnification	130,000	
Voltage (kV)	300	
Exposure time (s/frame)	0.2	
Number of frames	50	
Electron exposure (e-/Å^2)	71	
Defocus range (μm)	-1.0 ~ -2.0	
Pixel size (Å)	1.06	
Symmetry imposed	C1	
	apo-PTCH1 PDB ID: 7RHR EMDB ID: 24467	**GAS1–SHH–PTCH1** PDB ID: 7RHQ EMDB ID: 24466
Initial particle images (no.)	15,951,543	3,793,918
Final particle images (no.)	106,749	54,175
Map resolution (Å)	3.0	3.53
FSC threshold	0.143	0.143
Refinement		
Non-hydrogen atoms	7820	10459
Protein residues	974	1300
Ligands	CLR: 3, NAG: 4	CLR: 2, PLM: 1, Y01: 1, NAG: 8 CA: 2, ZN: 1
RMSDs		
Bond lengths (Å)	0.006	0.009
Bond angles (°)	0.869	1.016
Validation		
MolProbity score	1.86	1.51
Clashscore	9.63	3.37
Poor rotamers (%)	0.0	0.0
Ramachandran Plot		
Favored (%)	94.85	94.19
Allowed (%)	5.05	5.73
Disallowed (%)	0.1	0.08

Table S2. ITC measurement of GAS1–EP interaction, Related to Figure 3

EP variant	N	$K_a \times 10^5$ (M^{-1})	K_d (μM)	ΔG (kcal·mol^{-1})	ΔH (kcal·mol^{-1})	ΔS (cal·mol^{-1}·K^{-1})	Associated Figure
palm	0.86 ± 0.09	2.60 ± 0.16	3.86 ± 0.25	-7.60 ± 0.03	-6.14 ± 0.54	4.92 ± 0.91	S7I
oct	0.88 ± 0.06	0.29 ± 0.09	34.6 ± 3.11	-6.29 ± 0.25	-2.54 ± 0.04	12.6 ± 0.50	S7J
unpalm	ND	ND	ND	ND	ND	ND	S7K
palm (9aa)	1.14 ± 0.04	2.69 ± 0.07	3.72 ± 0.26	-7.46 ± 0.27	-4.23 ± 0.17	10.8 ± 1.84	S7L